
Doctoral Dissertations

Student Theses and Dissertations

1975

Evaluation of the transition density function of carbon on various substrates from KLL Auger spectrum. Application of Auger electron spectroscopy to the bulk-to-surface precipitation and surface diffusion of carbon on polycrystalline nickel

Juan F. Mojica

Follow this and additional works at: https://scholarsmine.mst.edu/doctoral_dissertations

 Part of the [Physics Commons](#)

Department: Physics

Recommended Citation

Mojica, Juan F., "Evaluation of the transition density function of carbon on various substrates from KLL Auger spectrum. Application of Auger electron spectroscopy to the bulk-to-surface precipitation and surface diffusion of carbon on polycrystalline nickel" (1975). *Doctoral Dissertations*. 265.
https://scholarsmine.mst.edu/doctoral_dissertations/265

This thesis is brought to you by Scholars' Mine, a service of the Missouri S&T Library and Learning Resources. This work is protected by U. S. Copyright Law. Unauthorized use including reproduction for redistribution requires the permission of the copyright holder. For more information, please contact scholarsmine@mst.edu.

EVALUATION OF THE TRANSITION DENSITY FUNCTION OF CARBON
ON VARIOUS SUBSTRATES FROM THE KLL AUGER SPECTRUM.
APPLICATION OF AUGER ELECTRON SPECTROSCOPY TO THE BULK-
TO-SURFACE PRECIPITATION AND SURFACE DIFFUSION OF CARBON
ON POLYCRYSTALLINE NICKEL.

BY

JUAN F. MOJICA, 1941-

A DISSERTATION

Presented to the Faculty of the Graduate School of the
UNIVERSITY OF MISSOURI - ROLLA

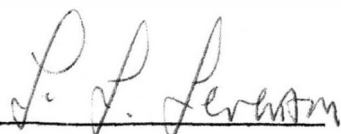
In Partial Fulfillment of the Requirements for the Degree
DOCTOR OF PHILOSOPHY

in

PHYSICS

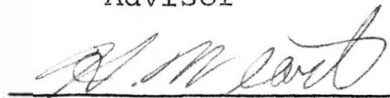
1975

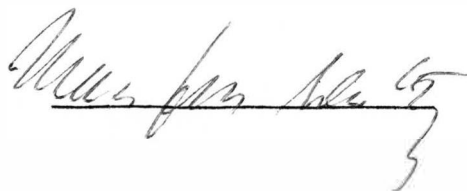
T3056
151 pages
c.1

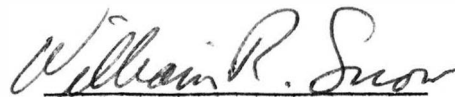


Advisor









248244

PUBLICATION THESIS OPTION

This dissertation has been prepared in the style utilized by Surface Science. Part I, pages vi-x and 2-94 and Part II, pages xi and 104-134 will be submitted for publication to Surface Science.

ACKNOWLEDGMENTS

The author wishes to express his sincere appreciation to Dr. L. L. Levenson, Associate Professor of Physics and Senior Investigator at the Graduate Center for Materials Research (GCMR) for his advice, encouragement and support in carrying out this work.

He wishes to thank Dr. M. Wuttig, Professor of Metallurgy, Dr. I. Adawi, Professor of Physics, Dr. H. W. Weart, Professor and Chairman of Metallurgy, and Dr. W. R. Snow, Assistant Professor of Physics for their helpful discussions and suggestions.

The support of the author's wife is appreciated.

The financial support from the Graduate Center for Materials Research, the National Science Foundation, and the Consejo Nacional de Ciencia y Tecnología de México is gratefully acknowledged.

TABLE OF CONTENTS

	Page
PUBLICATION THESIS OPTION.....	ii
ACKNOWLEDGMENTS.....	iii
TABLE OF CONTENTS.....	iv
LIST OF ILLUSTRATIONS.....	vi
LIST OF TABLES.....	xii
INTRODUCTION.....	1
PART I. Evaluation of the Transition Density Function of Carbon on Various Substrates from the KLL Auger Spectrum.....	2
ABSTRACT.....	3
INTRODUCTION.....	4
EXPERIMENTAL PROCEDURE.....	5
1. Instrumentation.....	5
2. The Samples.....	6
3. The Auger Micrographs.....	8
THE N(E) FUNCTION.....	9
THE TRANSITION DENSITY FUNCTION.....	12
INITIAL RESULTS.....	15
THE UNBROADENED AUGER FUNCTION A(E).....	16
RESULTS WITHOUT INSTRUMENTAL BROADENING.....	19
THE EFFECT OF CONCENTRATION.....	22
CONCLUSION.....	23
REFERENCES.....	25
APPENDIX I. The Transition Density Function.....	95
APPENDIX II. Flow Diagram for the Evaluation of the Transition Density Function.....	99

	Page
PART II. Application of Auger Electron Spectroscopy to the Bulk-to-Surface Precipitation and Surface Diffusion of Carbon on Polycrystalline Nickel.....	104
ABSTRACT.....	105
INTRODUCTION.....	106
EXPERIMENTAL PROCEDURE.....	108
EXPERIMENTAL RESULTS.....	110
ANALYSIS.....	113
DISCUSSION.....	117
CONCLUSION.....	119
REFERENCES.....	121
APPENDIX I. Diffusion of Two Semi-Infinite Media Through an Interface.....	135
VITA.....	139

LIST OF ILLUSTRATIONS

	Page
PART I.	
1. Carbon KLL Auger spectra from different materials. A was obtained from silicon carbide. B corresponds to pyrolytic graphite. C was obtained from a vacuum deposited film of nickel in which the carbon was an impurity.....	29
2. Auger spectrum of a piece of stress-annealed pyrolytic graphite. Spectrum A shows no contamination at the surface. Spectrum B reveals traces of nitrogen and oxygen at the surface.....	31
3. Micrograph of stress-annealed pyrolytic graphite. The dark region B was found to correspond to trace impurities of nitrogen and oxygen.....	32
4. Micrograph of a sample prepared by vacuum deposition of a chromium film through a gold grid onto pyrolytic graphite. Micrograph A was recorded with the 532 eV minimum of the $dN(E)/dE$ which corresponds to chromium. Micrograph B was taken with the 272 eV minimum that is characteristic of carbon.....	34
5. Micrographs of the same sample as in fig. 4. The dark regions show the distribution of the 258 and 249 eV maxima of the carbon $N(E)$ Auger curve respectively.....	36
6. Schematic diagram of the background suppression process.....	37
7. Flow diagram for the process of analog integration of the $dN(E)/dE$ Auger signal with background suppression.....	38

	Page
8. $N'(E)$ and $N(E)$ Auger curves as obtained from the (0001) surface of pyrolytic graphite placed at 90° angle of incidence with respect to the electron beam. Also shown are the gaussian components of the $N(E)$ curve.....	40
9. $N'(E)$ and $N(E)$ Auger curves from pyrolytic graphite (0001) placed at 60° angle of incidence with respect to the electron beam. The gaussian components of the $N(E)$ curve are also shown.....	42
10. Auger curves $N'(E)$ and $N(E)$ and the gaussian components of $N(E)$ of carbon on cobalt.....	44
11. Auger curves $N'(E)$ and $N(E)$ and the gaussian components of the $N(E)$ curve of carbon on copper.....	46
12. Auger curves $N'(E)$ and $N(E)$ and the gaussian components of the $N(E)$ curve of diamond (111).....	47
13. Auger curves $N'(E)$ and $N(E)$ and the gaussian components of the $N(E)$ curve of carbon in silicon carbide.....	48
14. Auger curves $N'(E)$ and $N(E)$ and the gaussian components of the $N(E)$ curve of carbon on titanium.....	49
15. Auger curves $N'(E)$ and $N(E)$ and the gaussian components of the $N(E)$ curve of carbon on vanadium.....	50
16. Auger curves $N'(E)$ and $N(E)$ and the gaussian components of the $N(E)$ curve of carbon on chromium.....	51
17. Auger curves $N'(E)$ and $N(E)$ and the gaussian components of the $N(E)$ curve of carbon on iron.....	52
18. Auger curves $N'(E)$ and $N(E)$ and the gaussian components of the $N(E)$ curve of carbon on nickel.....	53

	Page
19. Auger curves $N'(E)$ and $N(E)$ and the gaussian components of the $N(E)$ curve of carbon on copper.....	54
20. Diagram of the Auger process, ref.[13].....	55
21. Transition density functions of carbon in pyrolytic graphite (0001) placed at 90° and 60° angles of incidence with respect to the electron beam and also on copper and cobalt as evaluated from the $N(E)$ Auger function.....	57
22. Transition density functions of carbon in pyrolytic graphite (0001) placed at 90° angle of incidence with respect to the electron beam and in silicon carbide. Transition density functions of carbon on titanium, vanadium and chromium are also shown. These functions are evaluated from the $N(E)$ curve.....	59
23. Transition density functions of carbon in pyrolytic graphite (0001) at 90° angle of incidence with respect to the electron beam and on iron, nickel and copper. All these functions are evaluated from the $N(E)$ curve.....	61
24. Auger curves $N'(E)$ and $N(E)$ and the gaussian components of the $N(E)$ curve of the valence band of nickel.....	62
25. Valence band of nickel. The broken line shows the results obtained by Hagstrum [20] using Ion-Neutralization Spectroscopy. The full line corresponds to the transition density calculated from the Auger function $N(E)$	64
26. Computer simulation of instrumental broadening in the transition density function of carbon in pyrolytic graphite...	66
27. Computer simulation of instrumental broadening in the transition density function of carbon on nickel.....	68

	Page
28. Unbroadened Auger curves $A(E)$ of pyrolytic graphite (0001) at 60° and 90° angles of incidence with respect to the electron beam and also of diamond (111).....	69
29. Unbroadened Auger curves $A(E)$ of carbon on copper and cobalt. The original $N'(E)$ curve was of the graphitic form.....	70
30. Unbroadened Auger curves $A(E)$ of carbon in silicon carbide and on titanium.....	71
31. Unbroadened Auger curves $A(E)$ of carbon on nickel, chromium and vanadium.....	72
32. Unbroadened Auger curves $A(E)$ of carbon on iron and copper.....	73
33. Comparison of the valence band of diamond as reported by McFeely et al.[24] and the results obtained from the transition density function calculated from Auger electron spectroscopy. $I'(E)$: XPS spectrum, McFeely et al. $\phi(E)/v^2$: K X-ray emission spectrum, Wiech and Zopf. $\rho(E)$: Density of states, Painter et al.....	74
34. Transition density function of carbon in pyrolytic graphite (0001) at 90° angle of incidence with respect to the electron beam and in silicon carbide, calculated from the unbroadened Auger function $A(E)$	76
35. Transition density function of carbon in pyrolytic graphite (0001) at 60° angle of incidence with respect to the electron beam and in diamond (111). Also shown are the transition density functions of carbon on cobalt and copper. All these functions were calculated from the unbroadened Auger function $A(E)$	78
36. Transition density function of carbon on titanium, vanadium and chromium as calculated from the unbroadened Auger function $A(E)$	80

	Page
37. Transition density function of carbon on nickel, iron and copper as calculated from the unbroadened Auger function $A(E)$	82
38. Comparison between predicted [21] and experimentally obtained KLL Auger transitions of carbon. The cases of pyrolytic graphite (0001) at 60° and 90° angles of incidence with respect to the electron beam and of diamond (111) are shown.....	84
39. Comparison between predicted [21] and experimentally obtained KLL Auger transitions of carbon. The cases of silicon carbide, and of carbon on cobalt and copper are shown.....	86
40. Comparison between predicted [21] and experimentally obtained KLL Auger transitions of carbon. The cases of carbon on titanium, vanadium and chromium are shown.....	88
41. Comparison between predicted (broken lines) [21] and experimentally obtained KLL Auger transitions of carbon. The cases of carbon on iron, cobalt, nickel and copper are shown.....	90
42. Relation between the energies of the KLL Auger transitions of carbon and the metal substrate. The broken horizontal lines correspond to the predicted values [21] for atomic carbon.....	92
43. Change in shape of the KLL Auger spectrum of carbon on copper as the concentration of carbon at the surface increases.....	93
44. Carbon surface concentration dependence of \sqrt{t}	94

PART II.	Page
1. Schematic diagram of the experimental results and their interpretation.....	123
2. Time dependence of the peak-to-peak amplitude of the $dN(E)/dE$ Auger spectrum of carbon and nickel.....	124
3. Time dependence of the peak-to-peak amplitude of the $dN(E)/dE$ Auger spectrum of carbon and nickel.....	125
4. Time dependence of the peak-to-peak amplitude of the $dN(E)/dE$ Auger spectrum of nickel and carbon.....	126
5. Evolution of the carbon Auger spectrum as the concentration of carbon increases at the surface. The time marks indicate when recordings were started after heating began.....	128
6. Micrographs of carbon on the surface of polycrystalline nickel. The arrow in micrograph D indicates the position of the electron beam when the Auger spectra were recorded. The diameter of the beam was 5 μm . This will correspond to a spot of 1.16 mm. diameter in the micrograph.....	130
7. Time dependence of the carbon relative concentration at the surface of the polycrystalline nickel sample. Zero time is taken at the transition point between zones A and B.....	131
8. Bulk-to-surface diffusion coefficient D dependence of $1/T$	132
9. Plot of the normalized surface concentration of carbon versus \sqrt{t} . Zero time is taken at transition point between zones A and B...	133
10. Surface diffusion coefficient D_s dependence of $1/T$	134

LIST OF TABLES

	Page
PART I.	
I. Approximate Carbon Coverage of the Surface of the Metal Film.....	27

INTRODUCTION

The time evolution of the KLL Auger spectrum of carbon was considered to be an effective tool in the study of the diffusion process of carbon on polycrystalline nickel. Although very simple in theory, the useful application of this procedure to the desired purpose required a deeper involvement in the understanding of the Auger process.

Integration and deconvolution techniques were necessary to gain access to the information contained in the derivative mode of the Auger signal.

Part I of the dissertation describes the experimental and analytical procedures that were used in the evaluation of the transition density function of carbon on different substrates.

Part II describes the study of the bulk-to-surface precipitation and surface diffusion of carbon on polycrystalline nickel. The evaluation of the kinetics of these processes involved the monitoring of the time evolution of the Auger carbon signal as a function of temperature and also a mathematical model in terms of an interface.

Part I and Part II will be submitted for publication to Surface Science.

Part I

Evaluation of the Transition Density Function of Carbon
on Various Substrates from the KLL Auger Spectrum.

Manuscript to be submitted to Surface Science.

ABSTRACT

Analog integration with suppression of background and instrumental broadening is performed on the derivative mode of the carbon Auger signal. Information about the electronic states of carbon is derived by evaluation of the transition density function of the Auger process. It is found that the transition density function is continuous for well defined crystal structures such as graphite, diamond and silicon carbide, but discrete for carbon impurities on metal substrates. These results indicate the existence of a band for the crystal case, but also suggest the presence of atomic-like transitions for situations in which carbon appears only as an impurity.

INTRODUCTION

Several attempts have been made to associate the energies and the shapes of Auger spectra, recorded as the first derivative of the Auger current, not only with the elements present at the surface but also with their chemical state.

In the particular case of carbon, Haas and Grant[1] reported the influence of the chemical state of carbon on the KLL spectrum of this element. They recorded the change of the carbon Auger spectrum at the surface of molybdenum as CO was adsorbed. The carbon spectrum which was associated with a carbide changed its shape when CO was present at the surface. Coad and Riviere[2] also reported the presence of two different spectra for the carbon KLL Auger transitions which they identified respectively as Ni_3C and graphite. Chang[3] presented four Auger spectra of carbon of different shape which were assigned to silicon, tungsten, titanium and nickel carbides. Recently, Haas and Pocker[4] have shown the Auger spectrum of a freshly fractured surface of a Ti-6Al-4V sample. The fine structure in the low energy side of the KLL spectrum of carbon is similar to the structure associated with titanium carbide. Haas and Pocker also report the change of this signal into the graphitic type following contamination of the sample from residual gases.

In all these cases, the presence of fine structure in the KLL Auger spectrum of carbon has been associated with the existence of a carbide at the surface of the sample.

Figure 1 shows three carbon KLL Auger spectra obtained from different samples: a single crystal of silicon carbide, a piece of stress-annealed pyrolytic graphite, and carbon that was present as an impurity in a vacuum-deposited film of nickel on a graphite substrate. The sharp minimum at about 273 eV is generally taken to be the energy of the $KL_{2,3}L_{2,3}$ Auger transition. In fact, this minimum represents the maximum negative slope of the $N(E)$ curve of the Auger signal. The precise energy at which the minimum occurs depends upon the shape of the $N(E)$ curve. The shape of the $dN(E)/dE$ signal on the low energy side of the 273 eV minimum also depends upon the exact shape of the $N(E)$ spectrum.

In the present work a new approach is taken in explaining the origin and the meaning of the fine structure in the Auger carbon spectrum. It will be shown that this fine structure is probably an effect of the concentration of the impurity carbon in the metal matrix and not necessarily produced by the formation of a carbide.

EXPERIMENTAL PROCEDURE

1. Instrumentation

The instrument used for the Auger analysis of the samples was a Scanning Auger Spectrometer (Physical

Electronics Industries, Inc.). A complete description of the apparatus is given in ref.[5]. In the present case the analysis of the samples was done with a primary electron beam current of $0.3\mu\text{A}$ and a beam energy of 5 keV. The beam size was estimated to be about $5\ \mu\text{m}$. The modulation voltage was 3eV.

A feature of the Scanning Auger Spectrometer is its ability to perform surface analysis with spatial resolution. An example of how this technique can be combined with Auger point analysis to obtain more information is shown in figs. 2 and 3. Figure 2A is the Auger spectrum of clean pyrolytic graphite. No impurities were detected in this spectrum. Figure 3 is an Auger micrograph of the area around the point previously analyzed. This micrograph reveals the existence of some impurities at the surface (dark region B).

An Auger analysis of region B (fig. 2B) reveals the existence of traces of nitrogen and oxygen in this region.

2. The Samples

The samples were prepared by vacuum deposition of a metal film approximately $500\ \text{\AA}$ thick on a piece of stress-annealed pyrolytic graphite (Union Carbide Corporation, Parma, Ohio). During deposition, the graphite was covered by a gold grid. The metal film was then coated with approximately $100\ \text{\AA}$ of carbon, evaporated from a carbon arc in vacuum. The carbon film was then covered with

another 200 Å of the same metal. The deposition was done at a pressure of 10^{-3} Pa in a diffusion pumped chamber. After deposition the gold grid was removed to expose the pyrolytic graphite substrate. The samples were then placed in the vacuum chamber of the Scanning Auger Spectrometer.

The purpose of using a gold grid to mask the pyrolytic graphite during the metal deposition was to create a recognizable pattern on the graphite substrate. This metal pattern improved considerably the usefulness of the Auger micrographing technique. The final appearance of the samples is illustrated in fig. 4A. In this micrograph the bright regions correspond to the metal deposited in a square pattern, while the dark stripes around the metal squares correspond to the graphite substrate.

To allow some diffusion to occur at the carbon-metal interface, the samples were heated in situ for 20 minutes to about 500°C. After this treatment the uppermost layer of metal was ion-sputtered until the Auger signal of carbon attained a convenient size.

Special attention was paid to sample contamination from residual gases. For all experiments it was necessary to work at pressures below 10^{-7} Pa. Otherwise sample contamination occurred during measurements.

Finally, Table I gives the carbon coverages that were achieved after all these procedures were completed. These coverages were approximated from a previous calibration work of M. Smith (unpublished). Using a quartz crystal

microbalance to monitor the coverage he obtained the ratio between the peak-to-peak amplitudes of the $dN(E)/dE$ Auger curves of nickel and carbon. The coverages for the other metals were extrapolated from the nickel curve by considering the different Auger yields of those metals with respect to carbon[6]. The coverages in Table I are estimated to be accurate to about 30%.

3. The Auger Micrographs

The Auger micrographs are produced by recording on photographic film the intensity of the $dN(E)/dE$ Auger spectrum of an element as the electron beam is rastered over an area of the target.

In our case, micrographs taken at selected energies of the fine structure mapped the origin of electrons contributing to this fine structure. Examples are shown in figs. 4 and 5. Micrograph A in fig. 4 corresponds to the metal film recorded with the 532 eV characteristic minimum of the $dN(E)/dE$ Auger spectrum of chromium. Micrograph B in the same figure corresponds to the graphite substrate recorded at 272 eV.

The two micrographs in fig. 5 were recorded using the maxima of the carbon $N(E)$ Auger signal at 258 and 249 eV. A word of caution is necessary in interpreting these two micrographs. They were taken using positive excursions of the $dN(E)/dE$ curve. Because of the way the instrument was designed, the micrographs in fig. 5 are like the negative of an Auger micrograph taken at an energy

corresponding to a negative excursion. Therefore, in these micrographs the black portions of the micrograph correspond to carbon atoms producing Auger electrons at the energies recorded.

The two micrographs in fig. 5 are significant in the sense that they show differences (spots 1, 2 and 3 in micrograph B) between the transitions occurring at those energies.

The dark spot at point 1 of fig. 5B indicates that 249 eV electrons originate there, but 258 eV electrons do not according to fig. 5A. The light spot at point 2 of fig. 5B means a nearly complete absence of 249 eV electrons, and point 3 in the same micrograph shows a region of relatively weak 249 eV electron emission.

Figure 5B illustrates the high information content of Auger micrographs. It also emphasizes the difficulty in directly interpreting $dN(E)/dE$ spectra. A more direct approach to interpreting Auger electron spectra is to use $N(E)$ curves.

THE $N(E)$ FUNCTION

The importance of obtaining the $N(E)$ Auger function is well established in the literature. Analog and numerical integration techniques[7-10] as well as theoretical models [11] have been used to recover this function. In this way, a deeper understanding of the Auger process can be obtained. Furthermore, better use of the

information in the Auger signal makes electron spectroscopy a better tool for the chemical analysis of surfaces.

For this study, analog integration was performed with a TR-20 (Electronic Associates, Inc.) analog computer. The use of this computer also allowed the suppression of the background signal so that only the desired $N(E)$ function was recorded.

A schematic diagram of how background suppression was accomplished is shown in fig. 6. The integrated Auger signal was superimposed on a positively increasing background signal. With the aid of a constant voltage power supply and the use of an integrating circuit a decreasing voltage was added to the $N(E)$ signal to counteract the effect of the increasing background voltage. The flow diagram for use of the analog computer is shown schematically in fig. 7.

After the function $N(E)$ was recorded it was resolved, by means of a DuPont analog curve resolver, into a summation of gaussian functions. The results are shown in figs. 8-19.

The graphs resulting from these procedures can be categorized into three groups.

The first group is represented by those graphs in which the Auger signal, in the derivative mode ($dN(E)/dE$), has a graphitic like shape shown in figs. 8-11. Although the $dN(E)/dE$ and the $N(E)$ signals of the first group are very similar to each other, differences are apparent

when the $N(E)$ curve is resolved into gaussian components. In particular, the energy positions of the maxima and the width of the gaussian components vary among the samples of this group. It is also interesting to notice the difference between the $N(E)$ function of graphite as the sample was positioned at 90° (fig. 8) or 60° (fig. 9) angles of incidence with respect to the incoming electron beam. This difference reflects the effect of the crystal structure on the cross-section of the Auger process.

The second group can be classified as the diamond-like group, in which the minimum at 272 eV of the $dN(E)/dE$ curve is accompanied by a small satellite in the low energy side at about 260 eV. Examples of the second group are shown in figs. 12 and 13 corresponding to diamond and silicon carbide.

The third group represents the Auger KLL spectrum of carbon on the different metal substrates. Figures 14-19 are examples of this Auger carbon spectrum on Ti, V, Cr, Fe, Ni and Cu. All the derivative curves of this group have the shape that has been associated with the presence of a carbide or a form of carbon other than graphite at the surface[1-4].

In the next section a theoretical model of the Auger process is used to analyze the $N(E)$ function of carbon. This analysis reveals how the valence electronic states of carbon are influenced by the presence and the arrangement of neighboring atoms of different types.

THE TRANSITION DENSITY FUNCTION

Once it is possible to express the function $N(E)$ analytically as:

$$N(E) = \sum_{i=1}^n G_1(E) \quad (1)$$

the convolution model discussed in the literature[12-16] can be used to extract the information contained in the $N(E)$ function.

Figure 20 shows the diagram of the Auger process as explained by the convolution model. In this model the Auger electron distribution function $N(E)$ is assumed to be related to some function of the valence band. This function, called the transition density[13,15,16], will depend on the density of states within the band and also on the excitation probability of the allowed transitions. The most usual form of representing the Auger emission process takes the zero energy reference to be the vacuum level. In this scheme the energy of the Auger electron, to a first approximation, is given by:

$$E = E_2 - 2E_1 - \phi . \quad (2)$$

For convenience of the model the zero energy reference is defined to be the Fermi energy level instead of the vacuum level. The energy in the band below the Fermi level is now represented by the variable ζ . The Auger electron leaves the sample with energy $E + \phi$ with respect

to the Fermi level. Then,

$$E + \phi = E_2 - 2\zeta - \phi \quad \text{or}$$

$$E = E_2 - 2(\zeta + \phi) \quad (3)$$

where ϕ is the work function and E_2 represents the ionization energy for some inner level.

Assume that the electrons filling the vacancy in the inner level and the Auger electrons leaving the sample can originate at any energy in the band. Define Δ to be one-half of the initial state separation between the two electrons involved in the transition. It is possible, then, to obtain the total Auger distribution function $F(\zeta)$ by integrating over all Δ 's such that the initial and final states are within the allowed band. Thus

$$F(\zeta) = \int g(\zeta + \Delta)g(\zeta - \Delta)d\Delta \quad (4)$$

will define the transition density $g(\zeta)$. Dividing $F(\zeta)$ into two symmetric parts:

$$F(\zeta) = \begin{cases} F_1(\zeta) = \int_0^{\zeta} g(\zeta + \Delta)g(\zeta - \Delta)d\Delta & [0 \leq \zeta \leq 1/2\zeta_1] \\ F_2(\zeta) = \int_0^{\zeta - \zeta_1} g(\zeta + \Delta)g(\zeta - \Delta)d\Delta & [1/2\zeta_1 \leq \zeta \leq \zeta_1] \end{cases} \quad (5)$$

and changing variables:

$$y = \zeta + \Delta \quad \text{and} \quad x = \zeta - \Delta$$

an expression that is compatible with the theorem of convolution for Laplace transforms can be obtained. This expression is given by:

$$2F_1(t/2) = \int_0^t g(y)g(t-y) dy \quad (6)$$

from which immediately follows:

$$g(y) = 2L^{-1}\{[f(2s)]^{1/2}\} \quad (7)$$

where $f(2s)$ is given by the Laplace transform of the original Auger distribution $N(E)$. Since the direct use of eq.(1) in evaluating $g(y)$ proved to be very difficult, if not impossible, a combination of the procedure used by Amelio and Scheibner[4] and eq.(1) was necessary to obtain the transition density function.

Therefore, if we define:

$$A(E) = mE + b \quad (8)$$

to be a function that represents $N(E)$ in a very small interval ΔE , then the transition density function $g(y)$ will be given by:

$$g(y) = \sqrt{b/2}\{y^{-1/2}e^{-\alpha y}/\Gamma(1/2) + \sqrt{\alpha}\text{erf}(\sqrt{\alpha y})\}. \quad (9)$$

In this expression:

$$\alpha = m/2b ; \quad (10)$$

$$m = [N(E + \Delta E) - N(E)]/\Delta E ; \quad (11)$$

$$b = [N(E)(E + \Delta E) - N(E + \Delta E)(E)]/\Delta E \text{ and} \quad (12)$$

$$y = E/2 . \quad (13)$$

Also:

$$\Gamma(1/2) = \sqrt{\pi} . \quad (14)$$

INITIAL RESULTS

The results of this first approximation are shown in figs. 21-23. In all the cases, with the exception of titanium, the transition density function of carbon appeared to be a continuous function, thus implying the existence of a band-like distribution of states. Also it can be seen in this first approximation that there are important differences between transition density functions as the carbon changes its crystal structure in going from graphite to silicon carbide and as the metal matrix in which the carbon is a foreign impurity changes from titanium to copper.

For comparison purposes, the $dN(E)/dE$ and the $N(E)$ curves of the valence band of polycrystalline Ni were obtained. These curves and the gaussian components of the $N(E)$ function are shown in fig. 24. The good agreement between the calculated transition density for the valence band of nickel as obtained from Ion-Neutralization Spectroscopy (INS) [17] compared to the one obtained by evaluating the function $g(y)$ from the data supplied by Auger Electron Spectroscopy (AES) is shown in fig. 25. The agreements in this case and also in the case of the band structure of diamond (not shown) are fairly good. The transition density of the graphite agrees also, in the general features, with the calculation of Painter and Ellis [18].

THE UNBROADENED AUGER FUNCTION $A(E)$

Because of the low concentrations of carbon on the metal films, the existence of valence bands associated with carbon is questionable. In Auger spectroscopy instrumental broadening is a real phenomenon which has been the subject of several studies[8,10,19]. The appearance of valence bands could be an artifact caused by signal broadening. Therefore, the effect of signal broadening was studied by computer simulating the instrumental broadening of single atom Auger transitions. Those transitions were assumed to be represented by extremely narrow gaussian functions. The width of these initial functions was increased from 0.01 to 0.8 of the experimental value for the gaussian components of $N(E)$. The results showing how a band-like structure is generated from discrete transitions, are presented in figs. 26 and 27 for the cases of pyrolytic graphite and of carbon on nickel. In these figures the curves labeled a, b, c, d, e, and f correspond to the cases in which the width of the gaussian functions simulating the transitions was equal to 0.01, 0.1, 0.2, 0.4, 0.6, and 0.8 of the width of the original gaussian components of $N(E)$ respectively.

To solve the problem of instrumental broadening the procedure suggested by Mulaire and Peria[19] was used in the following way:

Let the functions $A(E)$ and $N(E)$ represent the unbroadened and experimentally measured Auger electron

distributions. Let the function $B(E)$ contain the cumulative broadening effects inherent to instrument and Auger process. Evaluate $B(E)$ from the broadening of the elastic peak assuming that this peak would be a delta function if there were no instrumental broadening effects. Calculate then the desired function $A(E)$ from:

$$A(E) = F^{-1}(F(N(E))/F(B(E))) \quad (15)$$

F^{-1} = Inverse Fourier Transform.

To obtain the unbroadened function in our case, we proceeded as follows:

$$F(x) = (1/\sqrt{2\pi}\sigma) e^{-\left[\frac{x - \mu}{\sqrt{2}\sigma}\right]^2} \quad (16)$$

Since:

$$f(\lambda) = \int_{-\infty}^{\infty} \frac{e^{-i\lambda x}}{\sqrt{2\pi}\sigma} e^{-\left[\frac{x - \mu}{\sqrt{2}\sigma}\right]^2} dx \quad (17)$$

then;

$$f(\lambda) = e^{-(\sigma^2 \lambda^2 / 2 + i\lambda\mu)}. \quad (18)$$

Recalling from eq. (1) that:

$$N(E) = \sum_{i=1}^n G_i(E)$$

and defining the elastic peak $B(E)$ function by:

$$B(E) = [1/\sqrt{2\pi}\sigma_e] e^{-(E - \mu_e)^2/2\sigma_e^2} \quad (19)$$

we can solve eq. (15) for each one of the components of the function $N(E)$ and obtain:

$$a_i(\lambda) = e^{cb} \quad \text{where } c = (\sigma_e^2 - \sigma_i^2)/2 \quad (20)$$

and

$$b = \lambda^2 + 2i\lambda(\mu_e - \mu_i)/(\sigma_e^2 - \sigma_i^2) .$$

Taking now the inverse transform of $a_i(\lambda)$ we obtain:

$$A_i(E) = [2\pi(\sigma_i^2 - \sigma_e^2)]^{-1/2} \exp\left\{-\frac{1}{2} \frac{\sigma_i^2 - \sigma_e^2}{[\sigma_e^2 - \sigma_i^2]^2} [(\mu_e - \mu_i) + E]^2\right\} \quad (21)$$

Each one of the new components is then evaluated separately by setting $\mu_e = \mu_i$. Finally the unbroadened Auger function $A(E)$ will be expressed by:

$$A(E) = \sum_{i=1}^n G_i(E) = \sum_{i=1}^n [1/\sqrt{2\pi}\sigma] e^{-(E - \mu_i)^2/\sigma^2} \quad (22)$$

with: $\sigma = (\sigma_i^2 - \sigma_e^2)^{1/2}$

and where the $G_i(E)$ gaussians are given by the unbroadened components $A_i(E)$ after they have been returned to their original positions.

RESULTS WITHOUT INSTRUMENTAL BROADENING

Figures 28-32 show the newly calculated function $A(E)$. The importance of the gaussian components becomes now more apparent as the new Auger $A(E)$ function reveals more detailed structure.

The transition density function was evaluated again using the unbroadened function $A(E)$. Figure 33 shows a comparison between the new transition density without instrumental broadening and the results obtained from other techniques as reported by McFeely et al[20]. Figures 34-37 contain the results in the transition densities evaluated without the broadening.

For the cases of graphite, silicon carbide, diamond and the graphitic carbon on cobalt the transition density is still a continuous function, thus retaining its band character. The transition density is almost continuous for carbon on copper when the carbon Auger $dN(E)/dE$ function is of the graphitic form. This could be explained by the low solubility of carbon in copper so that the concentration of carbon was smaller than in the case of carbon on cobalt, for example. (See Table I).

In the cases of the metals substrates generating a carbon Auger $dN(E)/dE$ signal with fine structure, the transition density functions in figs. 36 and 37 show discrete transitions, V, Cr, and Ni being the best examples. This fact, together with the low carbon concentrations, strongly suggests the existence of

atomic-like transitions.

The correspondence of these transitions to the ones calculated by Siegbahn et al.[21] is shown in figs. 38-41. In these figures the column listed as "theory" contains the carbon Auger transitions as calculated by Siegbahn et al.[21]. The remaining columns show the carbon KLL transition energies which were determined experimentally for the different cases. The length of the lines representing the transitions corresponds to their relative signal strengths. The signal strength of the transition occurring near 265 eV was taken as unity. The energies at which these transitions occur correspond almost exactly to the maxima of the unbroadened Auger Function $A(E)$.

In fig. 42 the relation of the experimentally determined transitions with the values given in ref. [21] is plotted as a function of the atomic number. The zero reference for ΔE was chosen to be the energy of the KL_1L_2 transition for all the cases. This choice was made on the assumption that the innermost valence level energy would be least affected by the bonding mechanism. In this figure we observe two well defined trends of the KLL transitions of carbon in the three groups, i.e., Ti, V, and Cr in the first, Fe, Co and Ni in the second and Cu in the third group.

The transitions of the first element of each group agree well with the predicted values. As we progress in atomic number there seems to be a shift on the order

of 2 eV in the energy at which the $KL_1L_{2,3}$ transitions occur. There is a shift up to 5 eV for the next $KL_{2,3}L_{2,3}$ transition. And there appears to be a decrease in the width of the $dN(E)/dE$ Auger spectrum as we increase the atomic number in the first two groups.

It is possible that these effects could be associated with the influence of 3d electrons of the metal matrix in the valence electrons of carbon that has been reported[22], but at this moment we do not have definite proof of this.

It is clear, however, that the shifts in the position of the transitions cannot be associated with the tendency of the metal matrix to form a carbide, as Ti, Fe and Cu appear to be equivalent in respect to the energies at which the Auger transitions were detected to occur. It is well known[23] that Ti and Fe form carbides. But while the carbide of Ti is stable, the carbide of Fe is metastable. Copper does not have a known carbide.

Although changes in the chemical state of an element are considered the main source of modifications in the Auger spectrum, it is also known that plasmon losses can be an important feature[2,24-27].

In the case of graphite, the existence of plasmons at 7 and 29 eV has been reported[2,25]. In the present case, we were not able to detect the 7 eV plasmon in pyrolytic graphite. The amplitude of the 29 eV plasmon was found to have a significant effect only in the very low energy tail of the Auger spectrum.

The energies at which the plasmon losses occur are characteristic of each element and independent of the energy of the primary beam[25,26]. Since we had to deal with different metal substrates, the possibility of plasmon losses from the substrate influencing the shape of the Auger spectrum of carbon was considered. We found that in all cases the ratio of the strongest plasmon peak amplitude to the elastic peak amplitude was always less than 0.1, while the components of the Auger $N(E)$ function, except the one at the lowest energy, had a ratio greater than 0.3 with respect to the more intense component. Therefore, we consider very unlikely that the fine structure changes found in the Auger spectrum of carbon were significantly influenced by plasmon losses.

THE EFFECT OF CONCENTRATION

In fig. 43 we show the effect that an increase of the concentration has on the KLL Auger spectrum of carbon recorded as $dN(E)/dE$. The initial concentration of carbon at the surface of the metal film was approximately 0.12 monolayer and it increased up to 0.25 monolayer. The Auger signal changed as the concentration of carbon was increased going from a carbide-shaped spectrum (see fig. 1) to a graphitic Auger carbon signal. It is highly unlikely that this change in shape can be attributed to breaking of carbide bonds and formation of a graphitic layer as the metal matrix was copper. In view

of the results obtained from the evaluation of the transition densities, this change of shape appears to be caused by carbon leaving the metal matrix and diffusing over the surface to form the graphitic layer as the carbon concentration increased. The same effect was observed for carbon segregation and surface diffusion from a nickel matrix[28].

From diffusion theory, in the case of nickel the surface diffusion process was found to depend on \sqrt{t} . Applying the same model to the case of copper we plotted the Auger yield (area under the $dN(E)/dE$ curve) of carbon versus \sqrt{t} . In this model we assumed the Auger yield to be indicative of the amount of the element present at the surface[3]. The result is shown in fig. 44. The dependence of the process on \sqrt{t} is apparent. This indicates that the change in shape of the Auger spectrum is due to a surface diffusion process and therefore to an increase in the concentration of carbon.

CONCLUSION

Sickafus[15] has demonstrated that fine structure can be generated in the derivative of the Auger $N(E)$ function because of convolution effects. In agreement with his work, we found that changes in the transition density function produced by changes in the concentration of the element being analyzed are reflected in the fine structure of the $dN(E)/dE$ function. We have shown

that a careful evaluation of the transition density after consideration of the instrumental broadening and an estimate of the concentration in the case of impurities are necessary before anything can be inferred from the $dN(E)/dE$ Auger function with respect to the chemical state of elements present in very small quantities. The transition density function and thus the $dN(E)/dE$ curve are strongly affected by the concentration of the element considered and by the nature of the matrix containing the impurity atoms. The transition density function gives useful information about the surface electronic states of materials. This type of information should be of interest in a number of areas of surface science.

REFERENCES

- [1] T.W. Haas and T.J. Grant, Appl. Phys. Letters 16 (1970) 172.
- [2] J.P. Coad and J.C. Riviere, Surface Sci. 25 (1971) 609.
- [3] C.C. Chang, in: Characterization of Solid Surfaces, Ed. P.F. Kane and G.B. Larrabee (Plenum Press, New York-London, 1974) p.509.
- [4] T.W. Haas and D.J. Pocker, J. Vac. Sci. Technol. 11 (1974) 1087.
- [5] N.C. MacDonald, in: Physical Aspects of Electron Microscopy and Microbeam Analysis, Ed. B.J. Siegel and D.R. Beaman (John Wiley and Sons, Inc., 1975) p.431.
- [6] P.W. Palmberg, G.E. Riach, R.E. Weber and N.C. MacDonald, in: Handbook of Auger Electron Spectroscopy, Ed. Physical Electronics Industries, Inc., Edina, Minnesota, 1972.
- [7] L.C. Isett and J.M. Blakely, Report # 2196, Materials Research Center, Cornell University, 1974.
- [8] J.E. Houston, Surface Sci. 38 (1973) 283.
- [9] J.T. Grant, T.W. Haas and J.E. Houston, Phys. Letters 45A (1973) 309.
- [10] F. Meyer and J.J. Vrakking, Surface Sci. 33 (1972) 271.
- [11] E.N. Sickafus, Rev. Sci. Instr. 42 (1971) 933.
- [12] G.F. Amelio, Surface Sci. 22 (1970) 301.
- [13] M. Salmeron, Surface Sci. 41 (1974) 584.
- [14] G.F. Amelio and E.J. Scheibner, Surface Sci. 11 (1968) 242.
- [15] E.N. Sickafus, Phys. Rev. B 7 (1973) 5100.
- [16] J.J. Lander, Phys. Rev. 91 (1953) 1382.
- [17] H.D. Hagstrum, Phys. Rev. 150 (1966) 495.
- [18] G.S. Painter and D.E. Ellis, Phys. Rev. B 1 (1970) 4747.

- [19] W.M. Mulaire and W.T. Peria, *Surface Sci.* 26 (1971) 125.
- [20] F.R. McFeely, S.P. Kowalczyk, L. Ley, R.G. Cavell, R.A. Pollak and D.A. Shirley, *Phys. Rev. B* 9 (1974) 5268.
- [21] K. Siegbahn, C. Nordling, A. Fahlman, et al., in: *Atomic, Molecular and Solid State Structure Studied by Means of Electron Spectroscopy, ESCA (Electron Spectroscopy for Chemical Analysis)*, (Almqvist and Wiksell Boktryckeri AB., Uppsala, 1967) p.234.
- [22] L. Ramqvist, *J. Appl. Phys.* 42 (1971) 2113.
- [23] C.E. Wicks and F.E. Block, *Bulletin 605 (Bureau of Mines, Washington, 1963)*
- [24] A.M. Bradshaw, S.L. Cederbaum, W. Domcke and U. Kraus, *J. Phys. C (Solid State Phys.)* 7 (1974) 4503.
- [25] E.J. Scheibner and L.N. Tharp, *Surface Sci.* 8 (1967) 247.
- [26] L.N. Tharp and E.J. Scheibner, *J. Appl. Phys.* 38 (1967) 3320.
- [27] W.M. Mulaire and T.W. Rusch, *Surface Sci.* 19 (1970) 469.
- [28] J.F. Mojica, to be published.

TABLE I. Approximate carbon coverage of the surface of the metal film.

METAL SUBSTRATE	COVERAGE IN MONOLAYERS OF CARBON
	(Signal: "carbide")
Titanium	0.52
Vanadium	0.28
Chromium	0.10
Iron	0.10
Nickel	0.12
Copper	0.12
	(Signal: graphitic)
Cobalt	1.94
Copper	0.70

Figure 1. Carbon KLL Auger spectra from different materials. A was obtained from silicon carbide. B corresponds to pyrolytic graphite. C was obtained from a vacuum deposited film of nickel in which the carbon was an impurity.

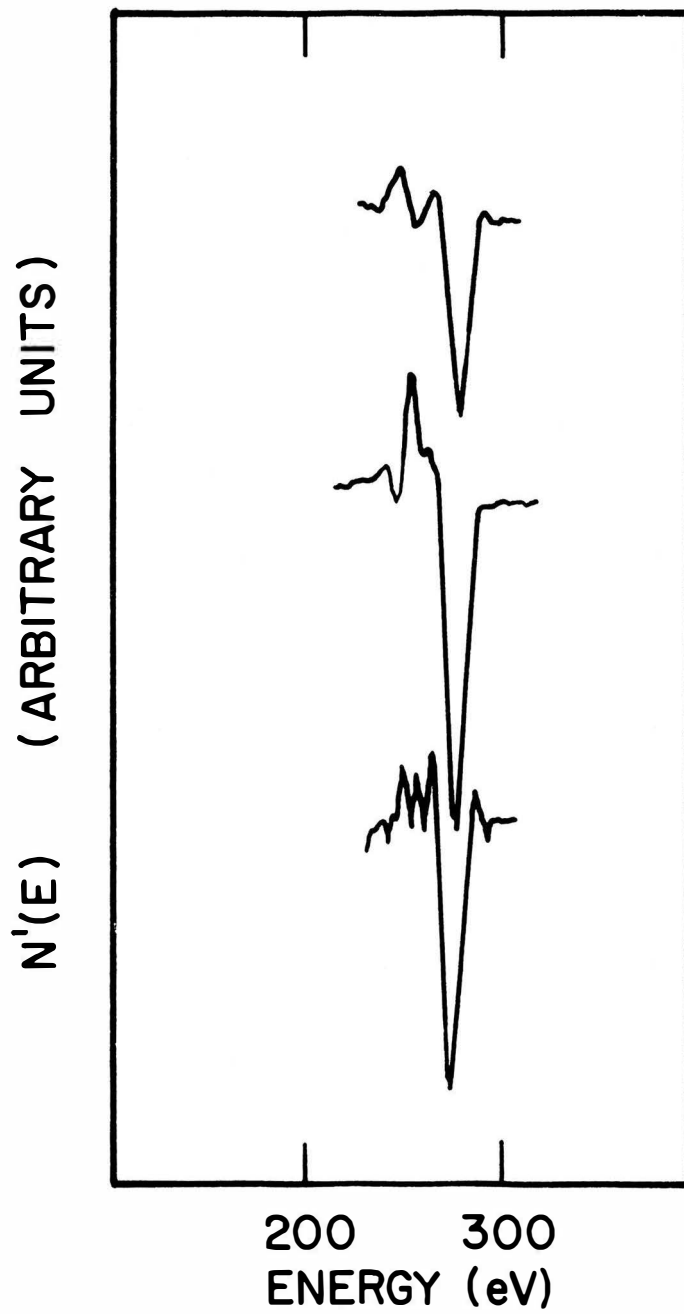


Figure 1

Figure 2. Auger spectrum of a piece of stress-annealed pyrolytic graphite. Spectrum A shows no contamination at the surface. Spectrum B reveals traces of nitrogen and oxygen at the surface.

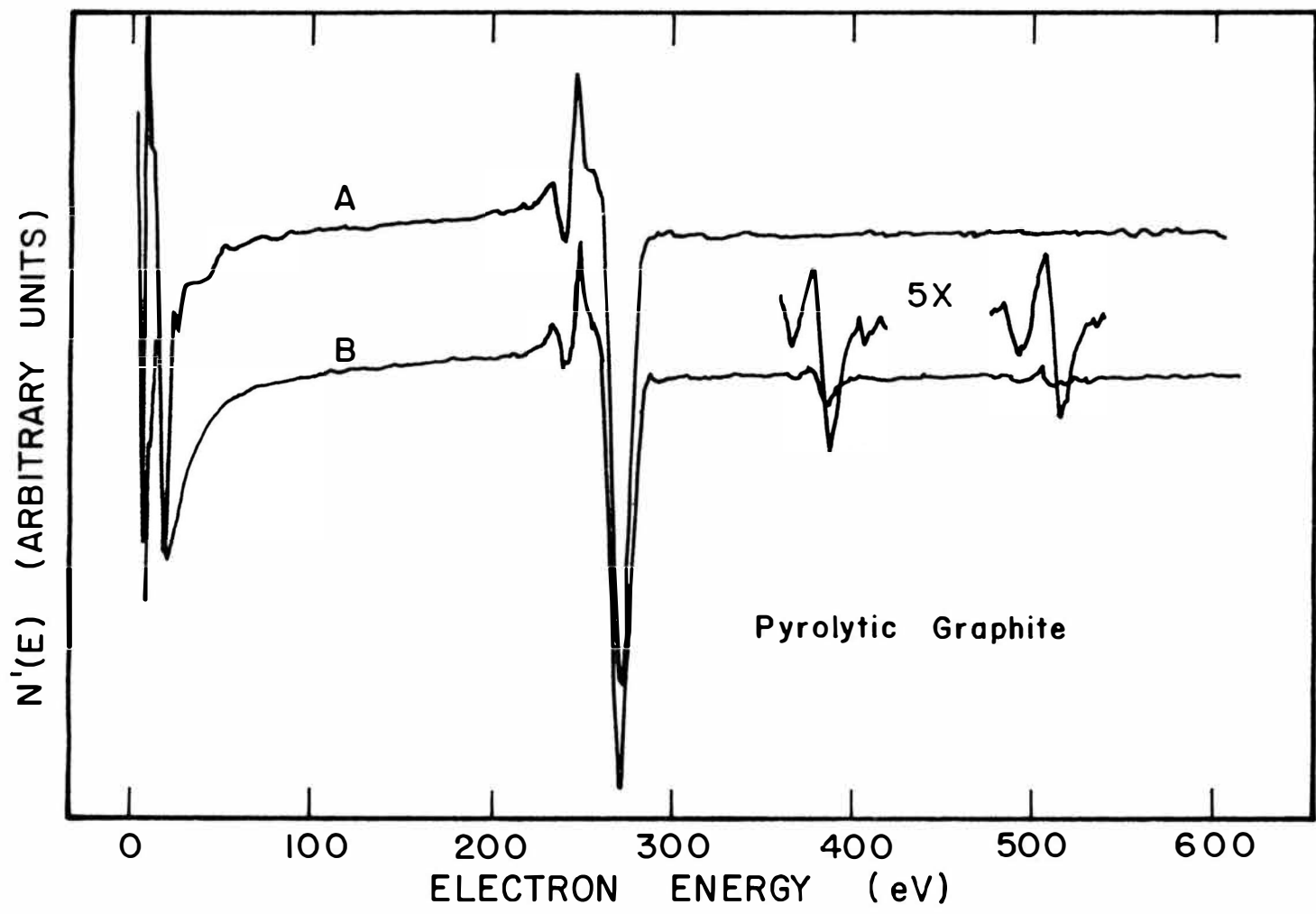


Figure 2

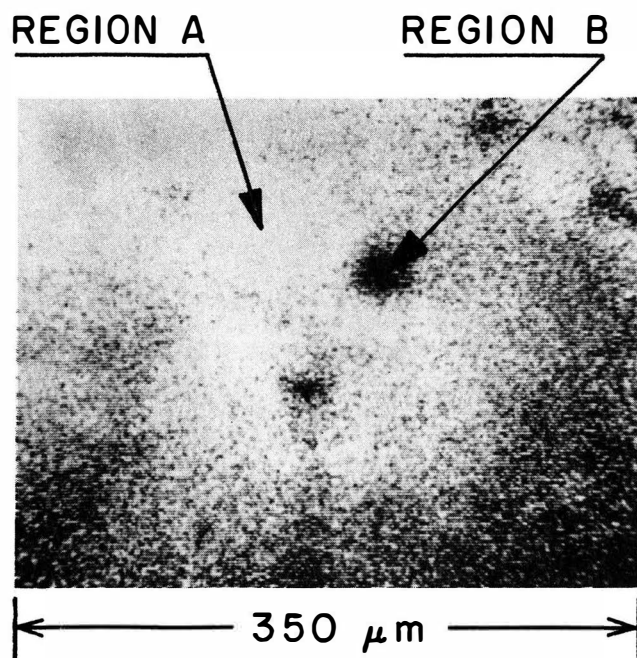
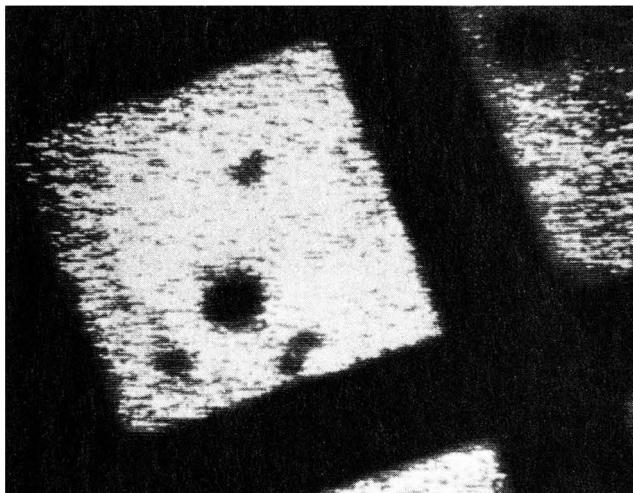
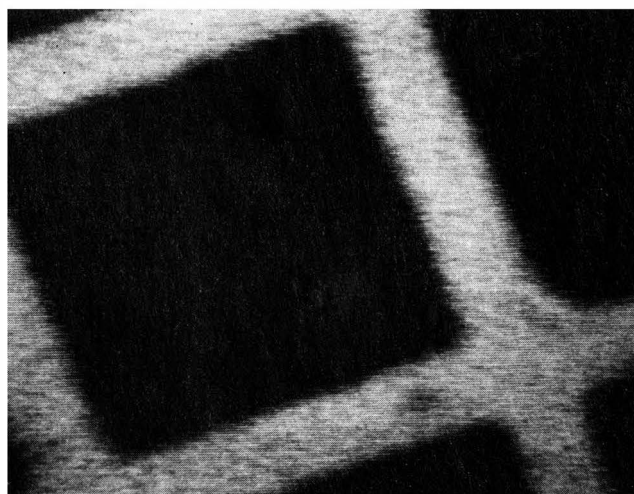


Figure 3. Micrograph of stress-annealed pyrolytic graphite. The dark region B was found to correspond to trace impurities of nitrogen and oxygen.

Figure 4. Micrograph of a sample prepared by vacuum deposition of a chromium film through a gold grid onto pyrolytic graphite. Micrograph A was recorded with the 532 eV minimum of the $dN(E)/dE$ which corresponds to chromium. Micrograph B was taken with the 272 eV minimum that is characteristic of carbon.



A



B

← 350 μm →

Figure 4

Figure 5. Micrograph of the same sample as in fig. 4. The dark regions show the distribution of the 258 and 249 eV maxima of the carbon N(E) Auger curve respectively.

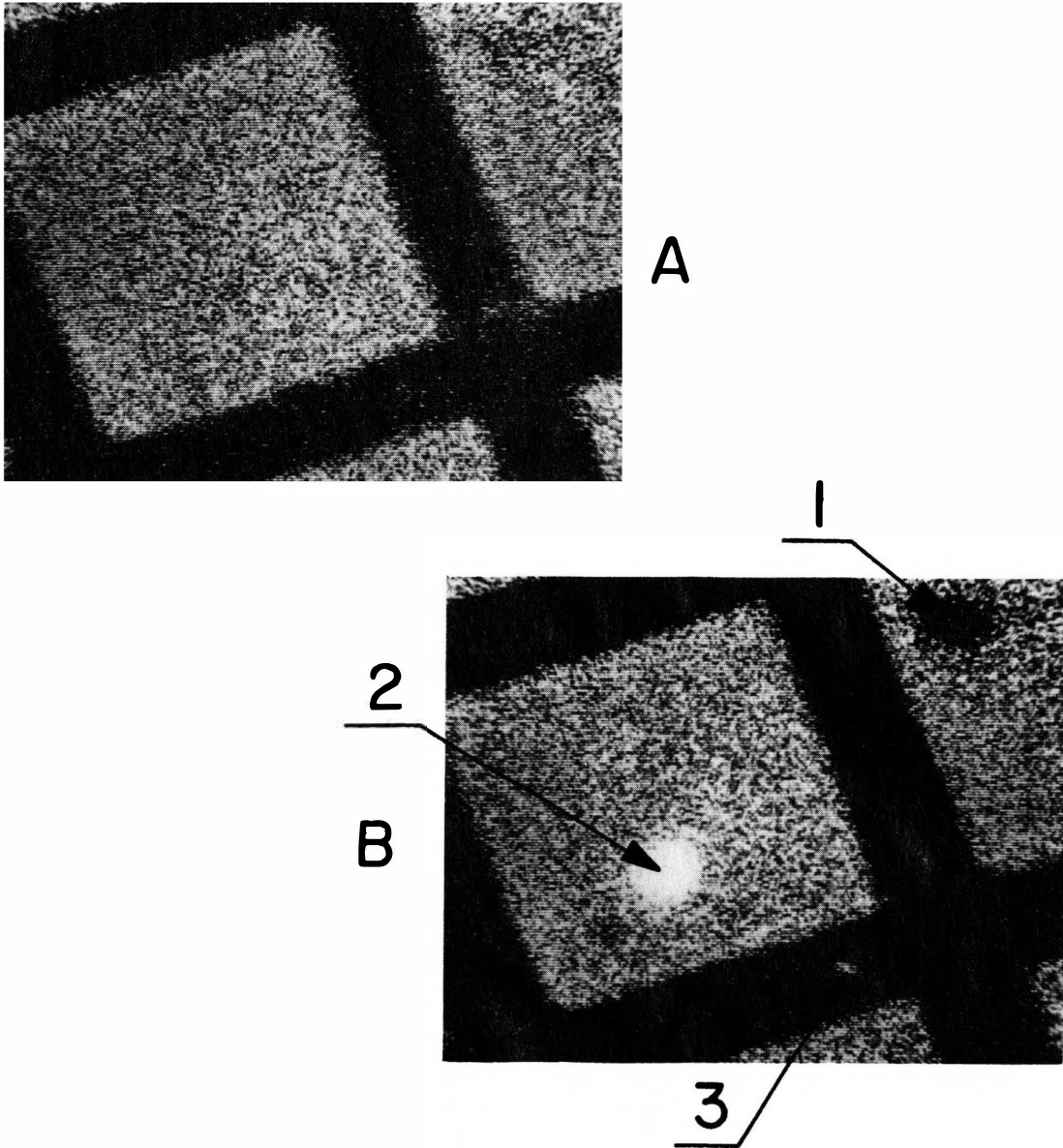


Figure 5

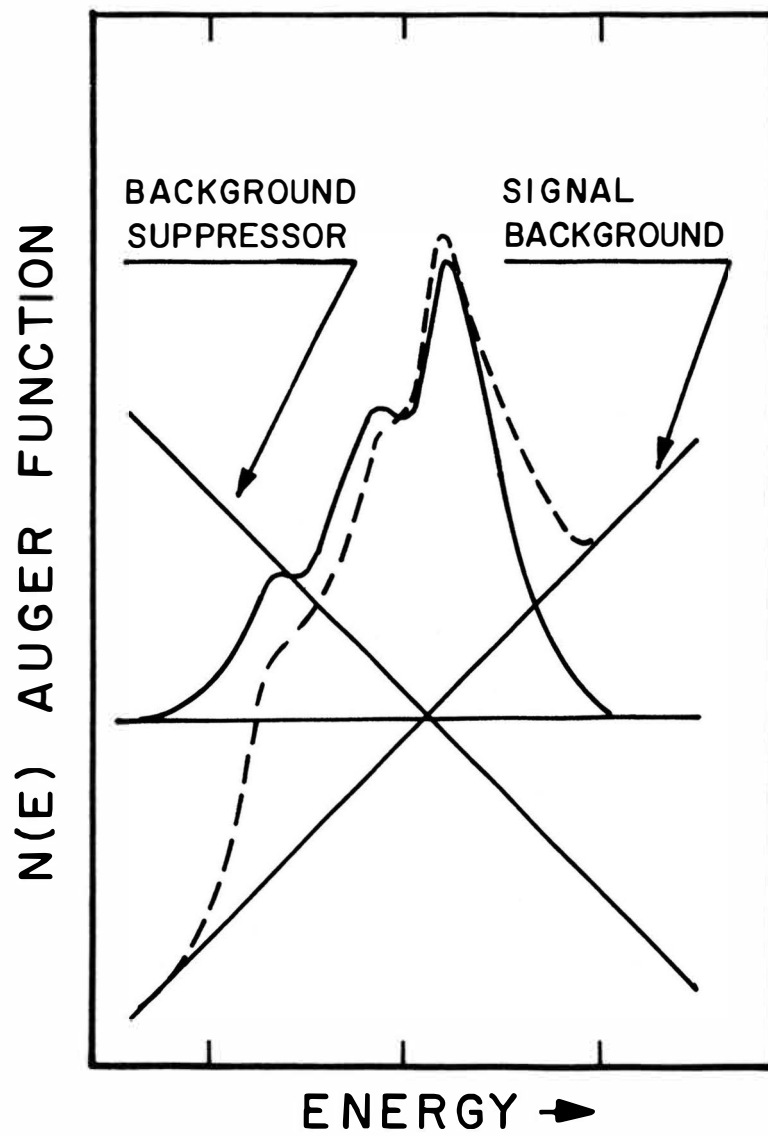


Figure 6. Schematic diagram of the background suppression process.

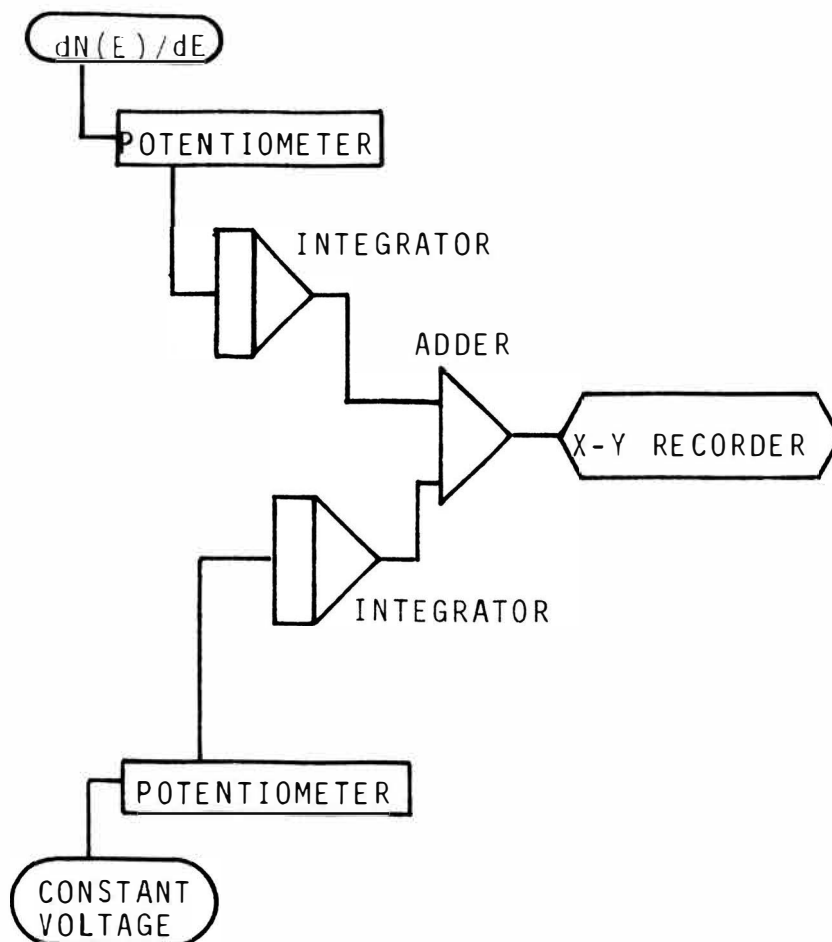


Figure 7. Flow diagram for the process of analog integration of the $dN(E)/dE$ Auger signal with background suppression.

Figure 8. $N'(E)$ and $N(E)$ Auger curves as obtained from the (0001) surface of pyrolytic graphite placed at 90° angle of incidence with respect to the electron beam. Also shown are the gaussian components of the $N(E)$ curve.

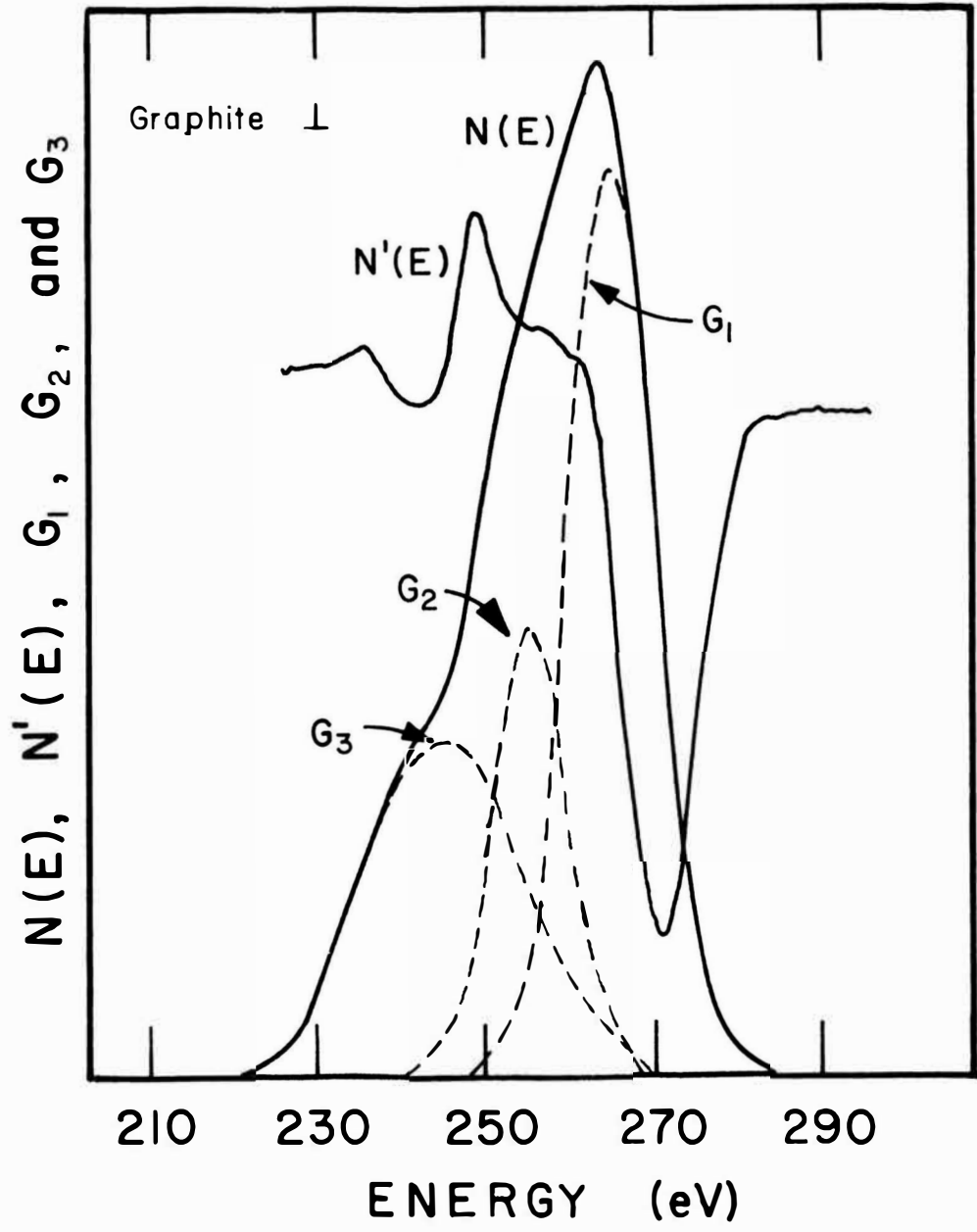


Figure 8

Figure 9. $N'(E)$ and $N(E)$ Auger curves from pyrolytic graphite (0001) placed at 60° angle of incidence with respect to the electron beam. The gaussian components of the $N(E)$ curve are also shown.

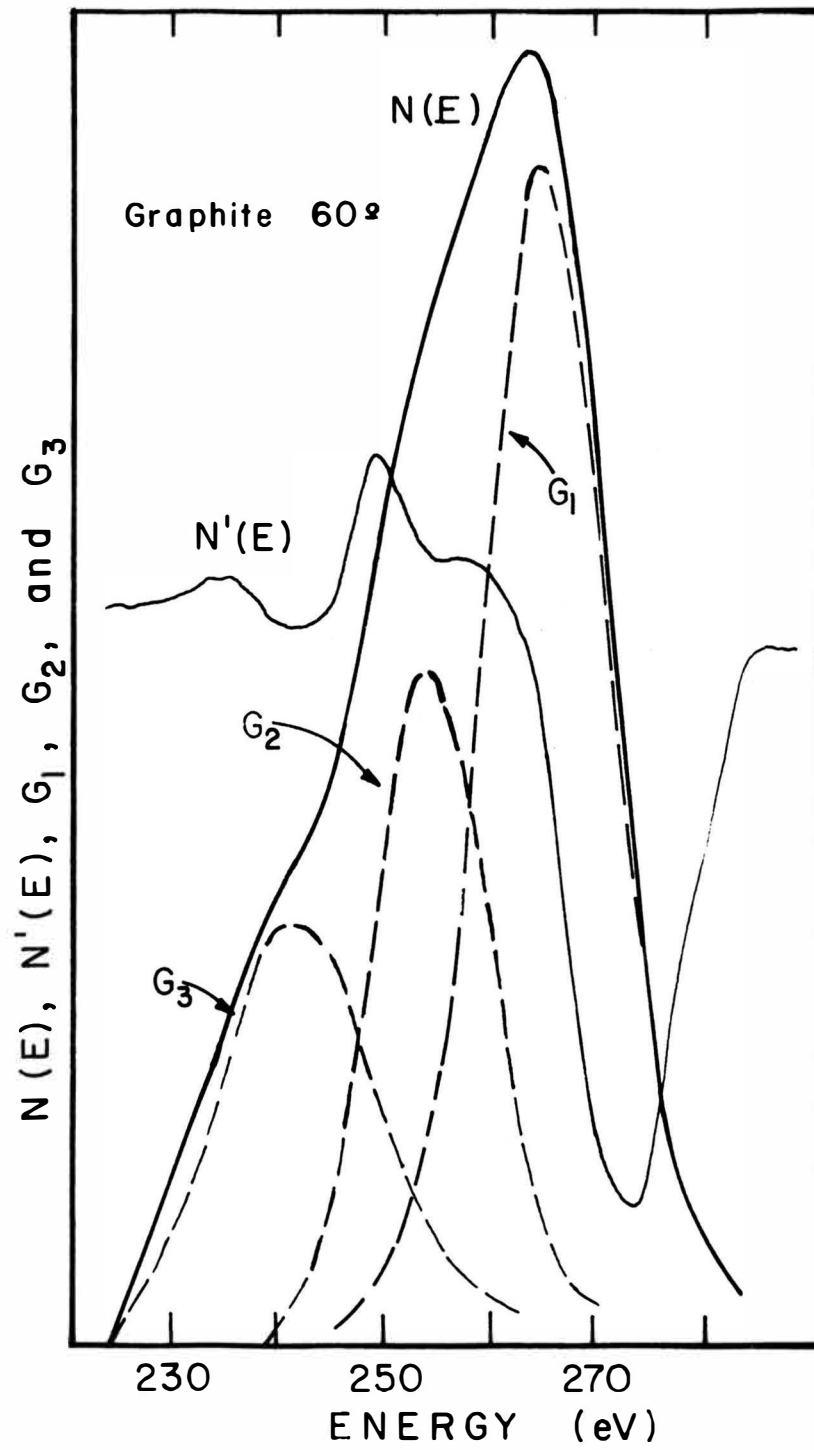


Figure 9

Figure 10. Auger curves $N'(E)$ and $N(E)$ and the gaussian components of $N(E)$ of carbon on cobalt.

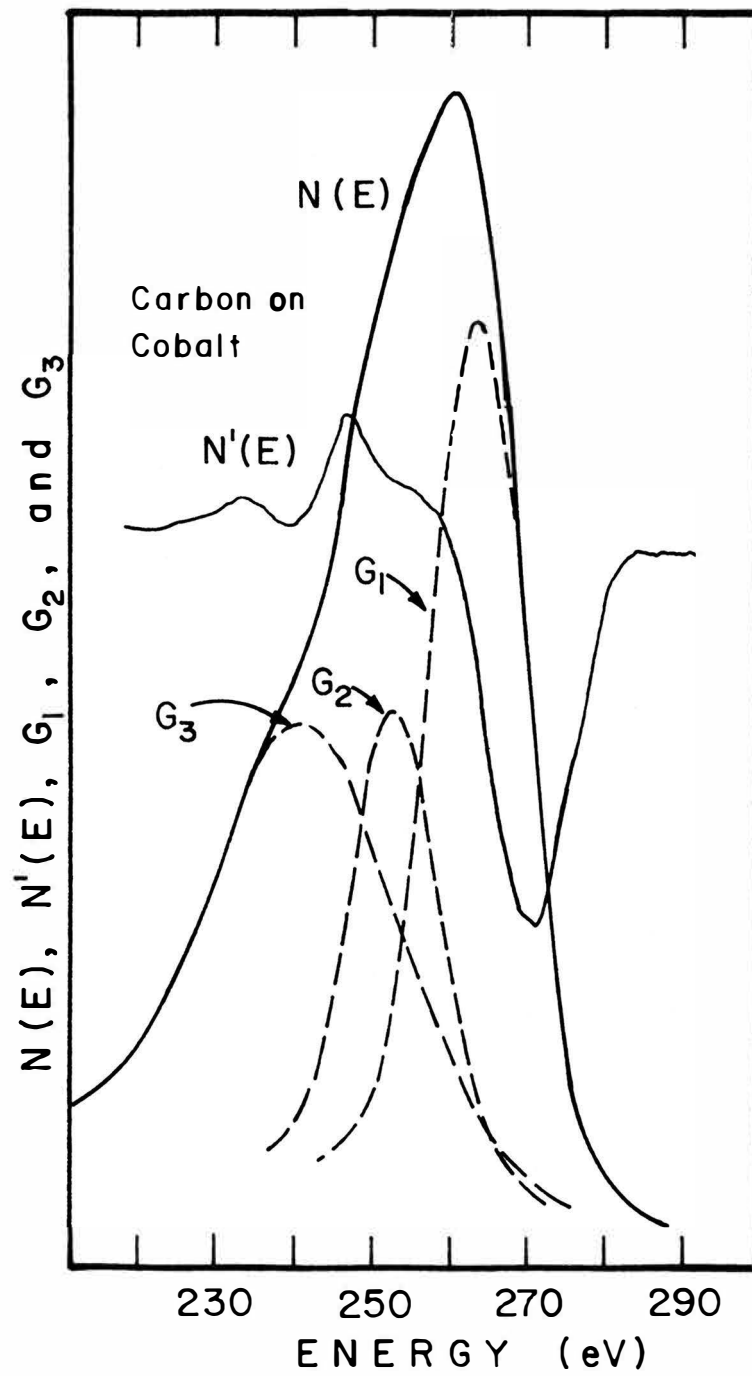


Figure 10

Figure 11. Auger curves $N'(E)$ and $N(E)$ and the gaussian components of the $N(E)$ curve of carbon on copper.

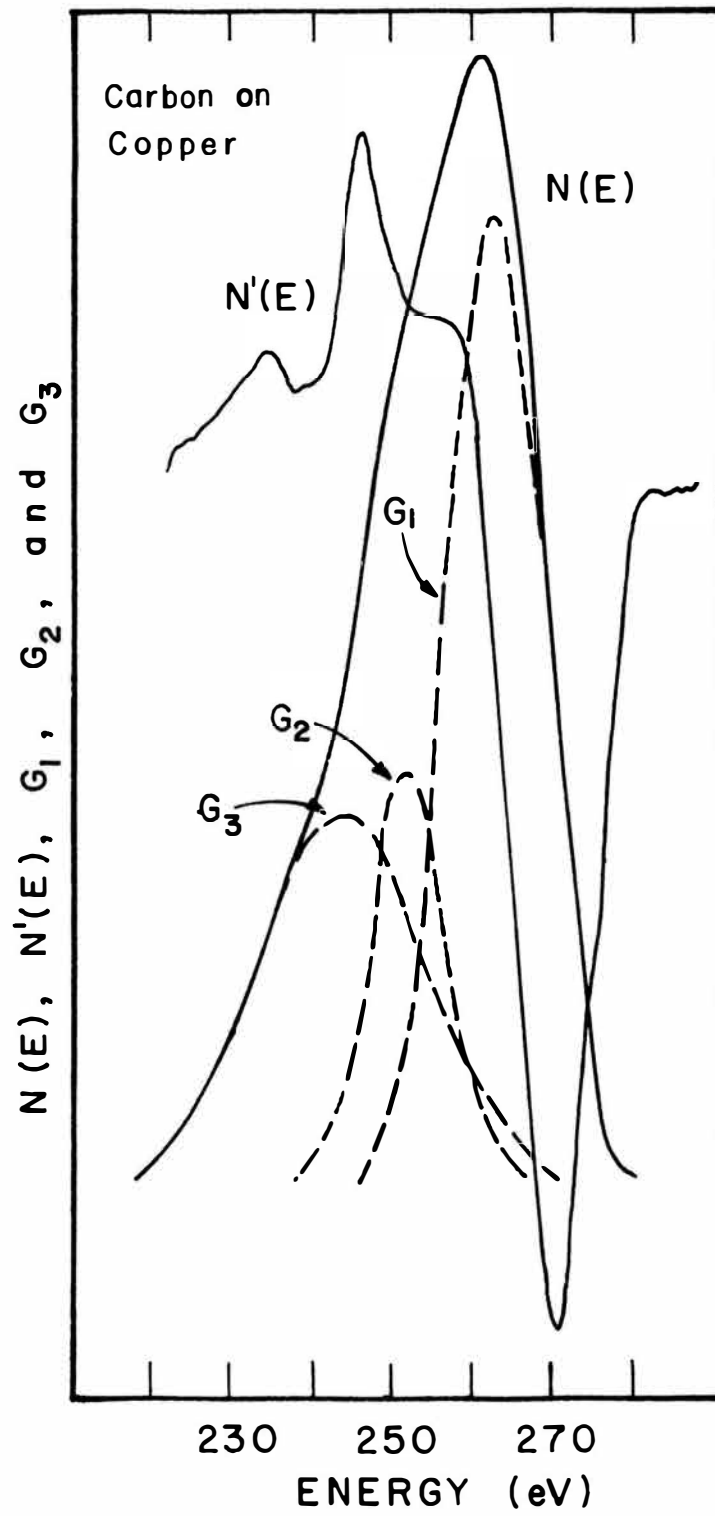


Figure 11

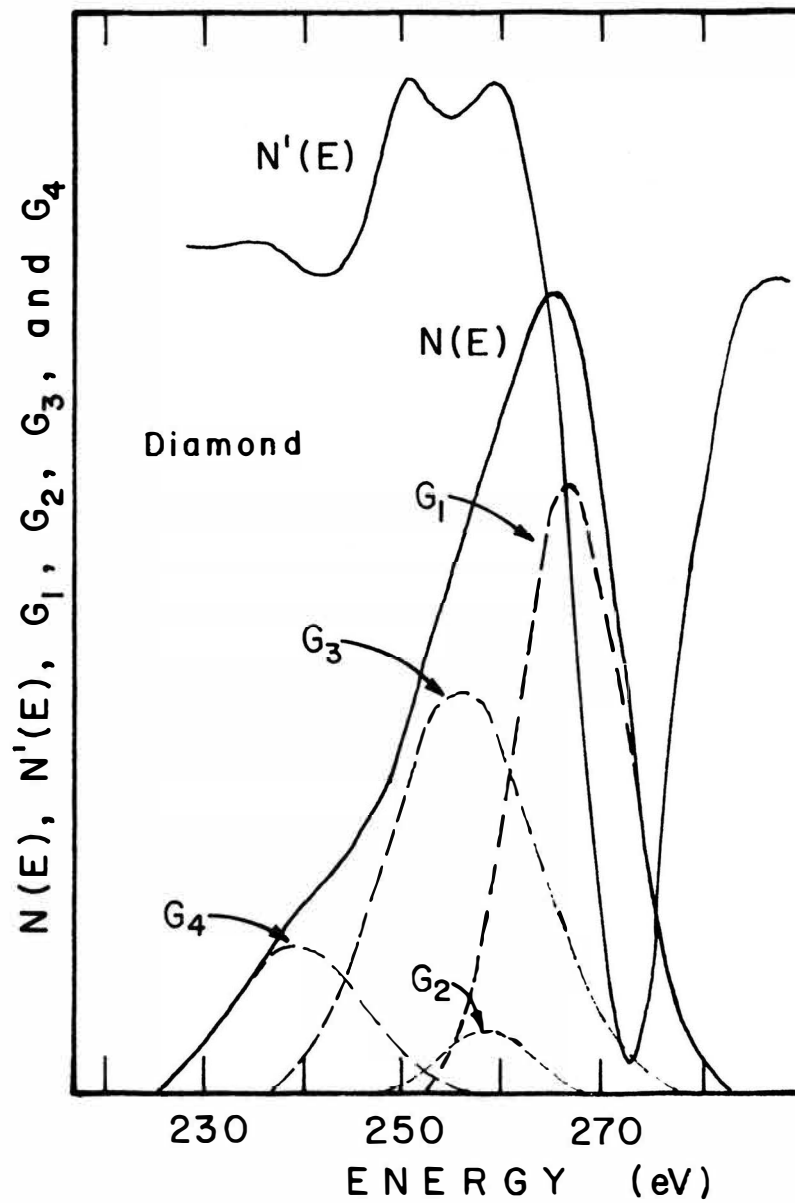


Figure 12. Auger curves $N'(E)$ and $N(E)$ and the gaussian components of the $N(E)$ curve of diamond (111).

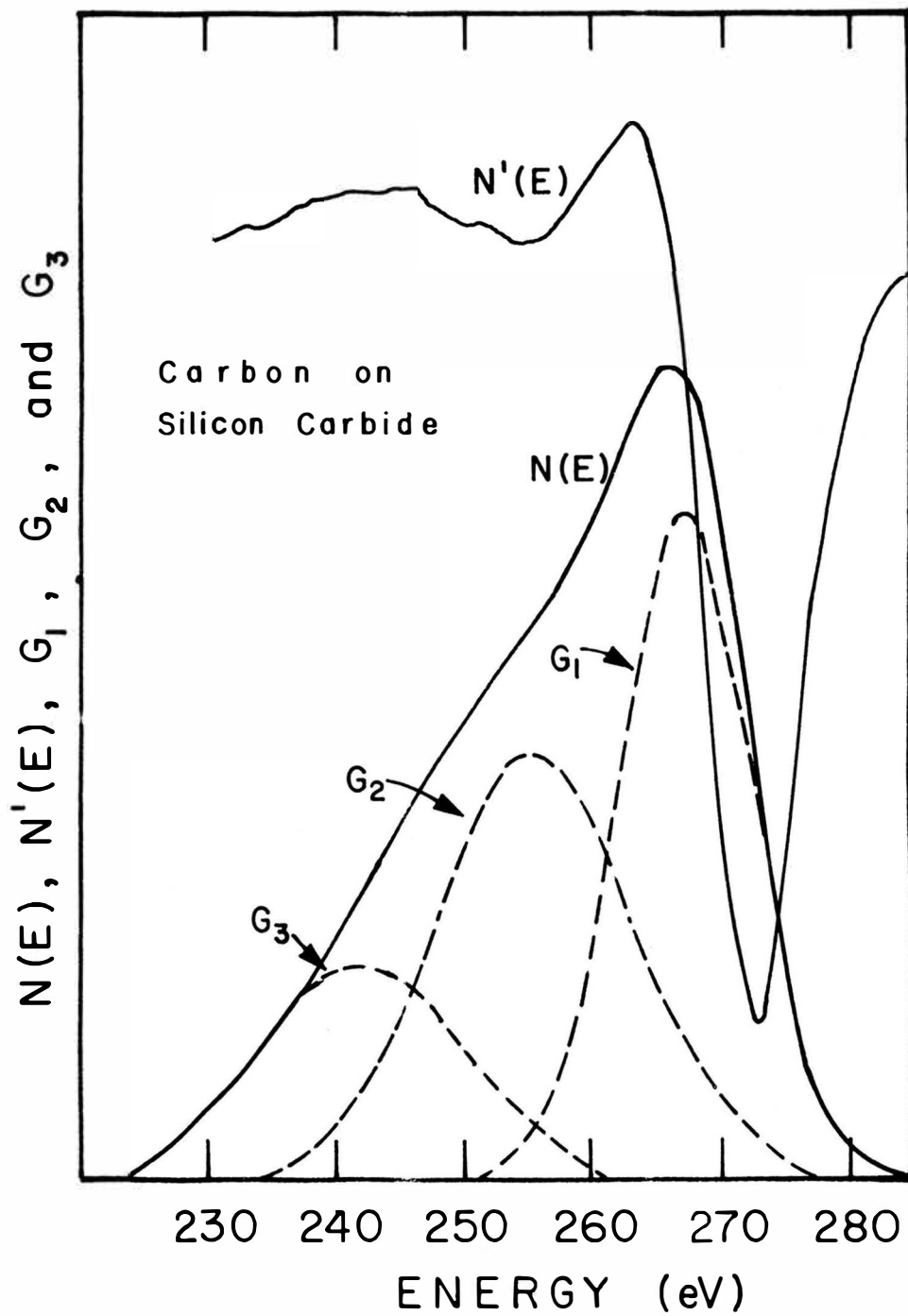


Figure 13. Auger curves $N'(E)$ and $N(E)$ and the gaussian components of the $N(E)$ curve of carbon in silicon carbide.

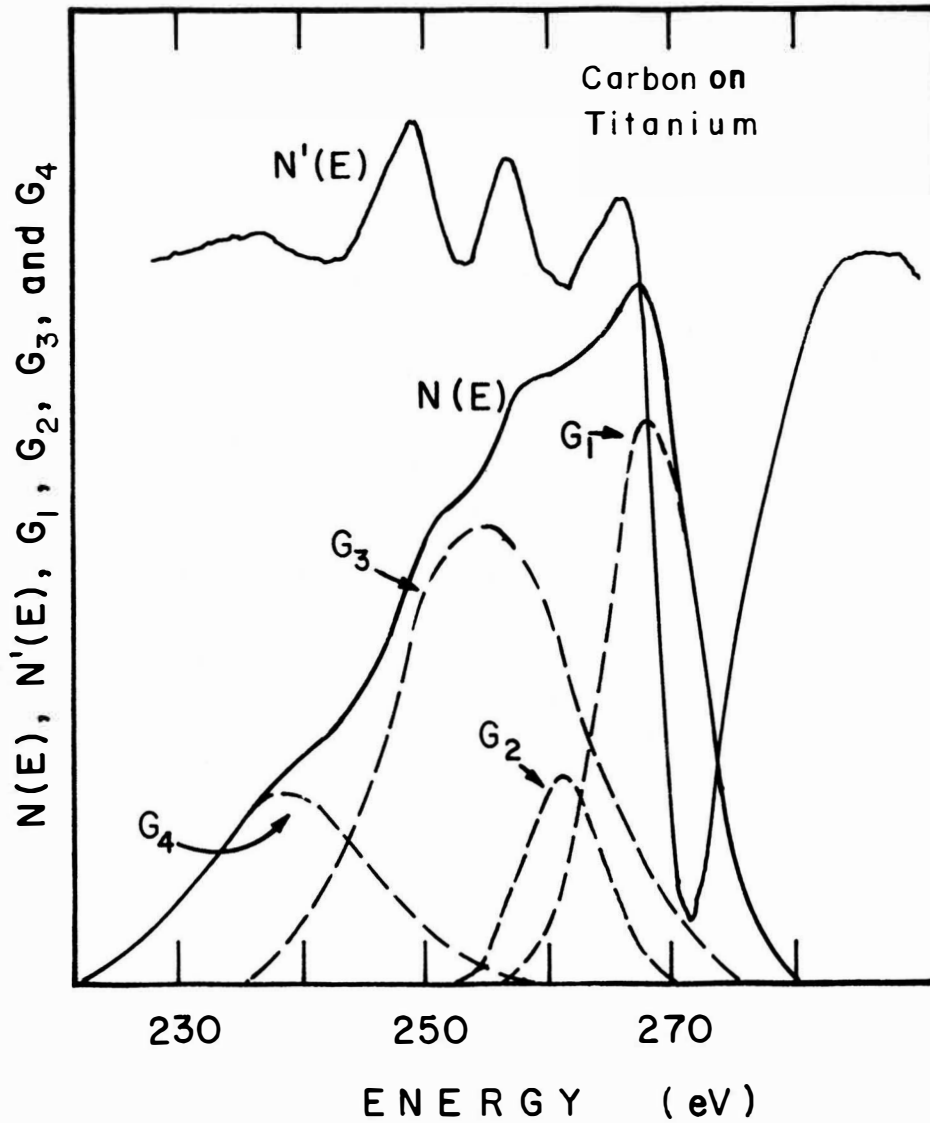


Figure 14. Auger curves $N'(E)$ and $N(E)$ and the gaussian components of the $N(E)$ curve of carbon on titanium.

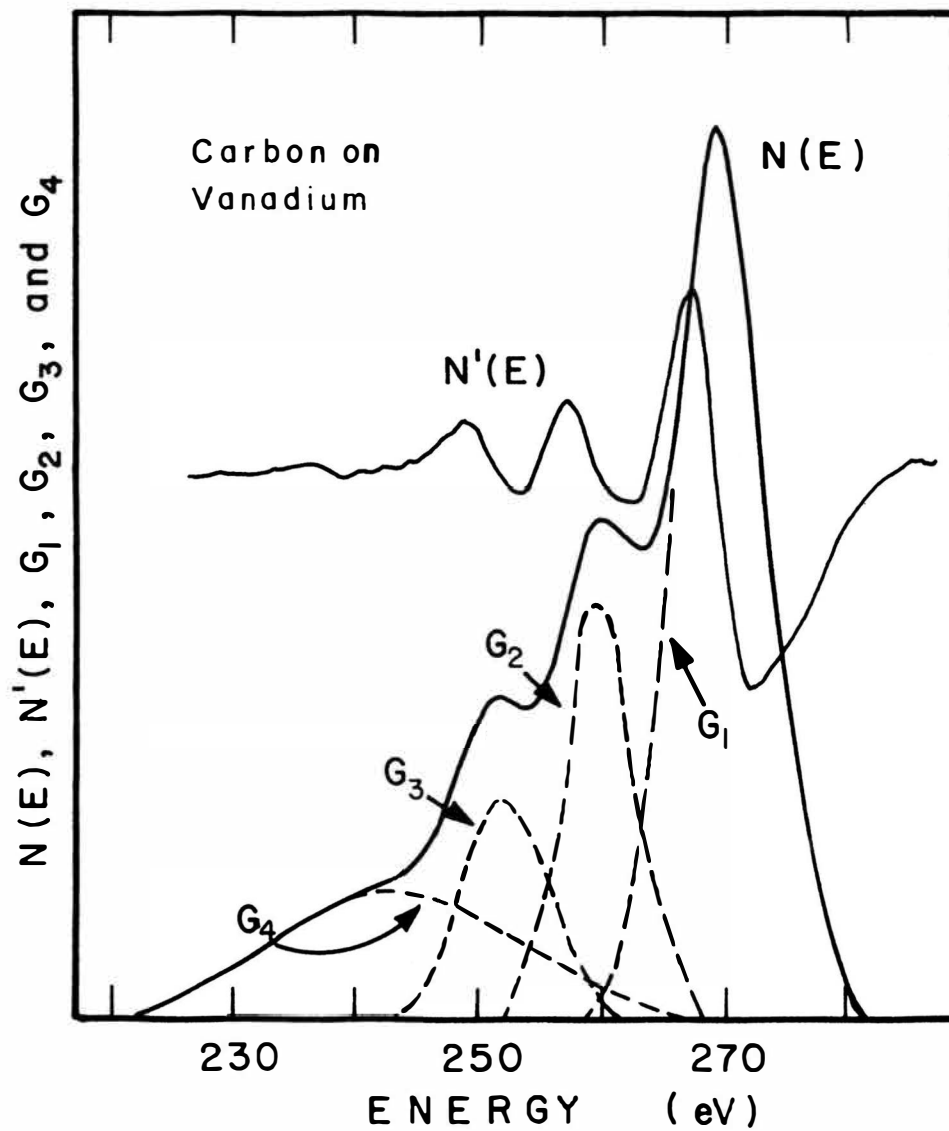


Figure 15. Auger curves $N'(E)$ and $N(E)$ and the gaussian components of the $N(E)$ curve of carbon on vanadium.

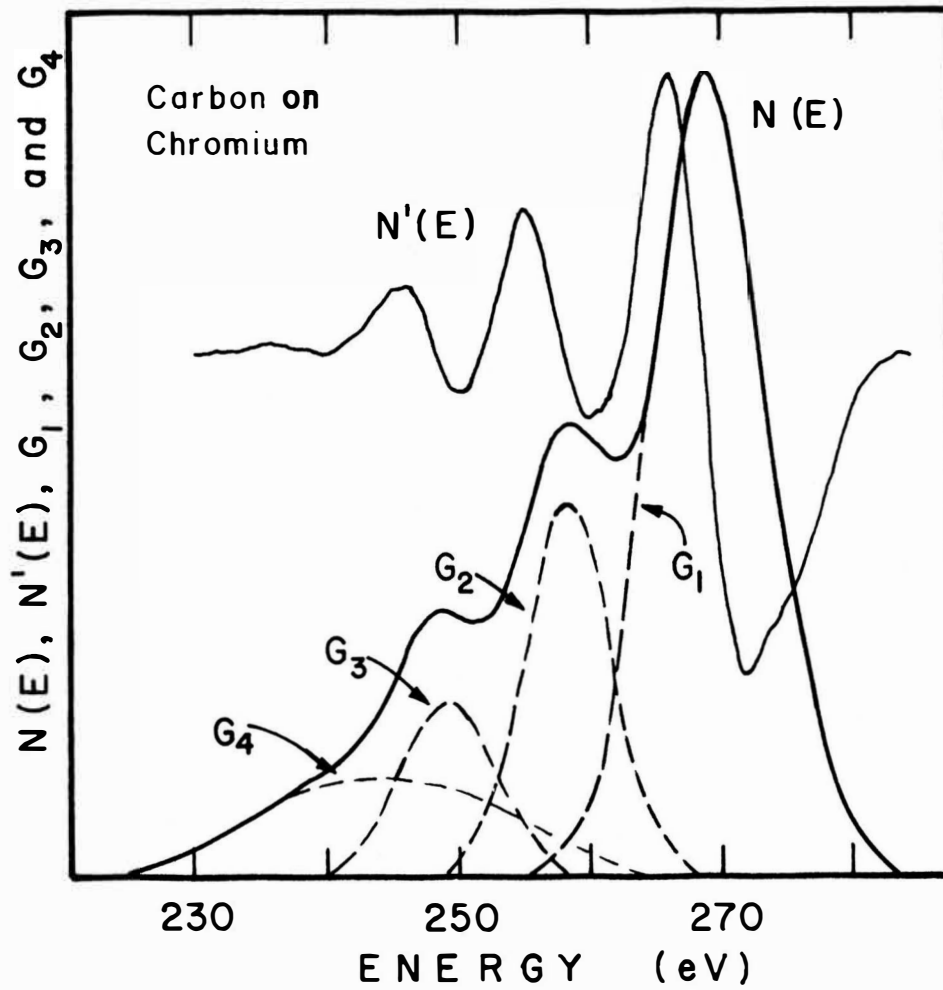


Figure 16. Auger curves $N'(E)$ and $N(E)$ and the gaussian components of the $N(E)$ curve of carbon on chromium.

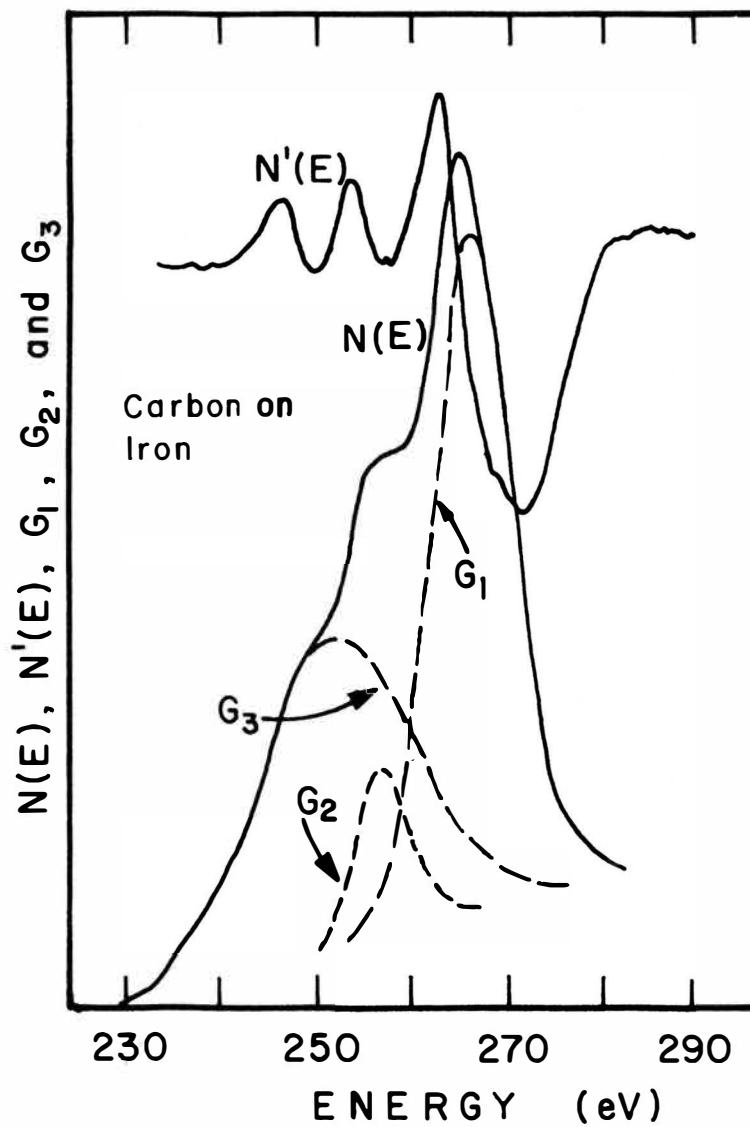


Figure 17. Auger curves $N'(E)$ and $N(E)$ and the gaussian components of the $N(E)$ curve of carbon on iron.

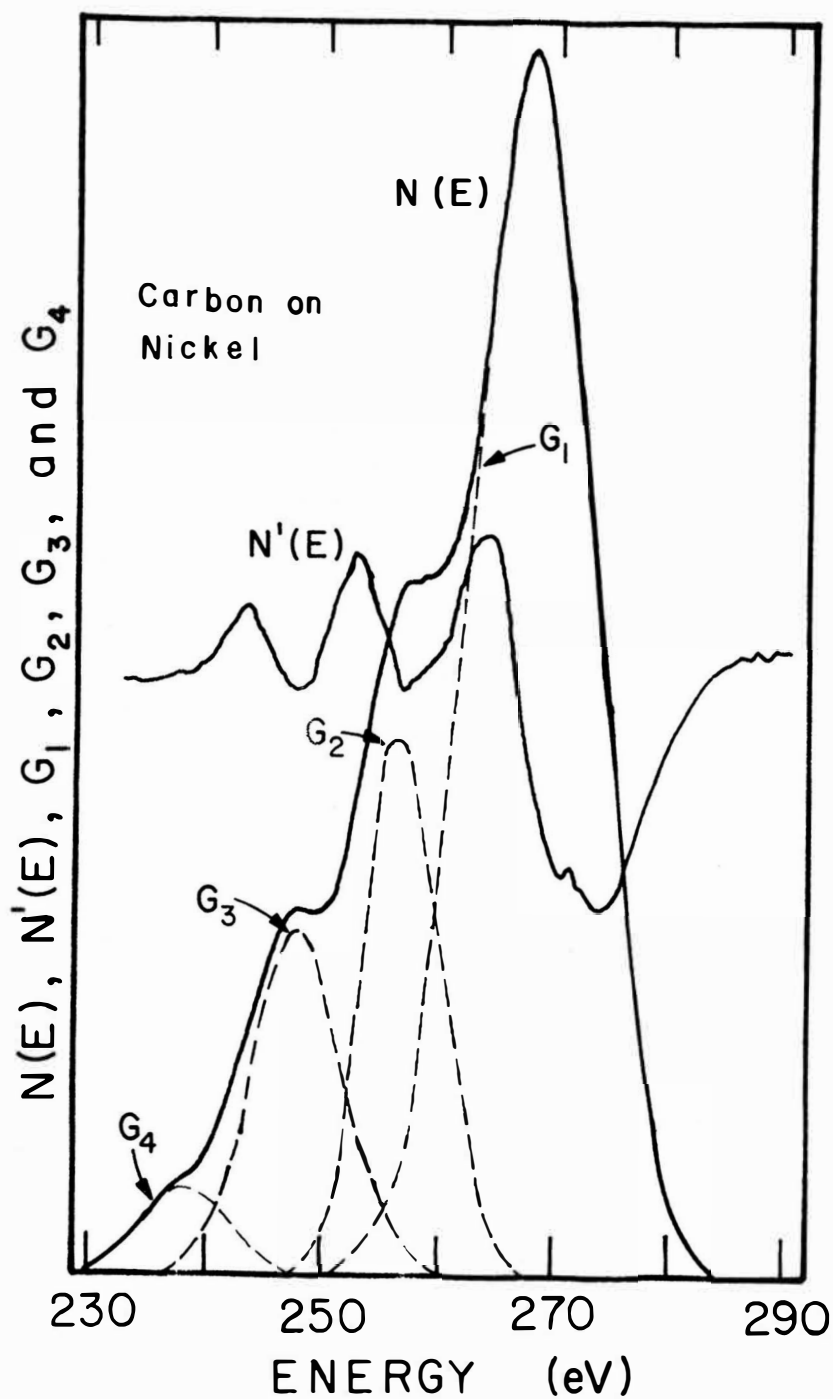


Figure 18. Auger curves $N'(E)$ and $N(E)$ and the gaussian components of the $N(E)$ curve of carbon on nickel.

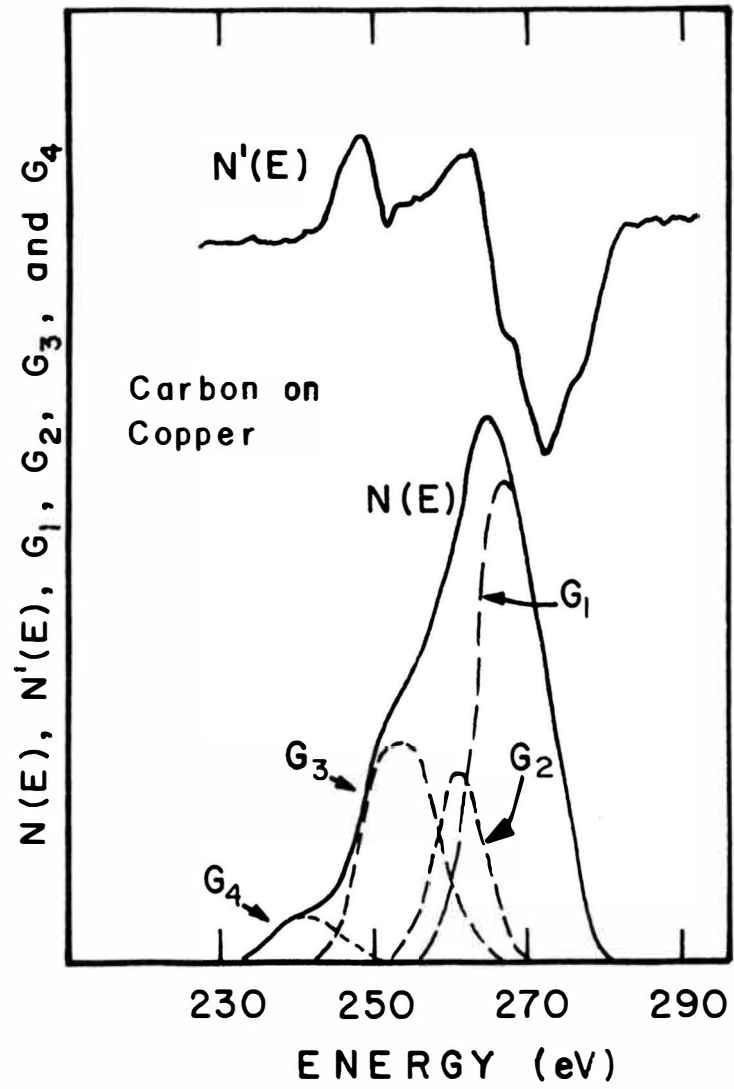


Figure 19. Auger curves $N'(E)$ and $N(E)$ and the gaussian components of the $N(E)$ curve of carbon on copper.

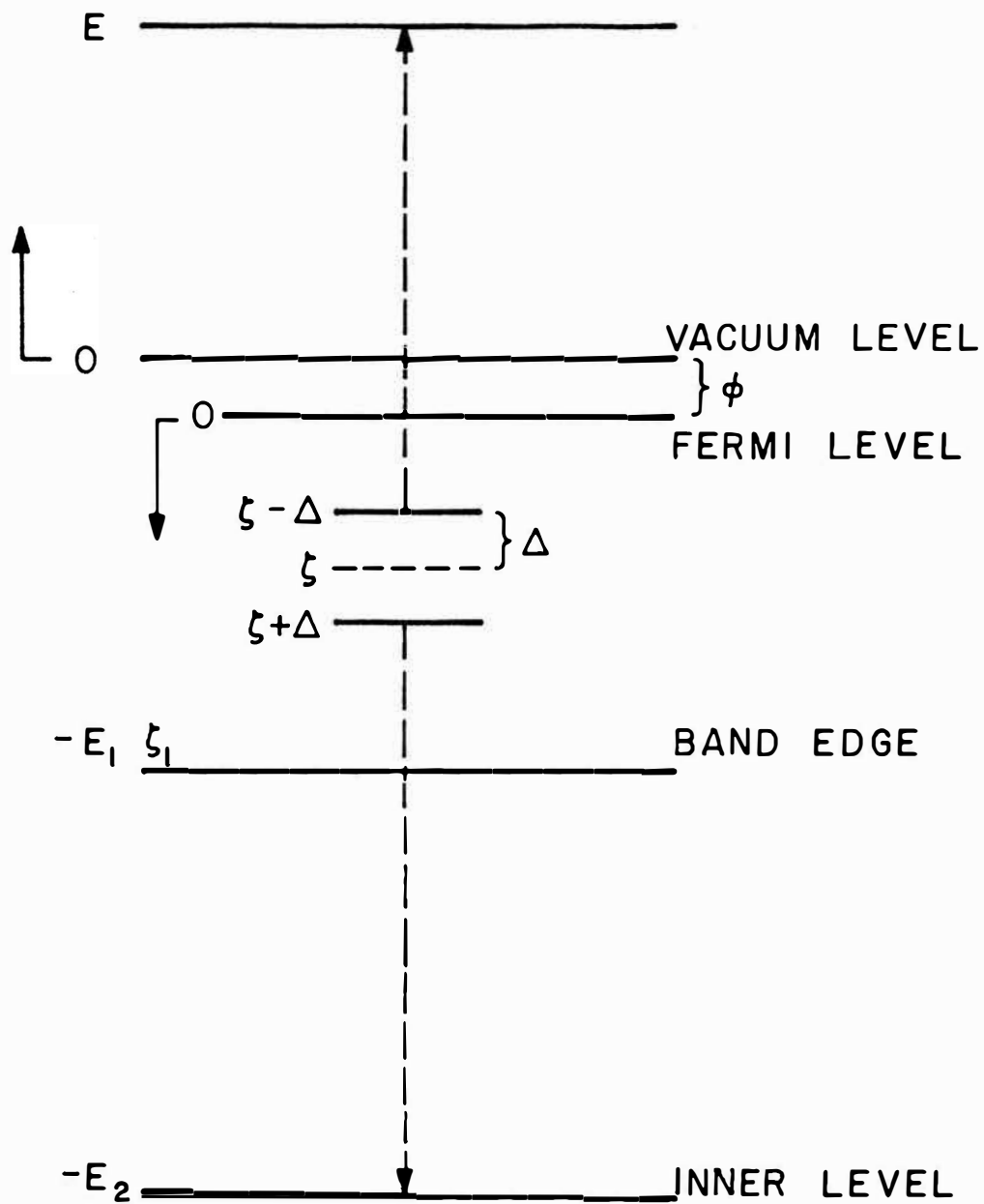


Figure 20. Diagram of the Auger process, ref.[13].

Figure 21. Transition density functions of carbon in pyrolytic graphite (0001) placed at 90° and 60° angles of incidence with respect to the electron beam and also on copper and cobalt as evaluated from the $N(E)$ Auger function.

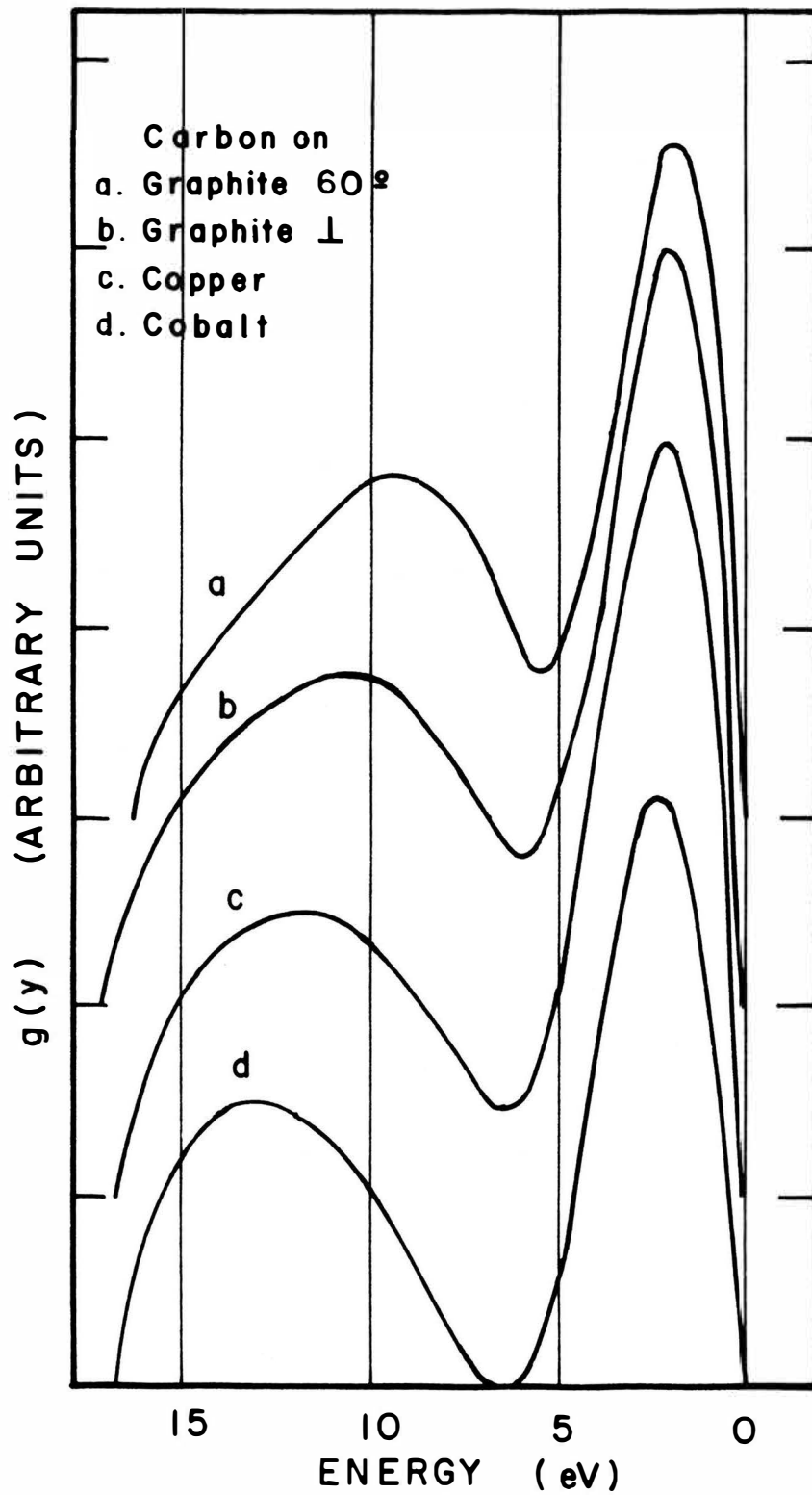


Figure 21

Figure 22. Transition density functions of carbon in pyrolytic graphite (0001) placed at 90° angle of incidence with respect to the electron beam and in silicon carbide. Transition density functions of carbon on titanium, vanadium and chromium are also shown. These functions are evaluated from the $N(E)$ curve.

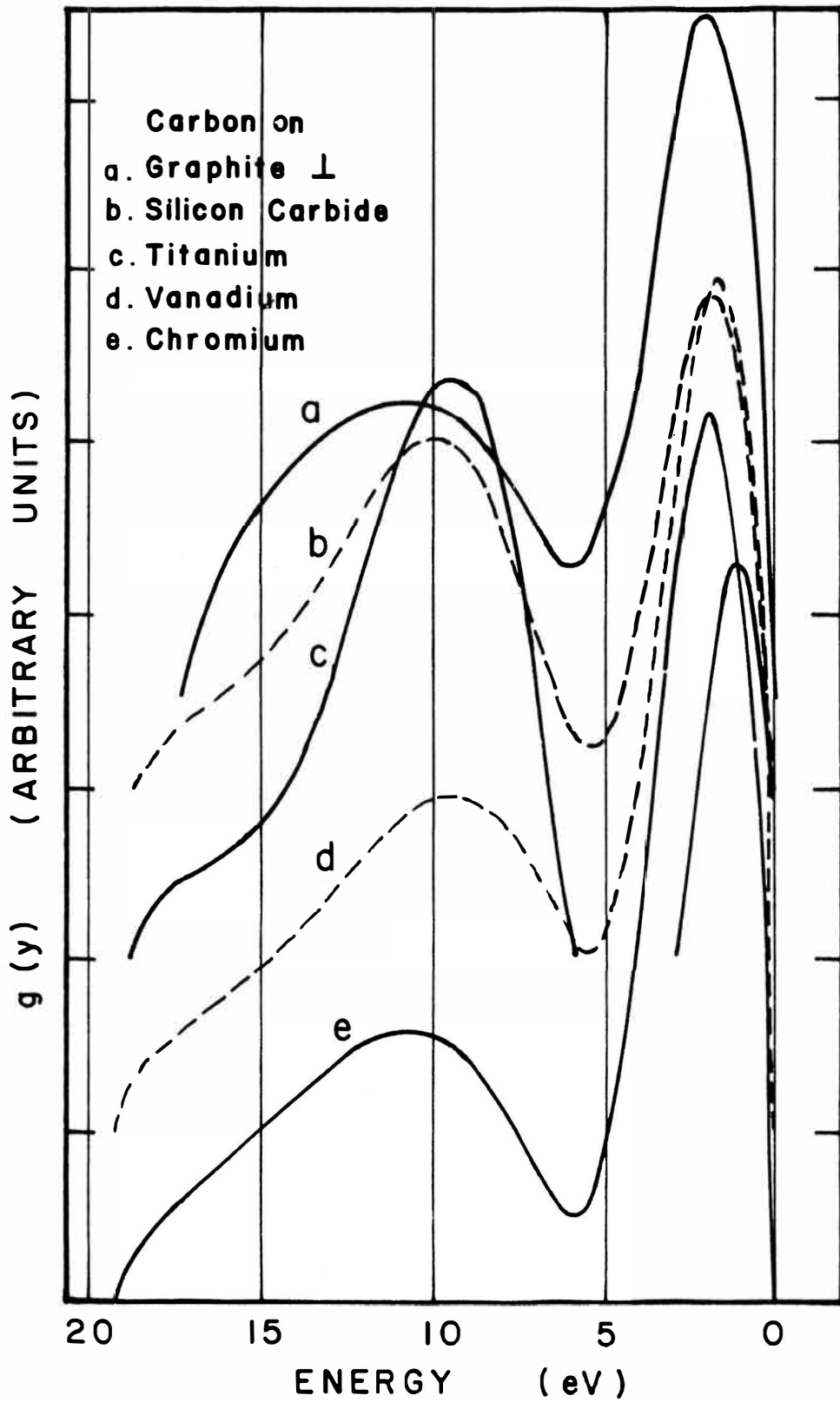


Figure 22

Figure 23. Transition density functions of carbon in pyrolytic graphite (0001) at 90° angle of incidence with respect to the electron beam and on iron, nickel and copper. All these functions are evaluated from the $N(E)$ curve.

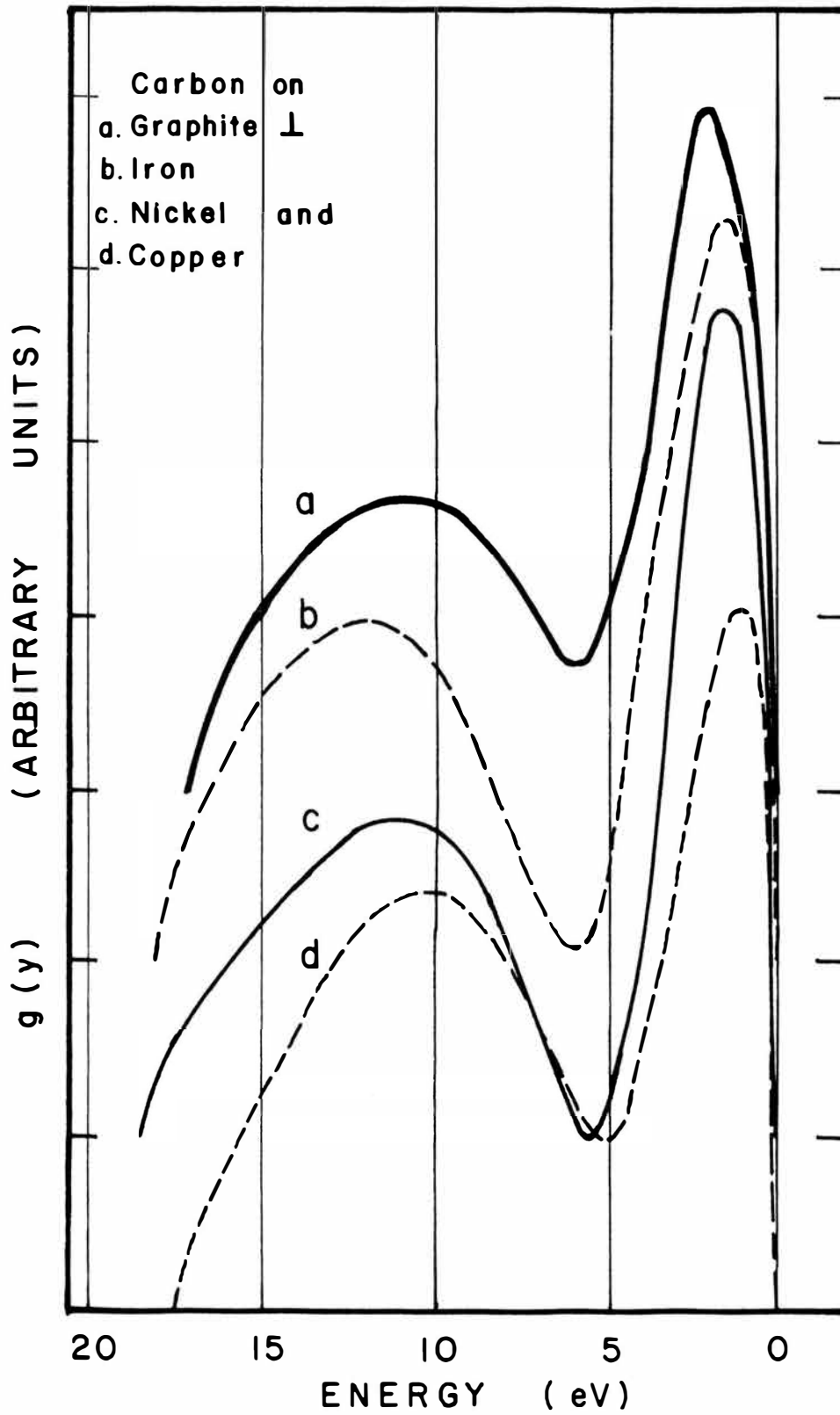


Figure 23

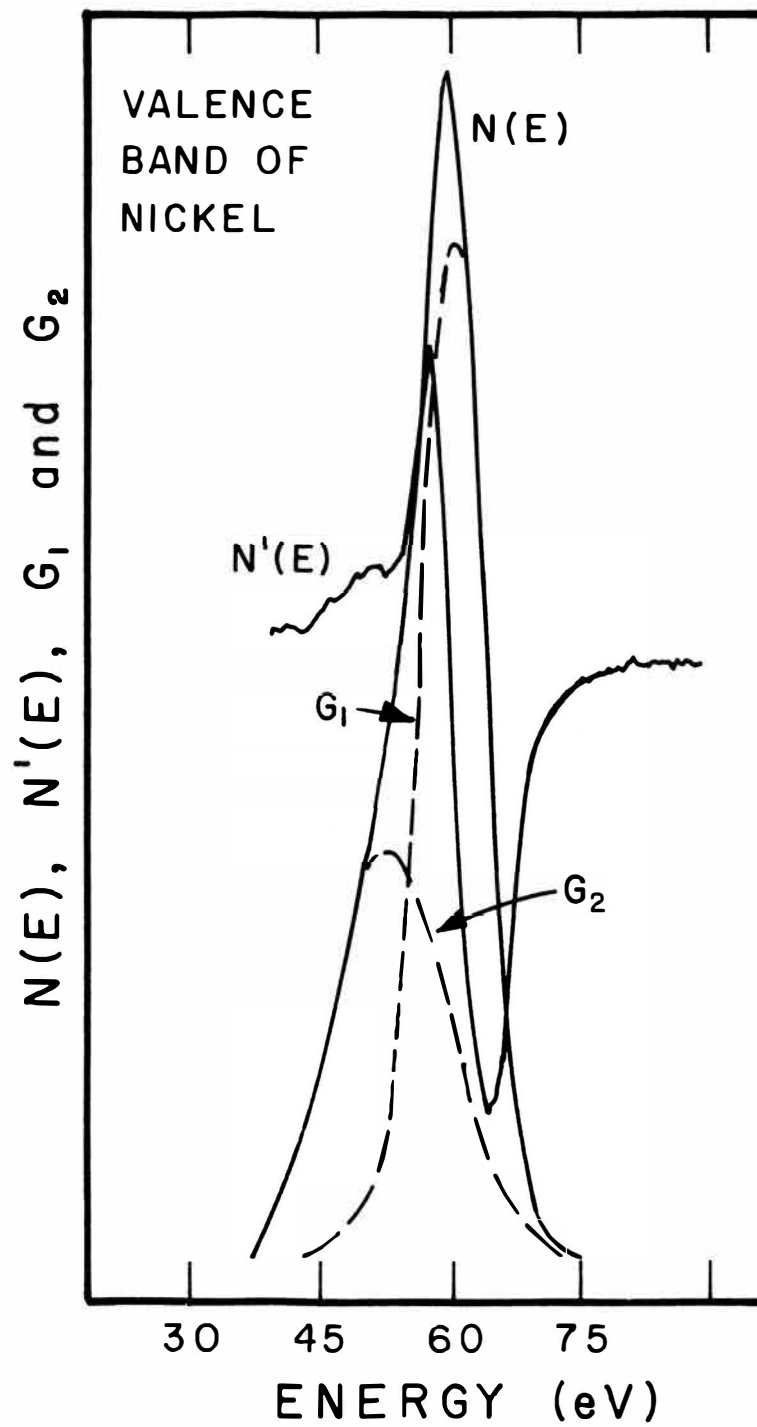


Figure 24. Auger curves $N'(E)$ and $N(E)$ and the gaussian components of the $N(E)$ curve of the valence band of nickel.

Figure 25. Valence band of nickel. The broken line shows the results obtained by Hagstrum [20] using Ion-Neutralization Spectroscopy. The full line corresponds to the transition density calculated from the Auger function $N(E)$.

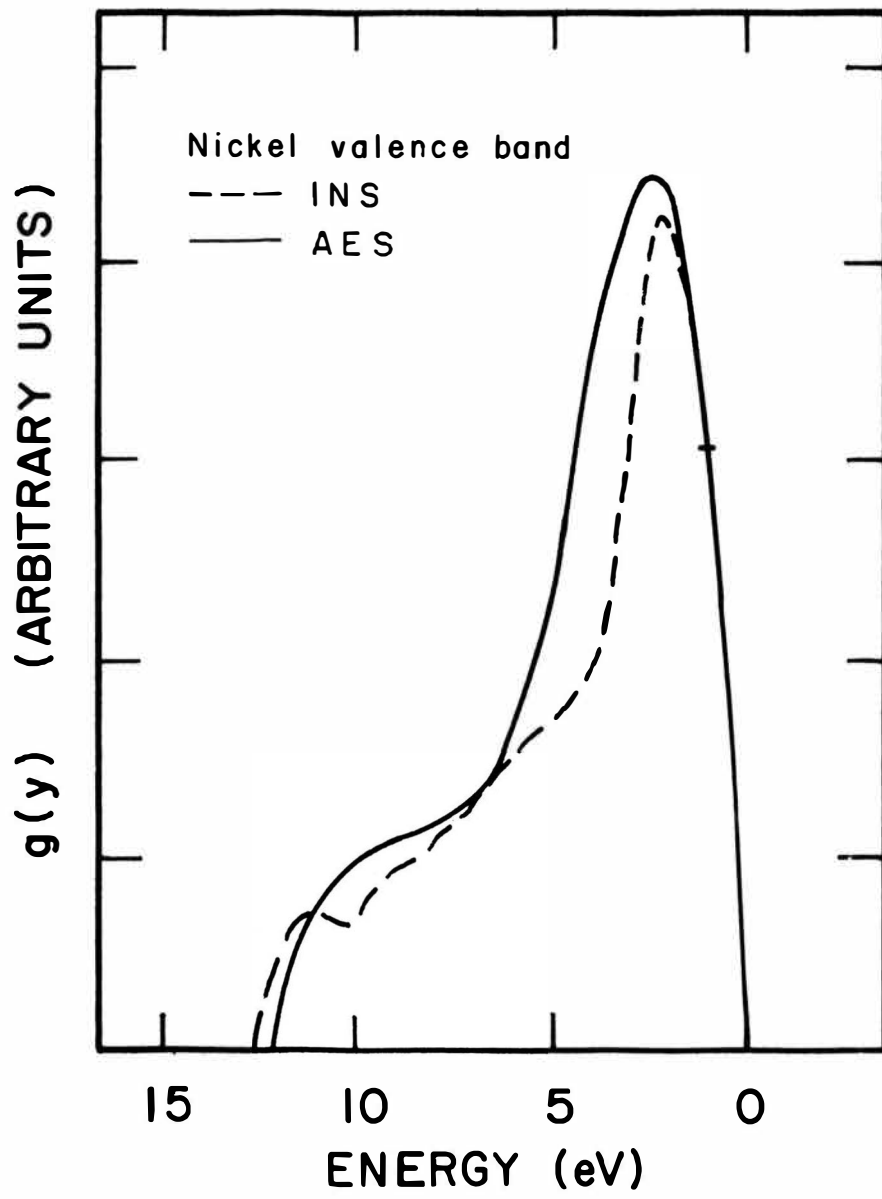


Figure 25

Figure 26. Computer simulation of instrumental broadening in the transition density function of carbon in pyrolytic graphite.

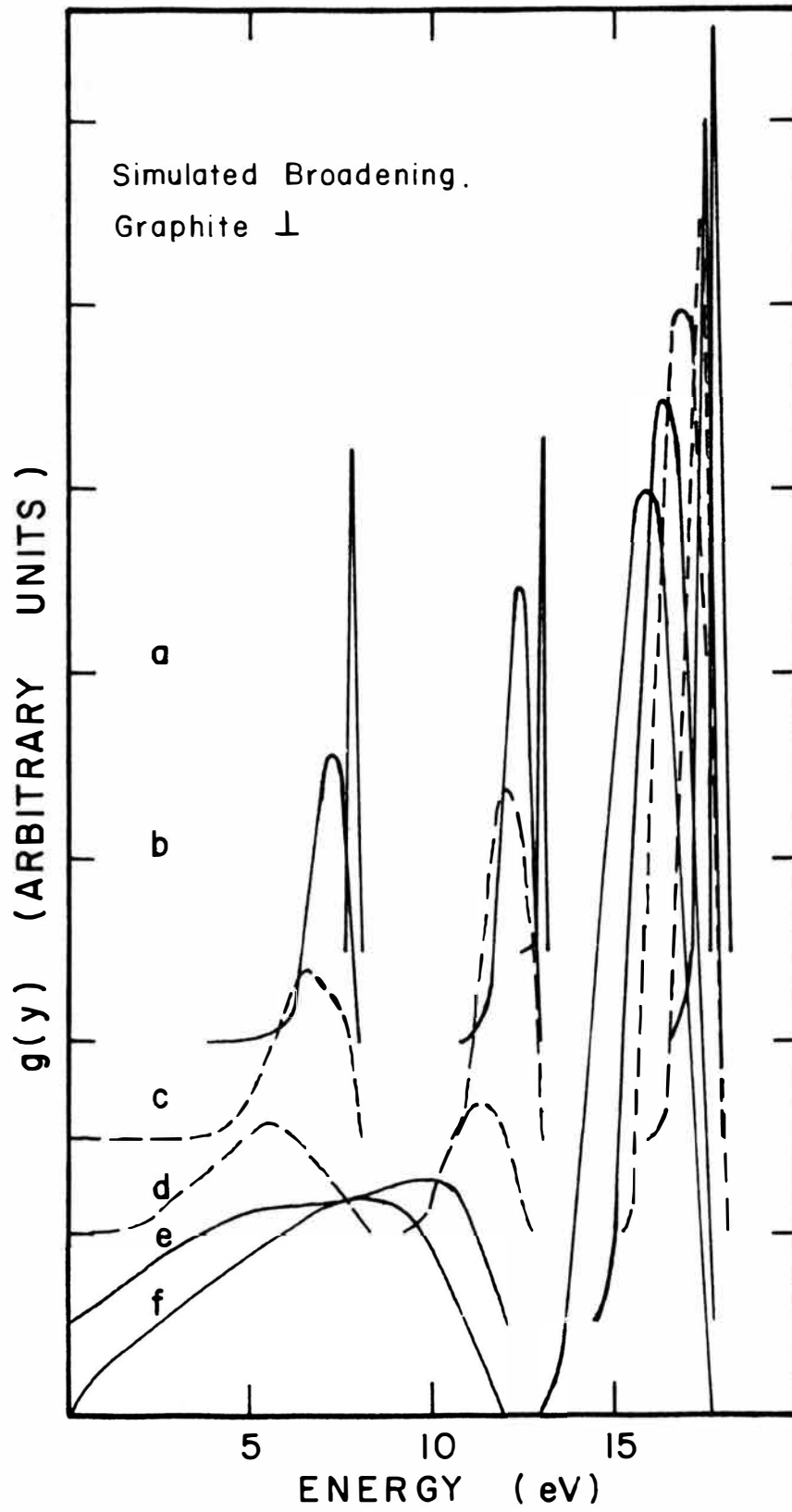


Figure 26

Figure 27. Computer simulation of instrumental broadening in the transition density function of carbon on nickel.

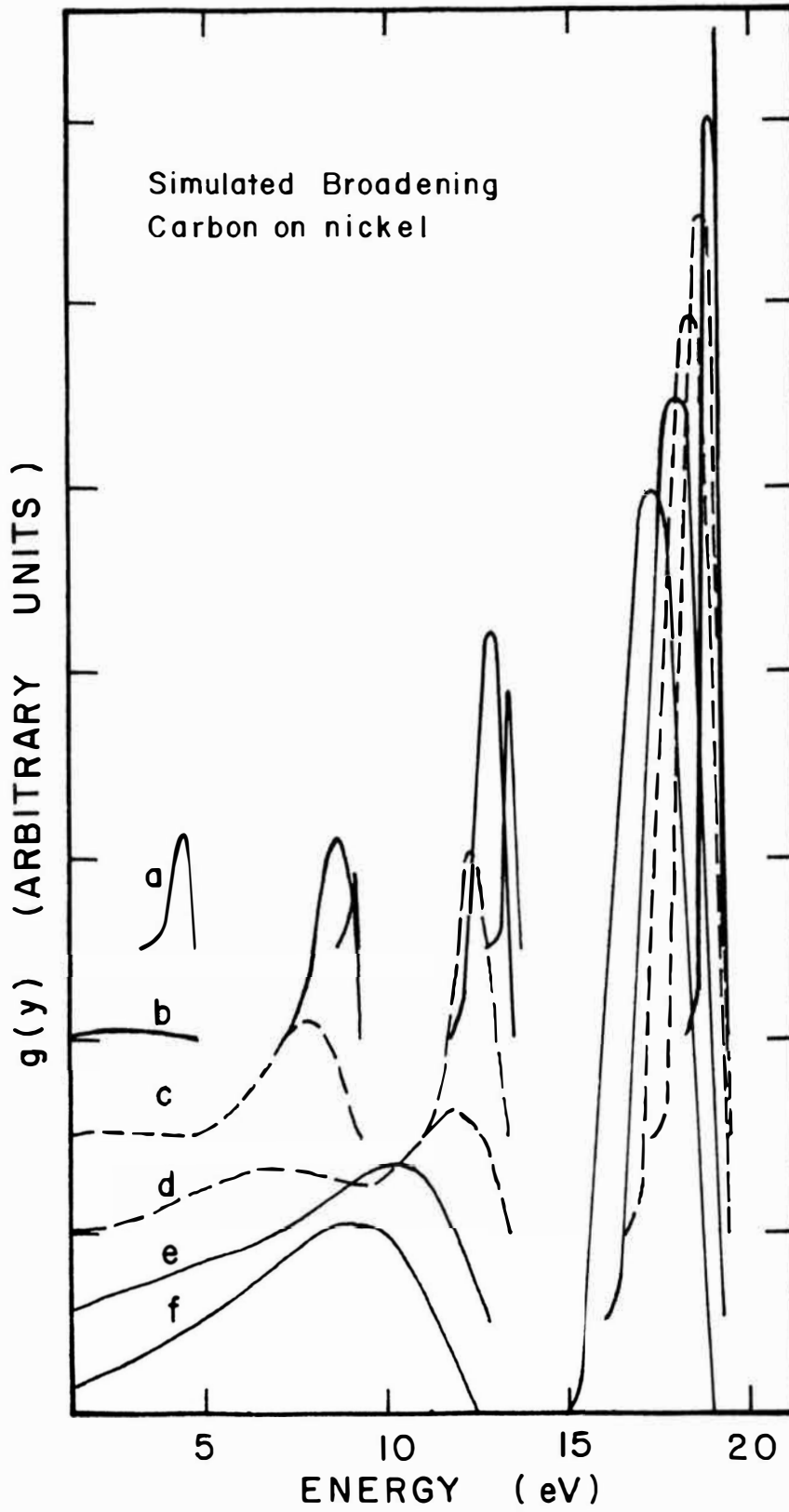


Figure 27

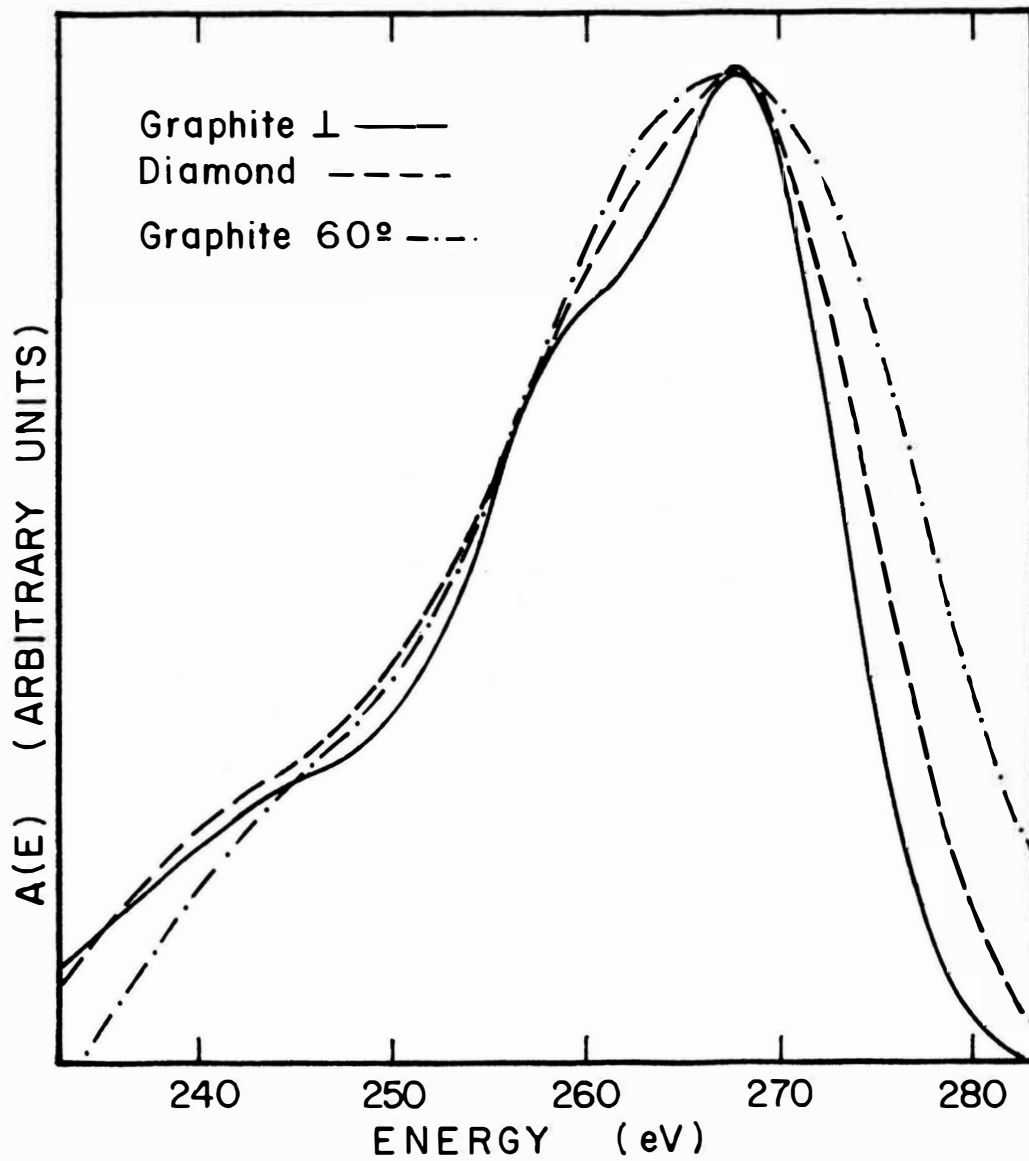


Figure 28. Unbroadened Auger curves $A(E)$ of pyrolytic graphite (0001) at 60° and 90° angles of incidence with respect to the electron beam and also of diamond (111).

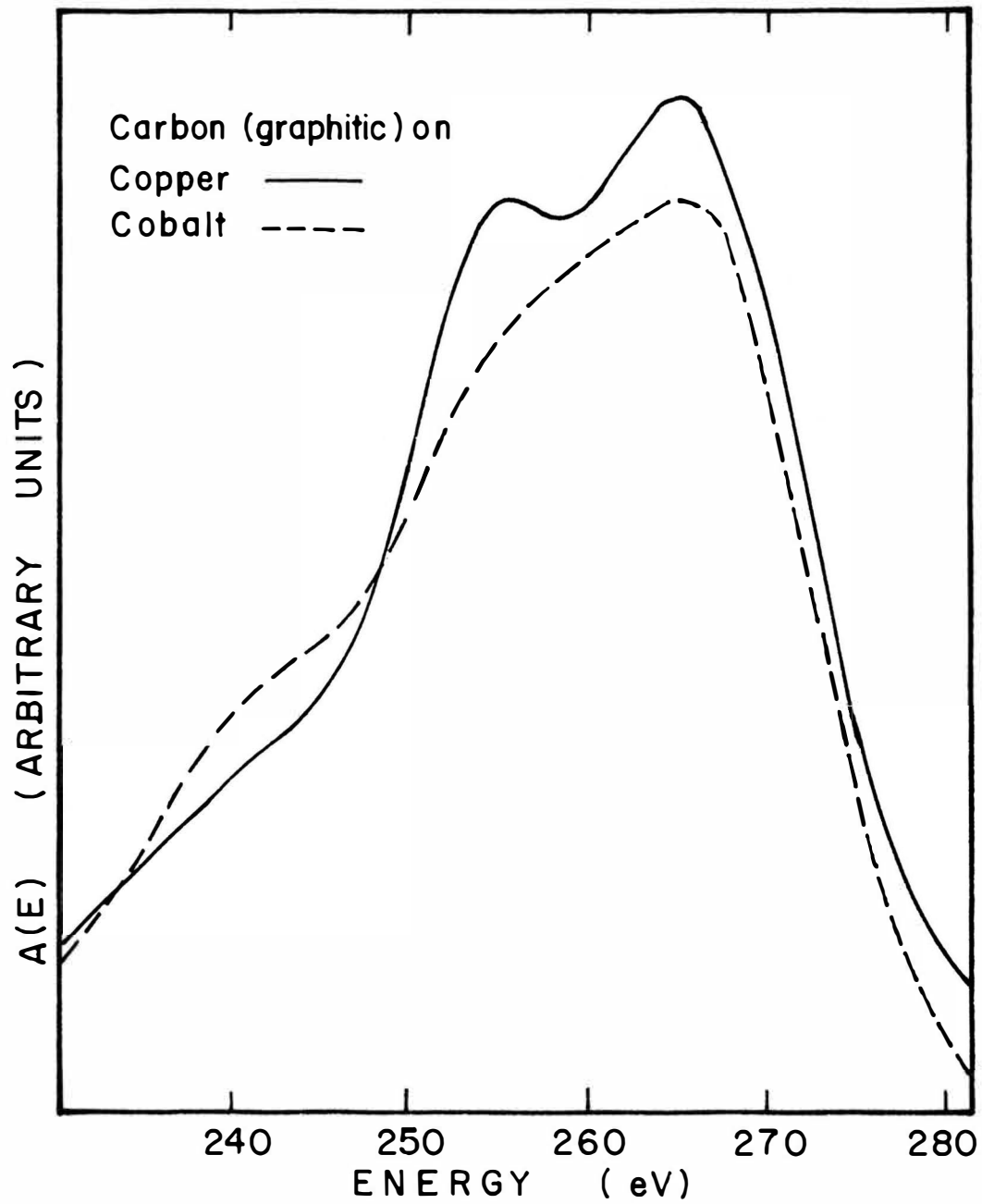


Figure 29. Unbroadened Auger curves $A(E)$ of carbon on copper and cobalt. The original $N'(E)$ curve was of the graphitic form.

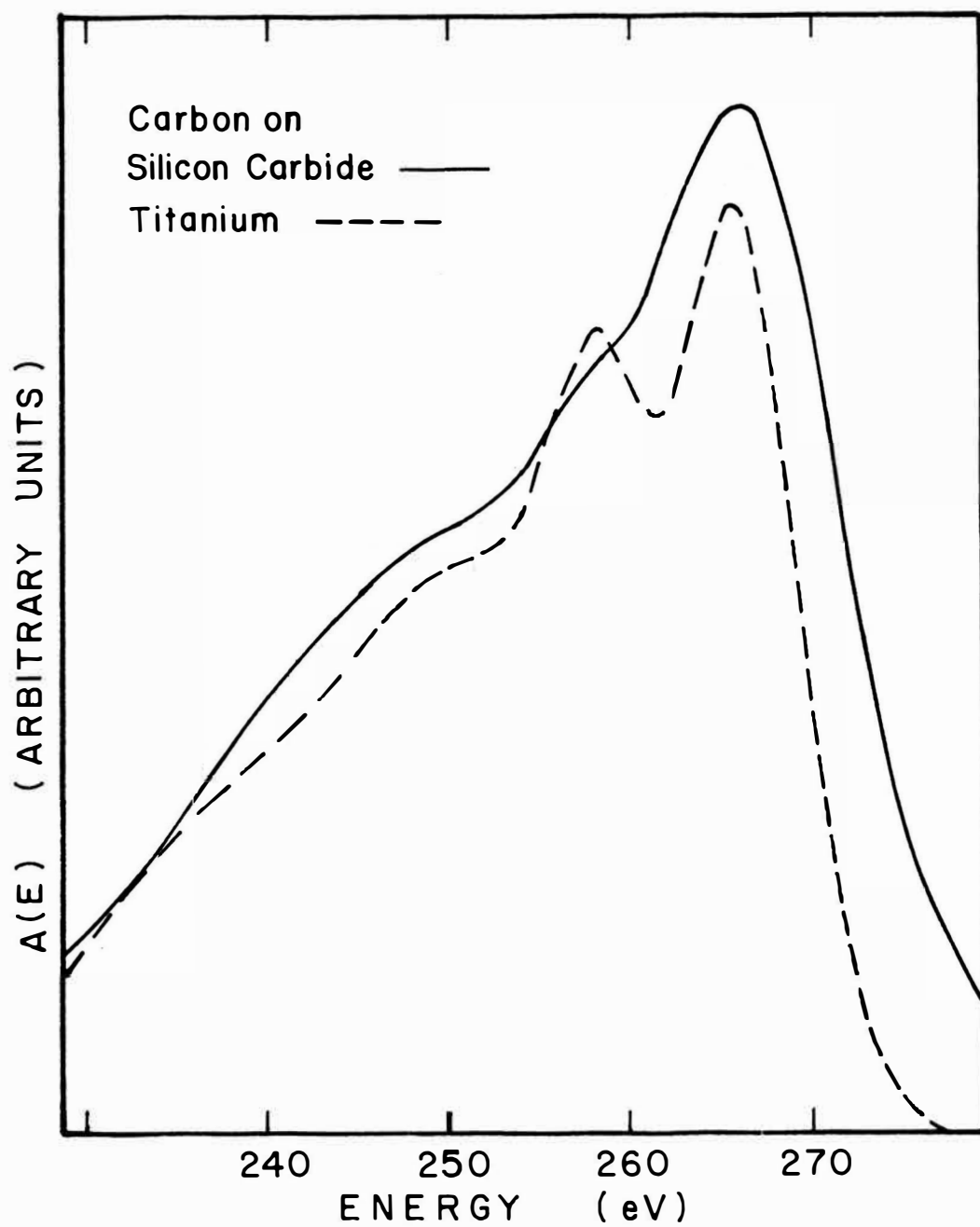


Figure 30. Unbroadened Auger curves $A(E)$ of carbon in silicon carbide and on titanium.

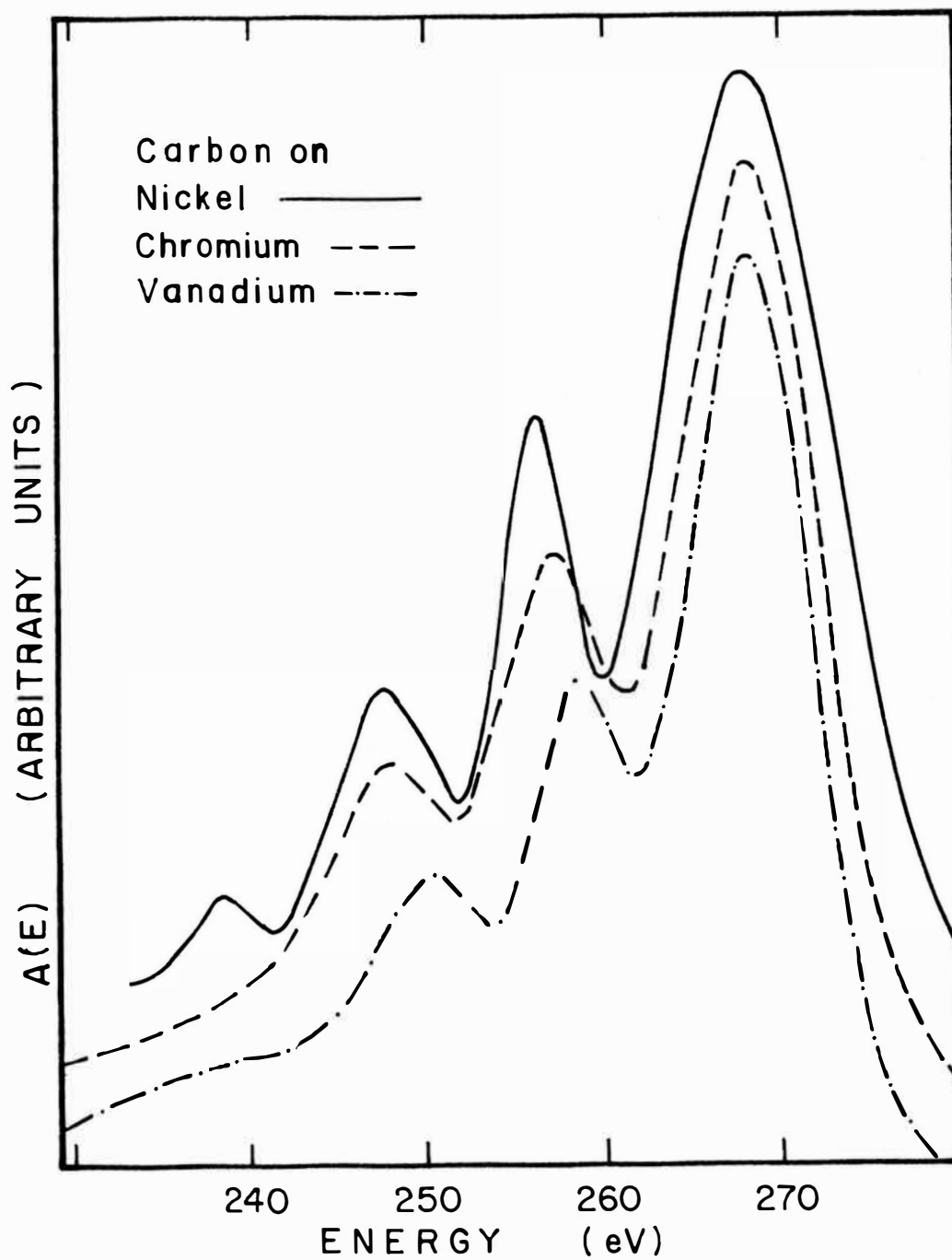


Figure 31. Unbroadened Auger curves $A(E)$ of carbon on nickel, chromium and vanadium.

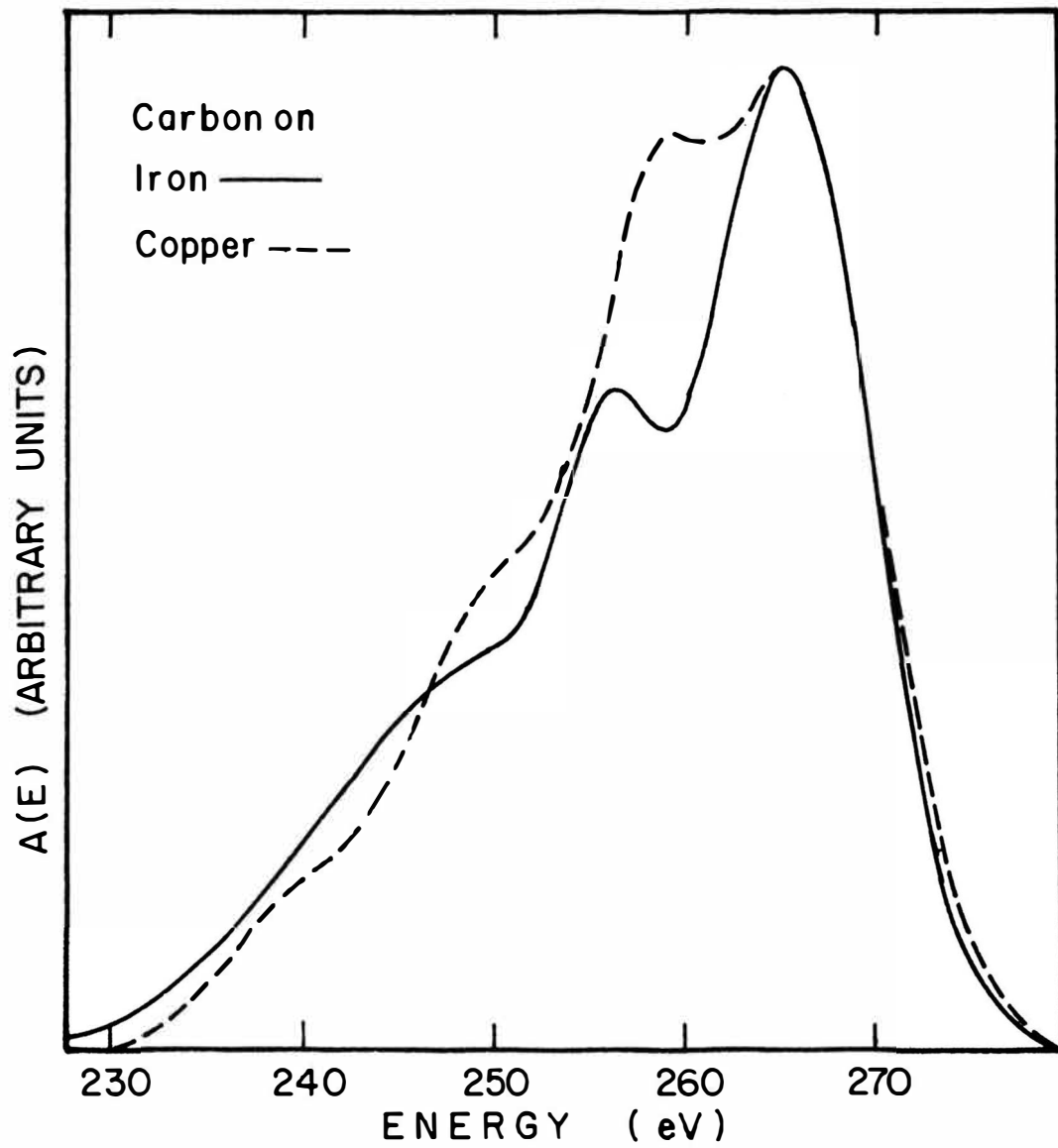


Figure 32. Unbroadened Auger curves $A(E)$ of carbon on iron and copper.

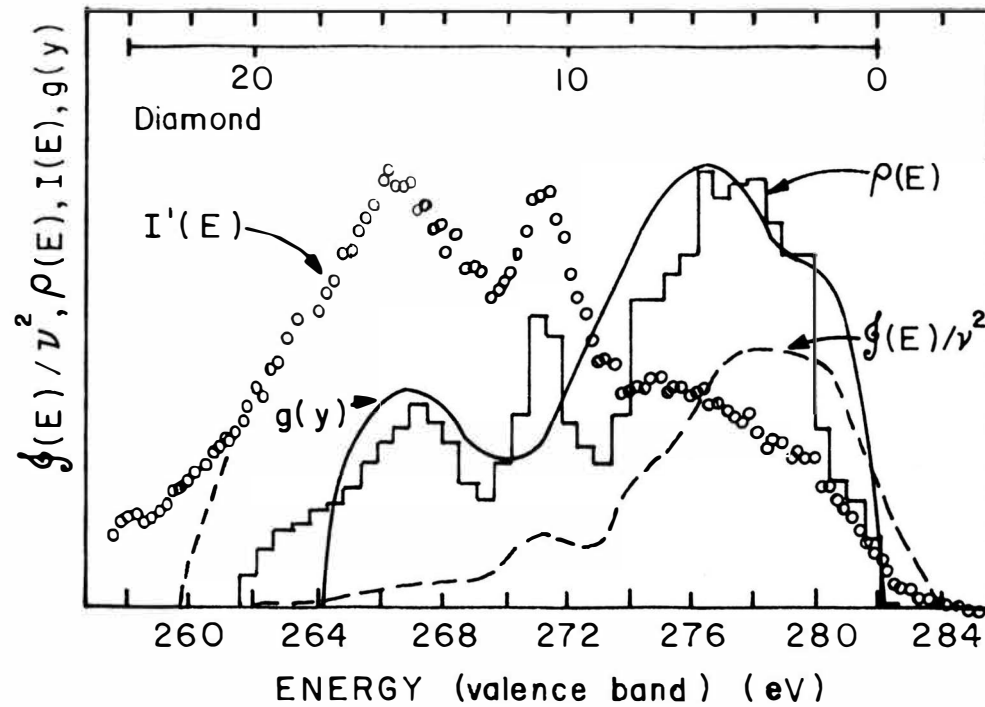


Figure 33. Comparison of the valence band of diamond as reported by McFeely et al. [24] and the results obtained from the transition density function calculated from Auger electron spectroscopy. $I'(E)$: XPS spectrum, McFeely et al. $\phi(E)/\nu^2$: K X-ray emission spectrum, Wiech and Zopf. $\rho(E)$: Density of states, Painter et al.

Figure 34. Transition density function of carbon in pyrolytic graphite (0001) at 90° angle of incidence with respect to the electron beam and in silicon carbide, calculated from the unbroadened Auger function $A(E)$.

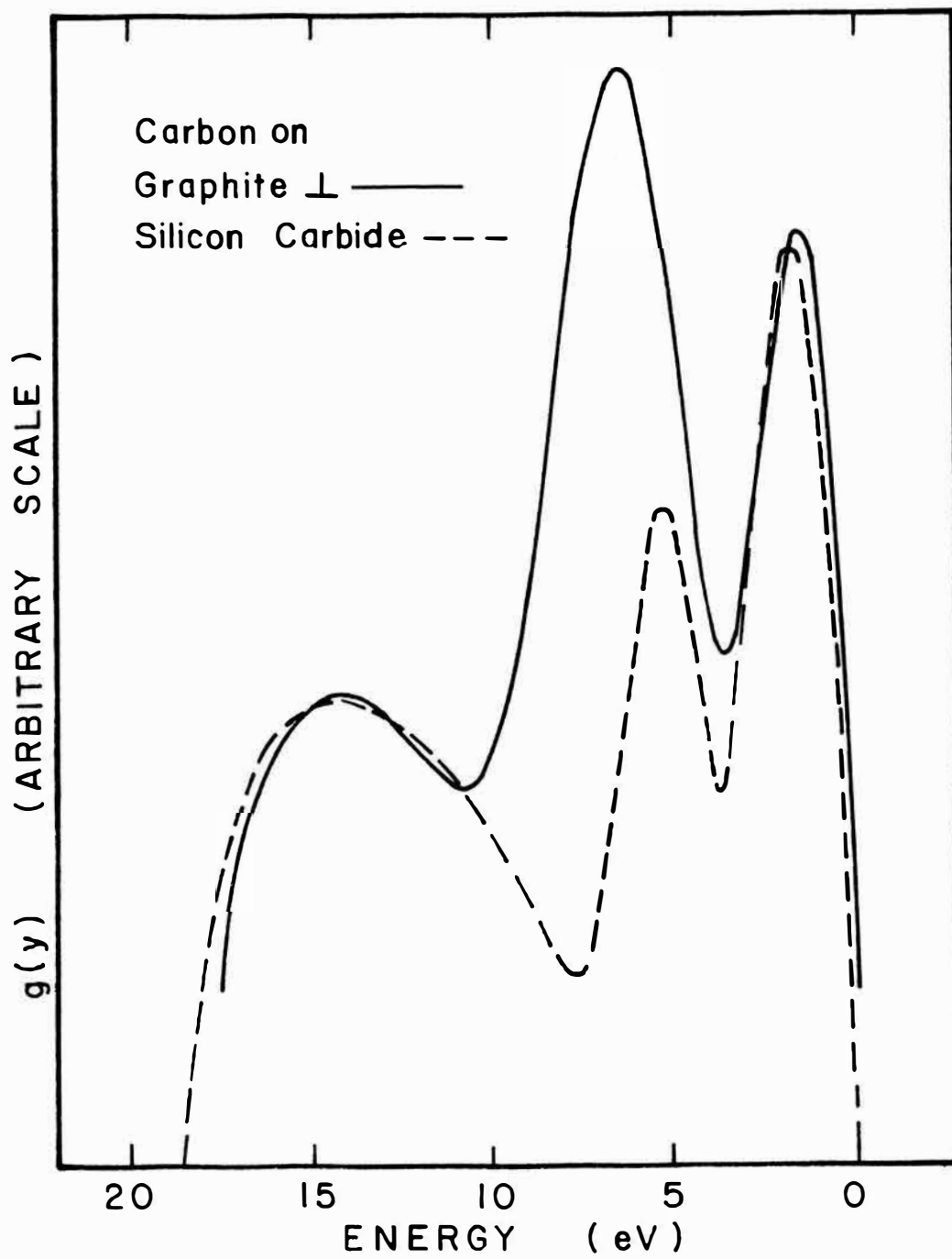


Figure 34

Figure 35. Transition density function of carbon in pyrolytic graphite (0001) at 60° angle of incidence with respect to the electron beam and in diamond (111). Also shown are the transition density functions of carbon on cobalt and copper. All these functions were calculated from the unbroadened Auger function $A(E)$.

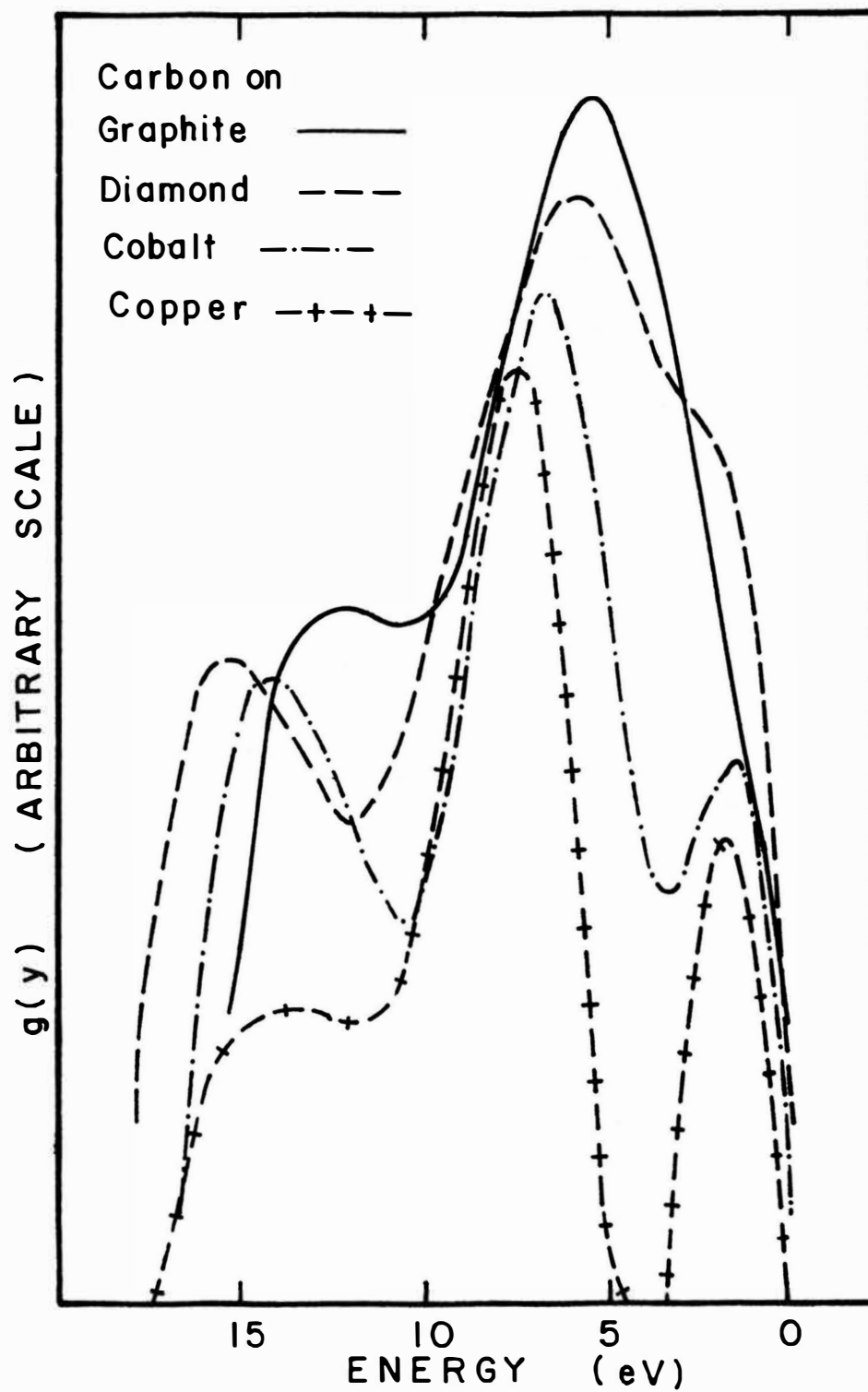


Figure 35

Figure 36. Transition density function of carbon on titanium, vanadium and chromium as calculated from the unbroadened Auger function $A(E)$.

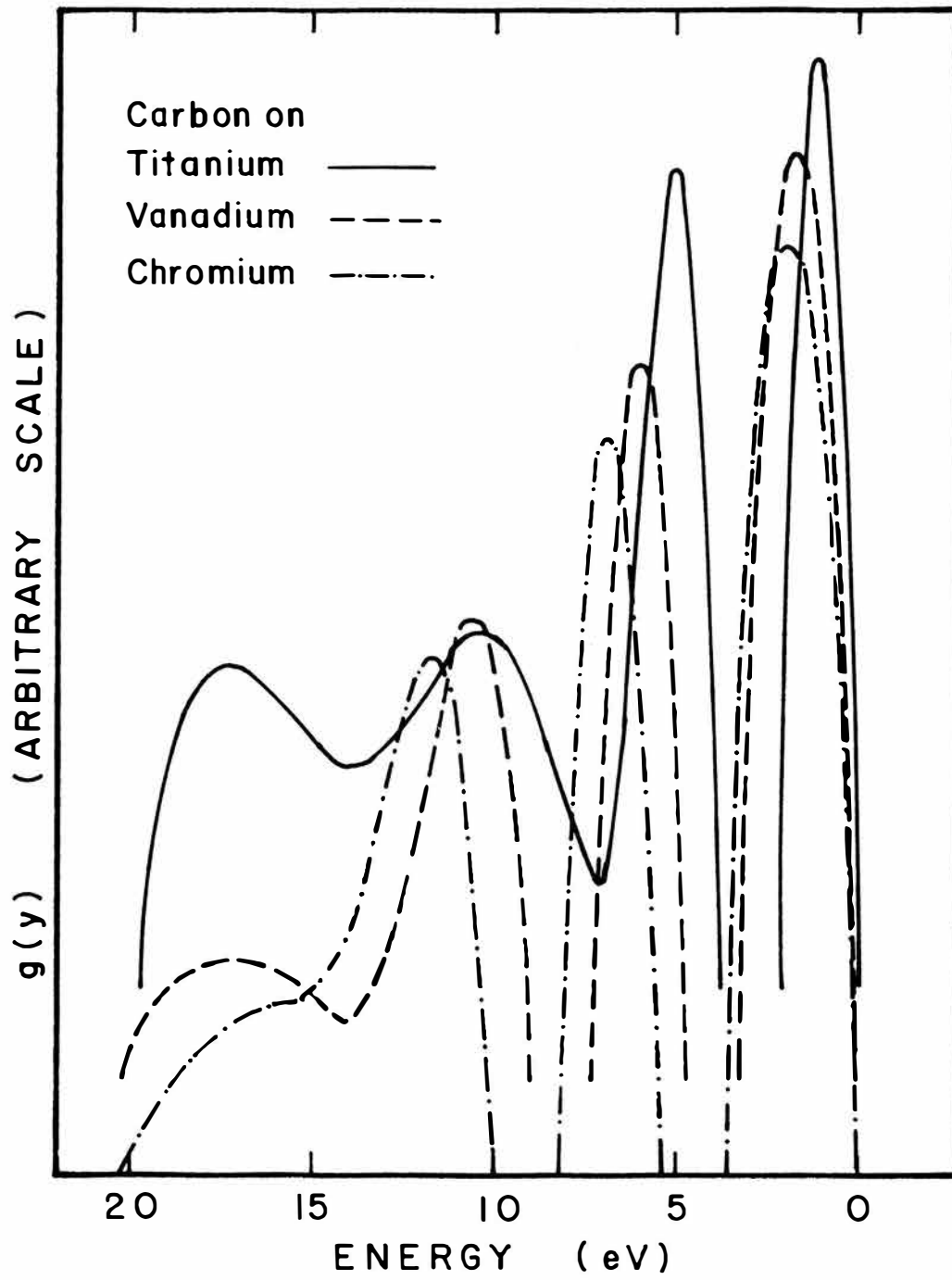


Figure 36

Figure 37. Transition density function of carbon on nickel, iron and copper as calculated from the unbroadened Auger function $A(E)$.

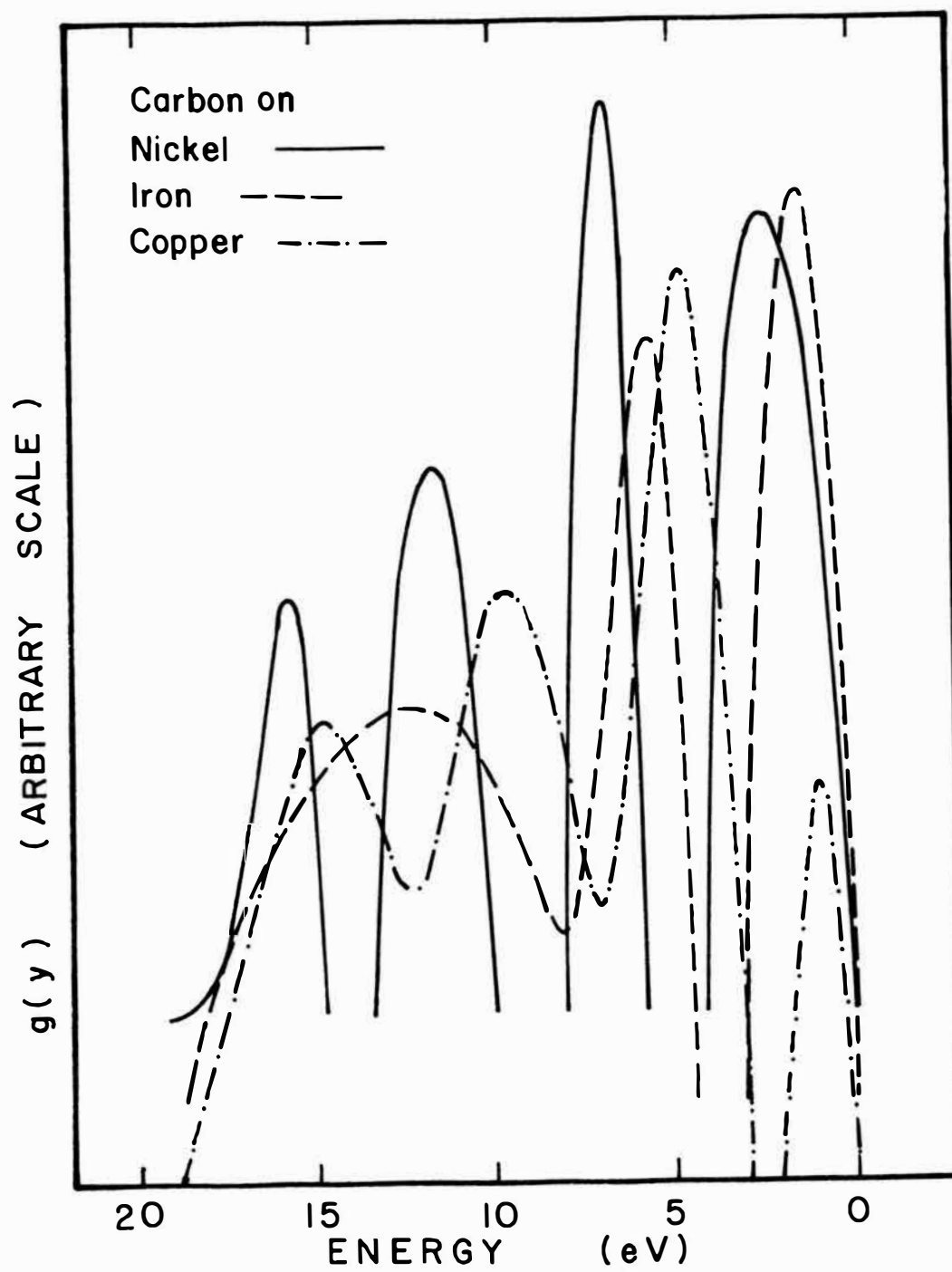


Figure 37

Figure 38. Comparison between predicted [21] and experimentally obtained KLL Auger transitions of carbon. The cases of pyrolytic graphite (0001) at 60° and 90° angles of incidence with respect to the electron beam and of diamond (111) are shown.

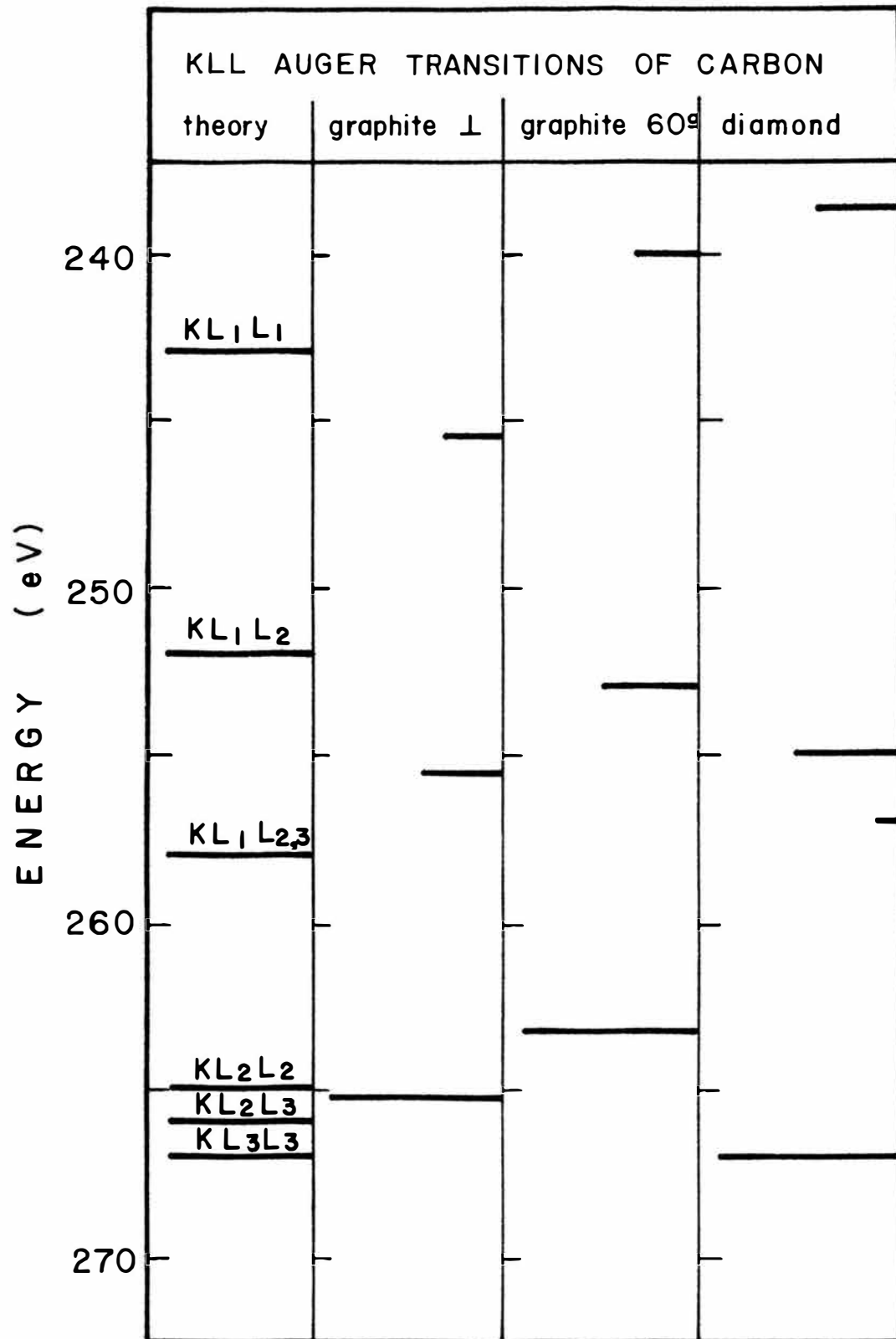


Figure 38

Figure 39. Comparison between predicted [21] and experimentally obtained KLL Auger transitions of carbon. The cases of silicon carbide, and of carbon on cobalt and copper are shown.

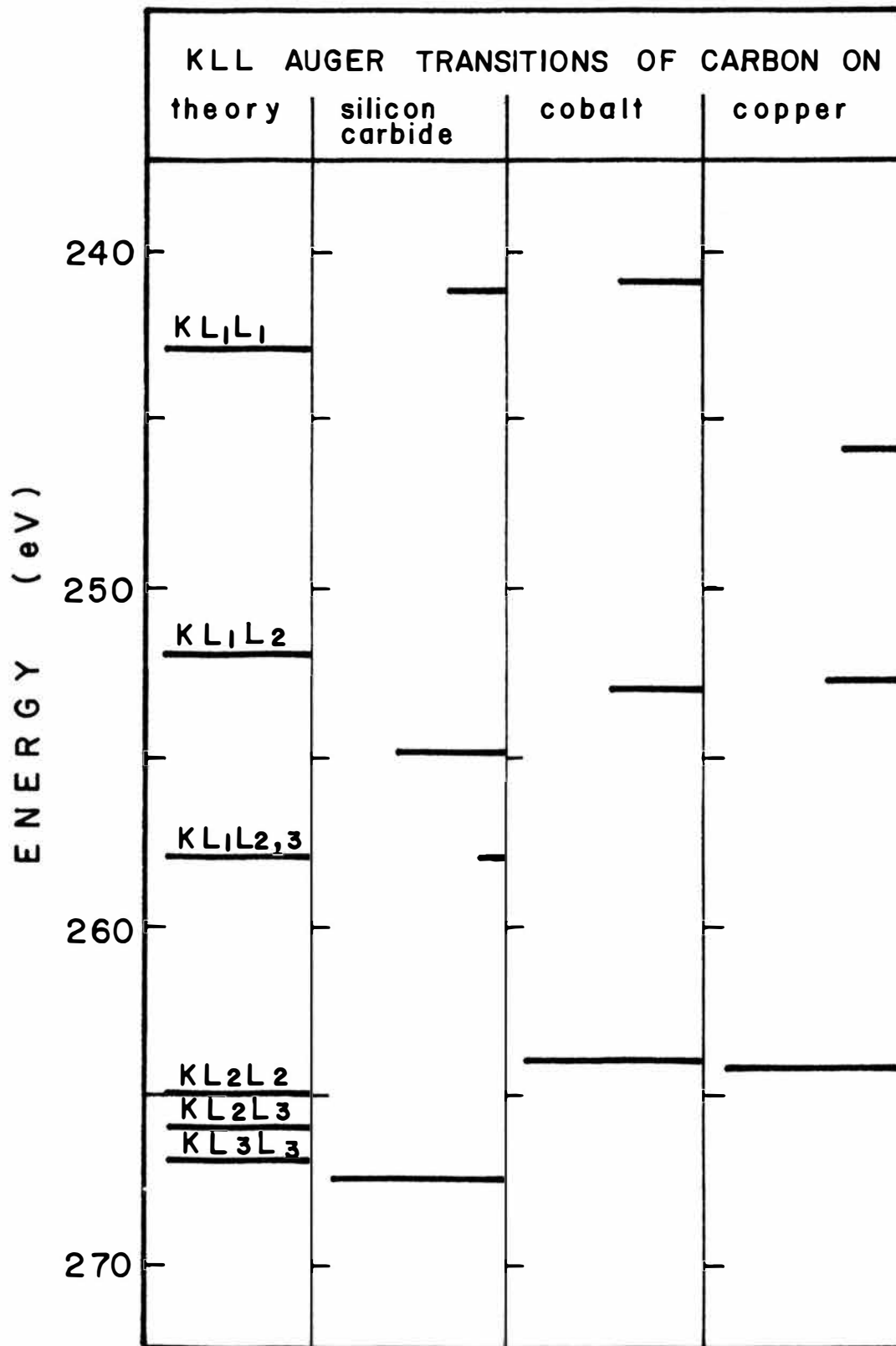


Figure 39

Figure 40. Comparison between predicted [21] and experimentally obtained KLL Auger transitions of carbon. The cases of carbon on titanium, vanadium and chromium are shown.

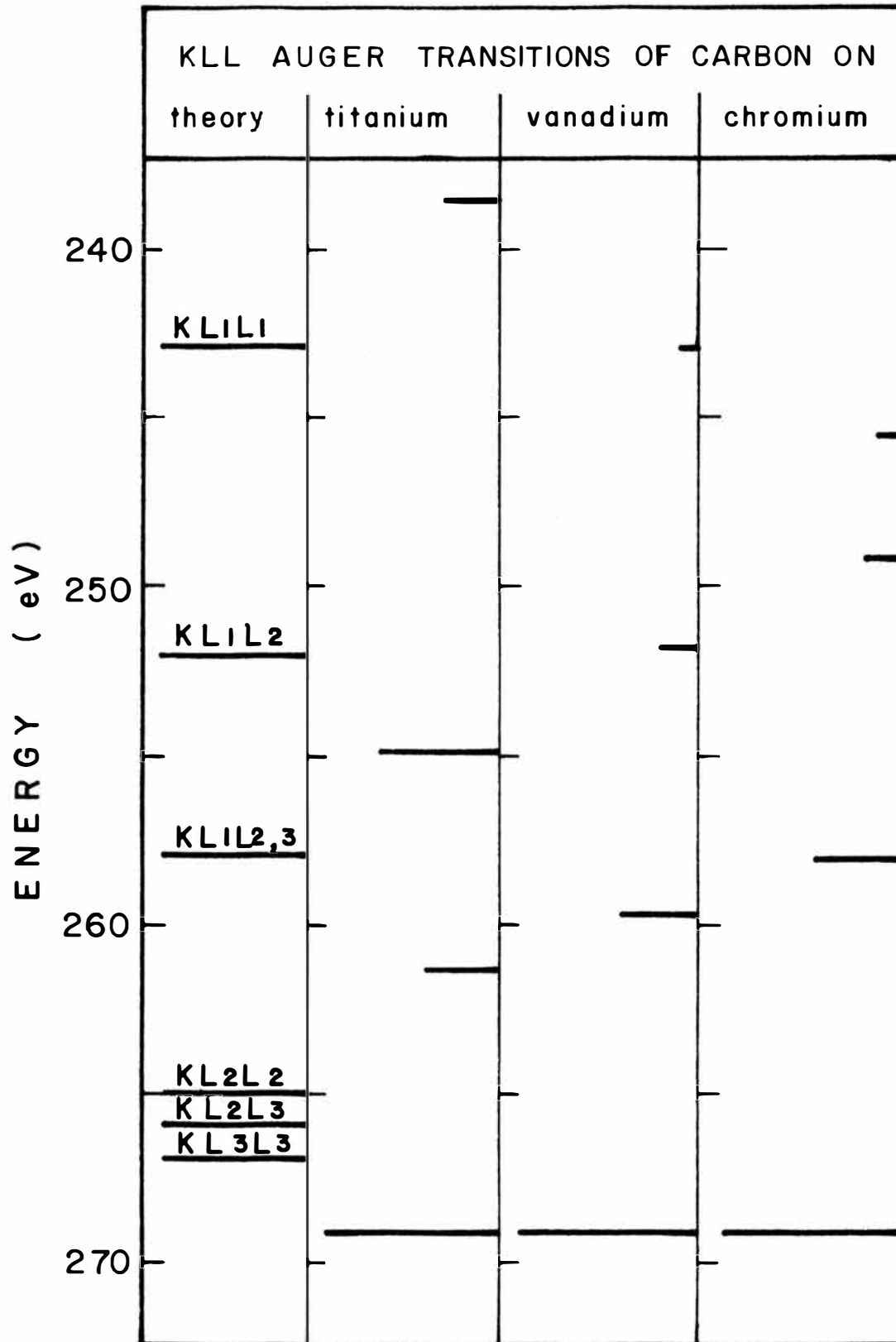


Figure 40

Figure 41. Comparison between predicted (broken lines) [21] and experimentally obtained KLL Auger transitions of carbon. The cases of carbon on iron, cobalt, nickel and copper are shown.

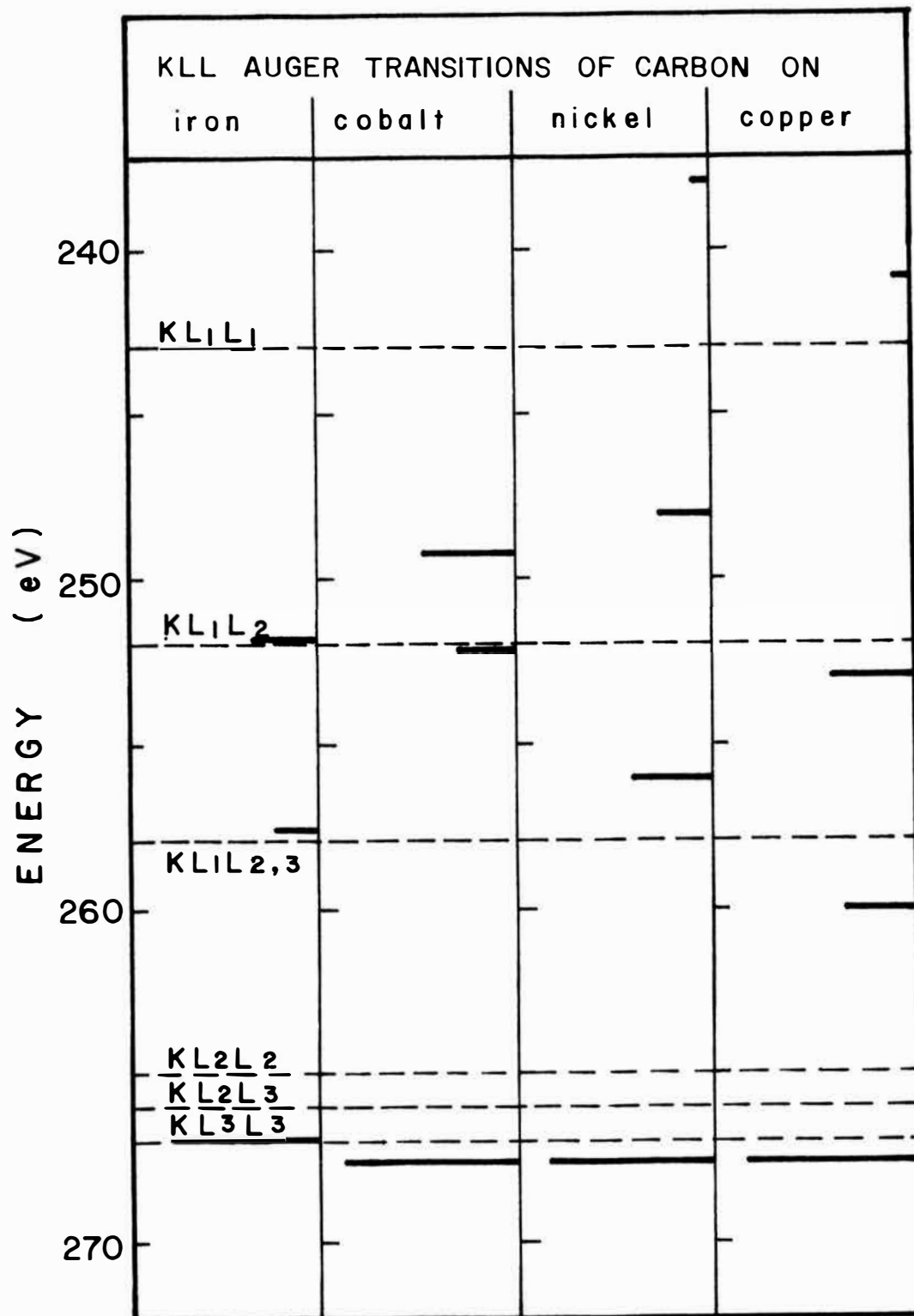


Figure 41

Figure 42. Relation between the energies of the KLL Auger transitions of carbon and the metal substrate. The broken horizontal lines correspond to the predicted values [21] for atomic carbon.

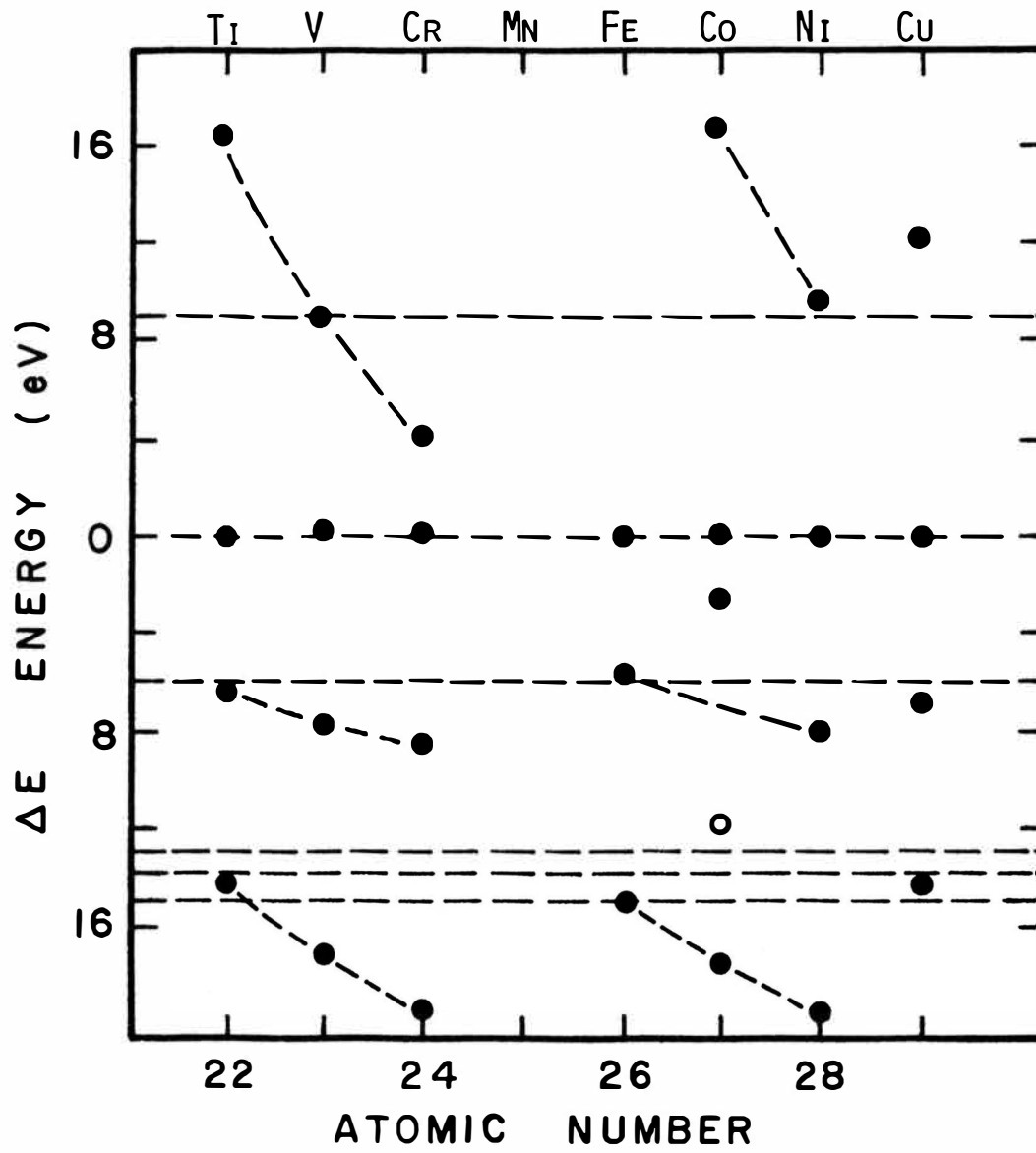


Figure 42

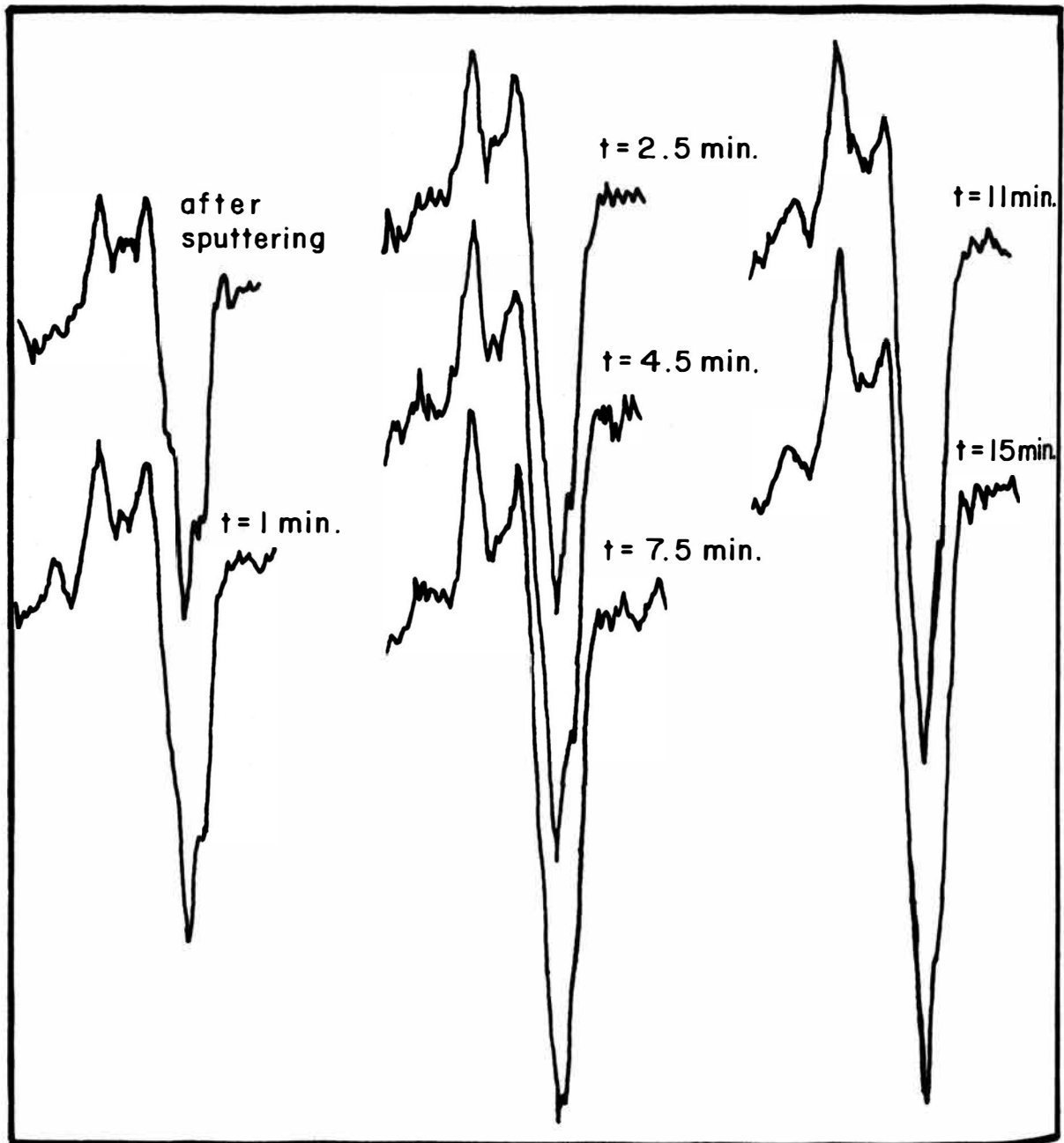


Figure 43. Change in shape of the KLL Auger spectrum of carbon on copper as the concentration of carbon at the surface increases.

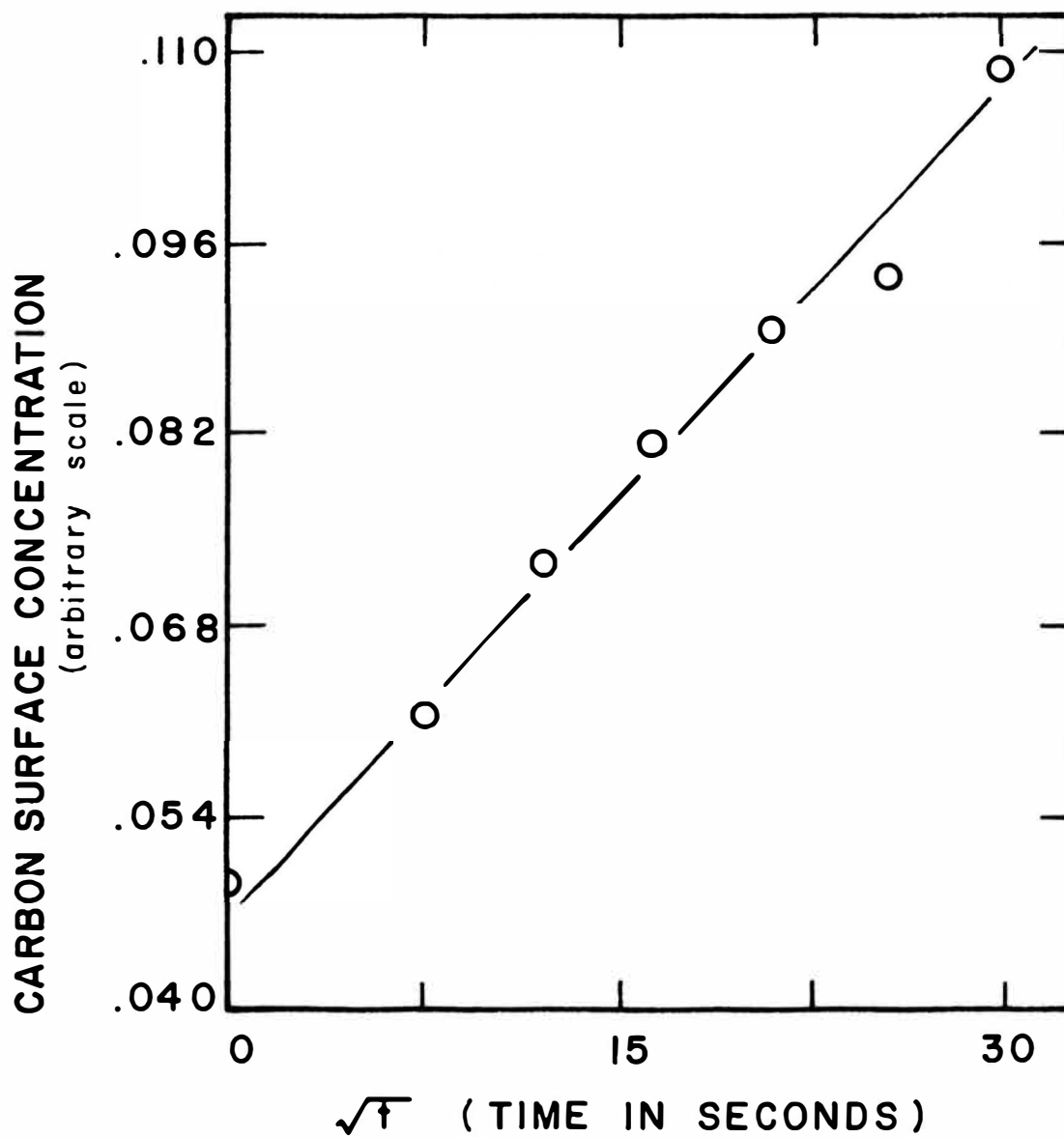


Figure 44. Carbon surface concentration dependence of \sqrt{t} .

APPENDIX I

THE TRANSITION DENSITY FUNCTION.

Assume that the Auger electron distribution function $N(E)$ is related to some function of the valence band. Let this function be $g(\zeta)$ where the variable ζ is used to define the energy below the Fermi energy level in the band and is related to the energy E of the Auger electron by:

$$E = E_2 - 2(\phi + \zeta) \quad (1)$$

where ϕ is the work function and E_2 represents the ionization energy for some inner level.

Assume also that the electrons filling the vacancy in the inner level and the Auger electrons can be originated at any energy of the band. Let Δ be one-half of the initial state separation between the two electrons involved in the transition. Then the total Auger distribution function $F(\zeta)$ can be obtained by integrating over all the Δ 's such that the initial and final states are within the band.

This distribution function will define the transition density $g(\zeta)$ since:

$$F(\zeta) = \int g(\zeta + \Delta)g(\zeta - \Delta)d\Delta \quad (2)$$

Making use of the symmetry of $F(\zeta)$ we divide this

function into two parts:

$$\begin{aligned}
 F_1(\zeta) &= \int_0^{\zeta} g(\zeta + \Delta)g(\zeta - \Delta)d\Delta & 0 < \zeta < 1/2\zeta_1 \\
 F_2(\zeta) &= \int_{\zeta-\zeta_1}^{\zeta} g(\zeta + \Delta)g(\zeta - \Delta)d\Delta & 1/2\zeta_1 < \zeta < \zeta_1
 \end{aligned}
 \tag{3}$$

$$\text{Take now: } F_1(\zeta) = \int_0^{\zeta} g(\zeta + \Delta)g(\zeta - \Delta)d\Delta$$

and let: $y = \zeta + \Delta$ and $t - y = \zeta - \Delta$, then:

$$F_1(t/2) = \int_{\zeta}^{2\zeta} g(y)g(t - y)dy . \tag{4}$$

In a similar way we can change:

$$x = \zeta - \Delta \quad \text{and} \quad t - x = \zeta + \Delta$$

and substitute in $F_1(\zeta)$ to obtain:

$$\begin{aligned}
 F_1(t/2) &= \int_{\zeta}^0 g(x)g(t - x)(-dx) \quad \text{or} \\
 F_1(t/2) &= \int_0^{\zeta} g(x)g(t - x)dx .
 \end{aligned}
 \tag{5}$$

Adding eqs.(4)and(5) we finally get:

$$2F_1(t/2) = \int_0^t g(y)g(t - y)dy . \tag{6}$$

Using the convolution theorem for Laplace transforms:

$$\begin{aligned}
 L\{2F_1(t/2)\} &= L\left\{\int_0^t g(y)g(t-y)dy\right\} \\
 &= L\{g(y)\}L\{g(y)\} \\
 &= [L\{g(y)\}]^2
 \end{aligned} \tag{7}$$

Taking the square root on both sides:

$$L\{g(y)\} = [L\{2F_1(t/2)\}]^{1/2} \tag{8}$$

and operating the inverse Laplace transform the final expression is:

$$g(y) = 2L^{-1}[f(2s)^{1/2}] \tag{9}$$

where $f(2s)$ is the Laplace transform of the Auger distribution as given by the $N(E)$ function.

To evaluate the transition density function we proceed as follows:

Let $A(t)$ be the function that represents the Auger electron distribution. Define

$$A(t) = \sum_{i=1}^n G_i(t) \tag{10}$$

where $G_i(t)$ is the i th gaussian component of the Auger electron distribution.

Let $H(t) = mt + b$ be the straight line approximation of $A(t)$ in a very small interval Δt . Then:

$$L\{H(t)\} = f(s) = m/s^2 + b/s \quad \text{and} \quad (11)$$

$$f(2s) = b(s + \alpha)/2s^2 \quad \text{where} \quad (12)$$

$$\alpha = m/2b . \quad (13)$$

Evaluating now,

$$[f(2s)]^{1/2} = (b/2)^{1/2} \{1/(s + \alpha)^{1/2} + \alpha/[s(s + \alpha)^{1/2}]\}. \quad (14)$$

Taking the inverse Laplace transform of eq. (14) the transition density function $g(t)$ will be given by:

$$g(t) = (b/2)^{1/2} \left\{ \frac{t^{-1/2} e^{-\alpha t}}{\Gamma(1/2)} + \sqrt{\alpha} \operatorname{erf}[(\alpha t)^{1/2}] \right\} \quad (15)$$

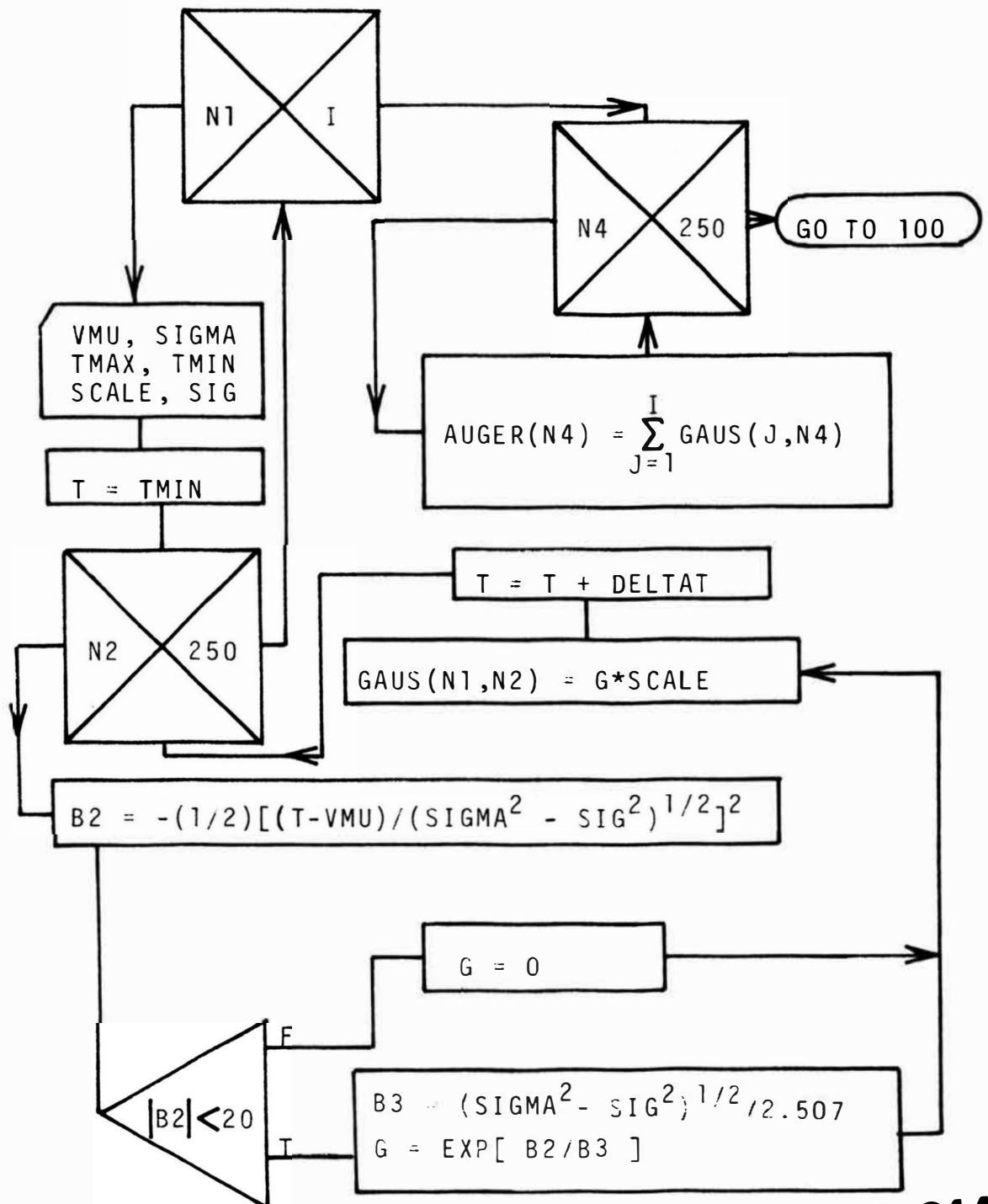
The parameter $\alpha = m/2b$ can be evaluated from eq. (10) since:

$$m = [A(t + \Delta t) - A(t)]/(\Delta t) \quad \text{and} \quad (16)$$

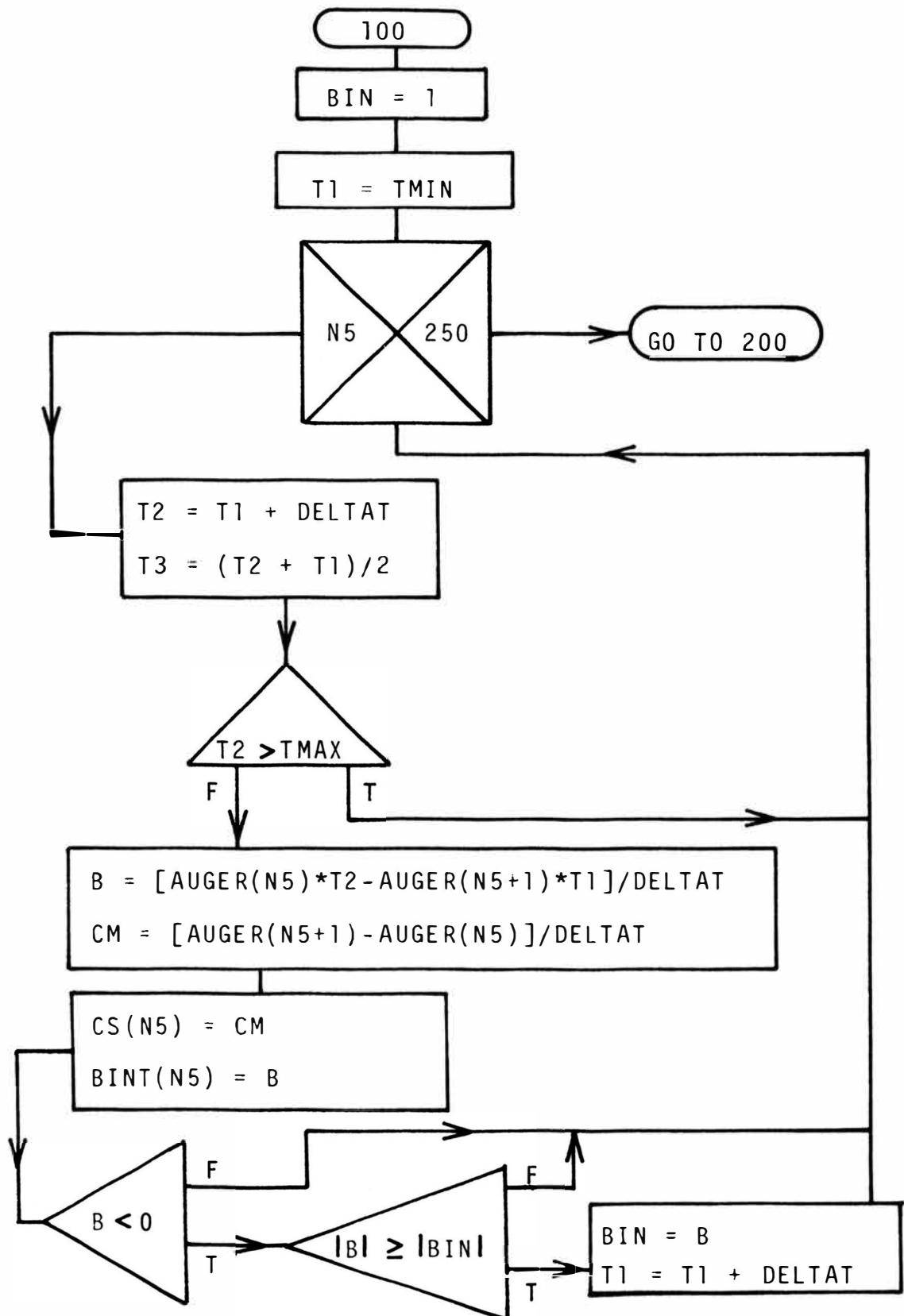
$$b = [A(t)(t + \Delta t) - A(t + \Delta t)(t)]/(\Delta t) . \quad (17)$$

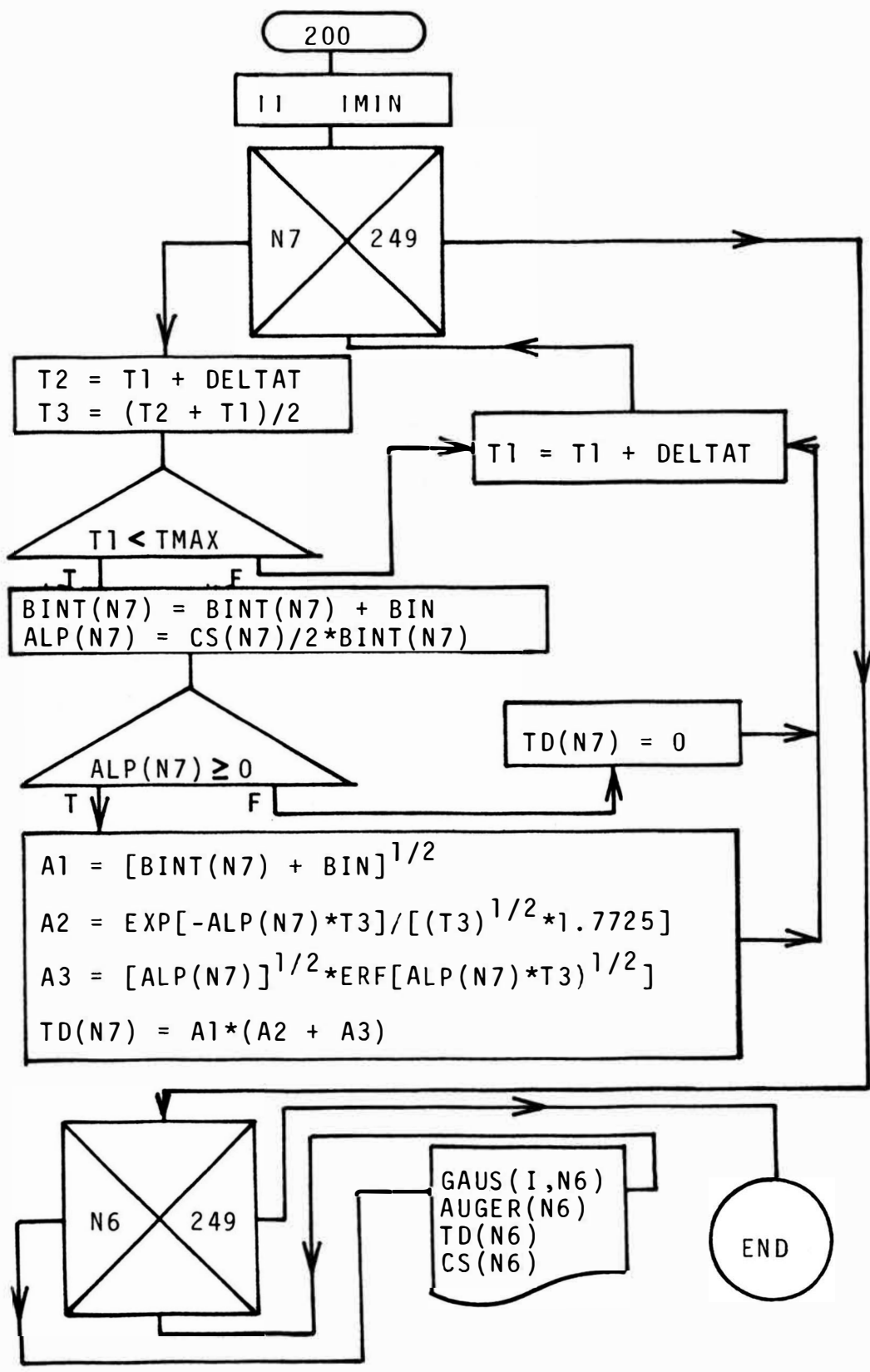
APPENDIX II

FLOW DIAGRAM FOR THE EVALUATION OF THE TRANSITION DENSITY FUNCTION.



248244





VARIABLES OF THE PROGRAM.

- GAUS(I,J). Evaluates the gaussian components of the Auger function $N(E)$ at each point of the energy range defined by the variables TMAX and TMIN.
- TD(J). Evaluates the transition density function at each point of the selected energy range.
- AUGER(J). Evaluates the Auger function $N(E)$ at each point of the energy range between TMAX and TMIN.
- BINT(J). Stores the value calculated for the intercept of the straight line that approximates the Auger function $N(E)$ at every interval defined by E and $E + \Delta E$.
- CS(J). Stores the value of the slope in the straight line approximation of the function $N(E)$ at every interval given by E and $E + \Delta E$.
- ALP(J). Stores the value of the variable α defined in Appendix I as: $\alpha = b/2m$. This variable is also calculated at every interval given by E and $E + \Delta E$.
- VMU. Stores the values of the means of the gaussian components of the function $N(E)$.
- SIGMA. Stores the values of the standard deviation of the gaussian components of $N(E)$.
- TMAX. High energy cut-off on the evaluation of the transition density function.

- TMIN. Low energy cut-off on the evaluation of the transition density function.
- SIG. Stores the value of the standard deviation of the gaussian component of the elastic peak. This variable is very important because it defines the instrumental broadening of $N(E)$.
- SCALE. Scale factor that relates the gaussian components of $N(E)$ to each other according to their maxima.
- BIN. Dummy variable used to avoid the problem of zero intercept on the straight line approximation of $N(E)$.
- DELTAT. Magnitude of the small intervals in which the energy range has been divided.
- I. This variable counts the number of gaussian components of $N(E)$.

Part II

Application of Auger Electron Spectroscopy to the Bulk-
to-Surface Precipitation and Surface Diffusion of Carbon
on Polycrystalline Nickel.

Manuscript to be submitted to Surface Science.

ABSTRACT

The time evolution of the KLL Auger spectrum of carbon as a function of temperature is used to derive the kinetics of the surface diffusion and bulk-to-surface precipitation of carbon on polycrystalline nickel.

The results show that the activation energy for the surface diffusion of carbon atoms on polycrystalline nickel is 6.9 ± 0.6 kcal/mole, and the activation energy for bulk-to-surface precipitation is 9.4 ± 0.6 kcal/mole. The temperature dependence of the surface diffusion coefficient can be represented, over the experimental temperature range, by:

$$\ln(D) = 10.27 - 3568/T.$$

INTRODUCTION

In the study of diffusion in solids we can distinguish between bulk diffusion, bulk-to-surface precipitation and surface diffusion. Different techniques have been applied to evaluate the diffusion coefficient and the activation energy for these processes.

Internal-friction measurements and radioactive tracers techniques are better suited for bulk diffusion processes. In the case of carbon, Klopp and Barth[1] refer to the work done by Powers and Doyle[2] which used internal-friction measurements to determine the diffusion equation for carbon in columbium. Using this same technique Ke[3] and Wert[4] obtained results for the diffusion of carbon in tantalum. More recently Massaro and Petersen[5] using a radioactive tracer technique determined the diffusion of carbon-14 through polycrystalline nickel.

For bulk-to-surface precipitation and surface diffusion a surface analysis technique is required. Auger Electron Spectroscopy (AES) has proven to be a suitable technique for surface characterization and its use for segregation and diffusion studies has become common practice. Bishop and Riviere[6] applied AES to investigate the segregation of boron in boron-doped iron. Wildman, Howard and Ho[7] studied the case of grain boundary diffusion of copper in polycrystalline aluminum films by combining AES and ion-sputtering techniques.

This technique has also been used in the case that concerns us. Sickafus[8] used this technique to study the kinetics of carbon and sulfur removal in a nickel surface at temperatures above 450°C. Combining AES with Low Energy Electron Diffraction (LEED) and assuming a Langmuir model for segregation to non-interacting sites, Isett and Blakely determined the binding energies of carbon to Ni(100)[9] by monitoring the decrease in the peak-to-peak amplitude of the Auger signal of carbon in the temperature range between 315 and 727°C. They also obtained the energy of segregation of carbon to a stepped nickel surface between 372 and 780°C[10]. Shelton, Patil and Blakely[11] also used AES to look at the equilibrium segregation of carbon to a nickel[111] surface containing about 0.3 at% carbon in solution and in a temperature range above 500°C.

The present work concerns the diffusion kinetics of carbon in polycrystalline nickel. Previous workers have been concerned about equilibrium segregation of carbon in different nickel substrates.

Segregation, according to their definition, occurs "under conditions which correspond to a one-phase field on the phase diagram"[11]. On the other hand our work deals rather with a process in which a second phase is formed. This process is called precipitation.

This work differs from the previously mentioned procedures in that the bulk carbon concentration involved is of the order of 0.01 at% and in the use of AES to monitor

the increase of material at the surface as a function of time at constant temperature.

This procedure for determining the precipitation and diffusion of carbon at the surface of nickel was adopted for two reasons. First, the sputtering yields of nickel and carbon are radically different[12]. This difference will cause the nickel to be sputtered away at a faster rate than carbon. Therefore the carbon concentration as measured by AES will not correspond to carbon concentration at the depth the ion beam has penetrated the nickel. Second, it has been shown previously[13] that changes in carbon concentration produce changes in the carbon KLL Auger spectrum. By monitoring the change in shape of the Auger carbon signal at the sample surface we were able to determine the diffusion and precipitation kinetics of the process.

EXPERIMENTAL PROCEDURE

The instrument used was a Scanning Auger Spectrometer (Physical Electronics) that is described elsewhere[14]. Therefore we will mention only those features of the instrument which were significantly involved in the conduct of the experiment.

The primary beam current was 0.3 μA as measured by a Faraday cup. The beam energy was 2 keV. The modulation voltage was 3 eV. The electron probe was 5 μm diameter.

The instrument is capable of performing

two-dimensional Auger analysis over an area of the sample. This is done by recording on photographic film the intensity of the minimum of a characteristic Auger spectrum as the beam is rastered over an area of the sample. This technique then allows the recording of the spatial distribution of elements on the surface analyzed.

The instrument also has a multiplexing unit which was used to monitor the peak-to-peak amplitude of the Auger signals of carbon (272 eV) and nickel (65 eV). If other elements were present, their concentration was below the detection limit of the instrument (about 0.1% of a monolayer).

The sample used was a commercial high purity (99.99 at%) nickel ribbon, 0.05 X 0.025 X 1.5 cm. This sample was not treated to increase the carbon concentration. The ribbon was spot welded to a pair of molybdenum electrodes. These electrodes were attached to heavy gauge copper wire for the conduction of the heating current. The sample was resistance heated. No effect of the heating current was detected in the position or in the shape of the Auger spectra.

After the sample was positioned, it was annealed in ultra-high vacuum for 30 minutes at 1000°C. In this manner grain sizes of approximately 0.3 to 0.5 mm diameter were obtained. The results presented in this work were obtained after this first annealing of the sample. Data taken after a second annealing for another 30 minutes at 1000°C and in a different spot of the sample showed no discrepancy with

the data previously obtained.

Special attention was paid to the effect of sample contamination from residual gases. It was observed that at pressures below 10^{-6} Pa the effect of the residual atmosphere was not significant for the time required to take the data. All data were recorded at pressures of the order of 10^{-7} Pa or lower.

The temperature of the sample was monitored with a chromel-alumel thermocouple spot-welded to the nickel ribbon. The temperature was held constant to $\pm 1^\circ\text{C}$ during the recording of the data. The temperature readings were accurate to within $\pm 2^\circ\text{C}$. The distance from area probed by the electron beam to the thermocouple was estimated to be less than 0.1 mm. Because of this proximity Auger analysis of the sample were performed after each annealing. No Cr or Al contamination from the thermocouple was observed.

EXPERIMENTAL RESULTS

Figure 1 contains a schematic diagram of the experimental results and their interpretation. Two distinct regions are apparent. In region A the carbon Auger spectrum had the peculiar fine structure which has been already analyzed[13]. In this region we attribute the relative increase of the peak-to-peak amplitude of the carbon signal to carbon atoms migrating from the layers near to the surface and replacing nickel atoms at the surface.

In region B the carbon Auger spectrum had the graphitic form. In this region we assign the relative increase of the carbon signal to carbon atoms moving on the surface to form graphite patches.

The two processes outlined above should be borne in mind when considering the experimental results shown in Figs. 2-4. These figures show the peak-to-peak amplitude of the $dN(E)/dE$ Auger signal of carbon (272 eV) and nickel (65 eV). The peak-to-peak amplitudes of these signals were recorded for three temperatures: 345, 370 and 425°C. As previously mentioned, these amplitudes were recorded continuously by means of a multiplexing unit.

The first important characteristic of these curves that should be noted is the time for the transition to occur from region A to region B. As the absolute temperature increases, the transition time decreases. Our interpretation is that at higher temperatures precipitation to the surface and surface diffusion occur at comparable rates, so that regions A and B tend to merge together.

A second feature to be noted is the apparent plateau in region A for temperatures below 370°C. Since the mean escape depth of the 273 eV carbon KLL Auger electrons is about 10 \AA [15], it appears that in the plateau of region A, the number of carbon atoms within about 10 \AA from the surface is constant. However, as the time increases, carbon atoms continue to replace nickel atoms at the surface. This is shown by the continued decrease of the nickel Auger

signal.

In region B, more carbon atoms accumulate near the surface and diffuse to form patches of graphite that will eventually cover the entire surface.

The KLL Auger spectrum of carbon was monitored continuously and simultaneously with the peak-to-peak amplitudes. Figure 5 shows how the shape of the Auger carbon spectrum changes as the concentration of the carbon increases. It is also important to note that in this case, as in all the others, the change in the shape of the Auger spectrum corresponds to the transition point between regions A and B in the peak-to-peak amplitude curve. At this particular point the Auger signal having the peculiar fine structure in the low energy side starts changing into that which is identified as characteristic of graphite.

When the concentration reaches the saturation point, the carbon Auger spectrum is graphitic and no further changes occur either in shape or in peak-to-peak amplitude.

It is apparent that changes in shape of the KLL Auger spectrum and the peak-to-peak amplitude curves both record the process as it occurs on a microscopic scale.

Recording of the process on a macroscopic scale was obtained with the aid of the Auger micrographing technique previously mentioned, (fig. 6). In this figure, micrograph A shows the state of the sample when the recording of the data started. In this, and in all the other micrographs, the bright regions correspond to areas where carbon is

present at the surface. In micrograph A we can see only traces of carbon on the surface. Micrograph B was taken just before the Auger spectrum started to change in shape. It can be seen that the amount of carbon at the surface has increased considerably, but the carbon islands are still separated from each other. Micrograph C was recorded immediately after the transition point. It should be noted that in the central portion of this micrograph the carbon islands begin to cluster together as the amount of carbon continues to increase.

Finally, in micrograph D, the carbon covers almost entirely the surface of the sample. At this time the KLL Auger spectrum is definitely graphitic and does not change further in shape or in size.

ANALYSIS

For region A we considered the relation between the initial and final relative concentrations of carbon and the time to the transition point. For region B we used in the analysis the increase in the carbon relative concentration as a function of time. Carbon relative concentration defined as:

$$\frac{dN(E)/dE \text{ PEAK-TO-PEAK AMPLITUDE OF CARBON}}{dN(E)/dE \text{ PEAK-TO-PEAK AMPLITUDE OF NICKEL}}$$

was used instead of absolute concentrations in order to minimize instrumental error. This instrumental error is produced mainly by variations in the primary electron beam current, electron beam size and different settings in the

electron multiplier and the lock-in-amplifier needed for the processing of the signal. Relative concentration will be referred to simply as concentration.

The representative data points used in the analysis of the process in region B are presented in Fig. 7. The initial concentration and zero time for this process were taken at the transition point between zones A and B.

It is very important to note that the concentration recorded as a function of time will represent, at any time, the total amount of the particular element that has appeared at the surface. Therefore, the surface concentration of the element analyzed, considered to be proportional to the peak-to-peak amplitude of the Auger $dN(E)/dE$ spectrum, will be given by:

$$C_s(x,t) = \int_0^t -D(\partial C(x,t)/\partial x) dt \quad (1)$$

where $C(x,t)$ is the solution of the diffusion equation.

In order to choose a suitable model that would explain the experimental results, we considered the following: First, the concentrations that we obtained are not a function of depth but of time. Second, the concentration variation in time starts at an initial value C_0 and after a certain time reaches its maximum value without further increase. And, third, the concentration depends strongly on \sqrt{t} . This suggests that the solution of the diffusion equation is given by a source type solution where the concentration is proportional to:

$$[1/\sqrt{t}]e^{-x^2/4Dt}$$

or else it is of the error function type:

$$2/\sqrt{\pi} \int_0^z e^{-x^2} dx, \quad z = x/\sqrt{4Dt} .$$

The two diffusion processes in regions A and B can be described mathematically by the following set of equations, (see also Appendix I):

$$\partial C_1(x,t)/\partial t = D_1 \partial^2 C_1(x,t)/\partial x^2 \quad (2)$$

$$\partial C_2(x,t)/\partial t = D_2 \partial^2 C_2(x,t)/\partial x^2 \quad (3)$$

with boundary conditions:

$$C_1(x,0) = C_{10} \quad ; \quad C_2(x,0) = C_{20} \quad (4)$$

$$-D_1 \partial C_1(0_-,t)/\partial x = -D_2 \partial C_2(0_+,t)/\partial x \quad (5)$$

$$C_1(0_-,t) = mC_2(0_+,t) \quad (6)$$

This set of equations represents the diffusion through an interface having different diffusivities at both sides of the interface. The constant m in eq. (5) introduces a discontinuity in the concentration at the interface. This discontinuity is intended to reproduce the transition point of the concentration vs time curve.

The problem of diffusion through an interface and problems involving similar boundary conditions are very well treated in the literature[16-21]. Considering the fact

that the concentration showed a saturation region, the first model that was applied included a boundary condition of the form[16]:

$$C_1(-h,t) = 0 = C_2(h,t) \quad (7)$$

This boundary condition contains the assumption that the diffusion system has finite dimensions. The parameter h has no physical meaning in our system. It represents only the parametrical finite length of the media at both sides of the interface. The general solution for this system, as reported in ref. [16], can be expressed by:

$$C(x,t) = f(x,h)e^{-D\lambda^2 t}. \quad (8)$$

Taking the partial derivative of eq. (8) with respect to x and substituting into the right side of eq. (1) gives the surface concentration as a function of time:

$$C_s(0,t) = (A/\lambda^2) [1 - e^{-D\lambda^2 t}] \quad (9)$$

where the value of the constant A will depend on the parameter h .

Now, if we neglect the boundary condition given by eq. (7), the problem becomes that of a diffusion across an interface of two semi-infinite media. The solution to this case can be found in refs. [17 and 21] as follows:

$$C_2(x,t) = C_{20} + \frac{C_{10} - C_{20}/m}{1/m + \sqrt{D_2/D_1}} \operatorname{ERFC}[x/\sqrt{4D_2t}] \quad -\infty < x < 0 \quad (10)$$

$$C_1(x,t) = C_{10} + \frac{C_{20} - mC_{10}}{m + \sqrt{D_1/D_2}} \{ \operatorname{ERF}[x/\sqrt{4D_1t}] + 1 \} \quad 0 < x < -\infty \quad (11)$$

The solution for the problem can be obtained by using Laplace transforms. This is shown in Appendix I.

Substituting the partial derivatives with respect to x of either eq. (10) or (11) into eq. (1), setting $x = 0$ and integrating leads to the surface concentration as a function of time:

$$C_s(0,t) = A\sqrt{Dt} \quad (12)$$

where A is a constant that will depend on the initial concentration.

DISCUSSION

Solutions of the form of eq. (9) successfully explained the behavior of the system in region A. The carbon concentration in region B did not agree with an exponential dependence on time. A solution of the form of eq. (12) was satisfactory for region B but did not explain the behavior of the system in region A.

In view of the fact that we had two well defined processes for which the same model did not apply satisfactorily

we treated them as two independent processes for which different conditions should be applied. Once this assumption was made we were able to obtain reasonable results.

For region A the activation energy of the process was obtained by first plotting the logarithm of the initial and final concentrations versus time. The slope of the straight line joining those points represented the value of $\lambda^2 D$. The values of $\lambda^2 D$ obtained by this procedure were used in a plot of $\ln(\lambda^2 D)$ vs $1000/RT$ in $(\text{cal/mole})^{-1}$ as shown in fig. 8.

The calculated activation energy for this process was 9.4 ± 0.6 kcal/mole. The uncertainty represents the standard deviation of the least squares fit to the data points.

Since we were not able to resolve the concentration profile as a function of depth, we had no means of evaluating the parameter λ . Therefore we could not evaluate the diffusion coefficient for this process.

For region B the surface concentration as a function of time was given by:

$$C_s(t) = C_0 \sqrt{Dt/\pi} \quad (13)$$

where C_0 represents the initial bulk concentration of carbon.

The diffusion coefficient D was obtained by plotting $\sqrt{\pi} C_s(t)/C_0$ versus \sqrt{t} . Using this procedure D was calculated by a least-squares fitting of a straight line to

the data points and evaluation of the slope of the line. The results are shown in fig. 9. Once the diffusion coefficient was obtained for each temperature, the activation energy for the process was calculated from a plot of $\ln(D)$ vs $1000/RT$ (fig. 10), this last quantity being given in $(\text{cal/mole})^{-1}$. The activation energy was estimated to be 6.9 ± 0.6 kcal/mole for this process. The diffusion coefficient then fits an equation of the form:

$$\ln(D) = 10.27 - 3568/T \quad (14)$$

and the pre-exponential factor D_0 is of the order of:

$$3.5 \times 10^{-5} \text{ cm}^2/\text{sec.}$$

CONCLUSION

We studied the process of carbon diffusion on the surface of polycrystalline nickel. This was done by monitoring the changes in shape and in size of the carbon Auger spectrum in the derivative mode. We observed two distinct processes. One process has an activation energy of 9.4 ± 0.6 kcal/mole which we assign to carbon atoms leaving their sites below the surface and migrating to the top layer. Another with an activation energy of 6.9 ± 0.6 kcal/mole which we ascribe to carbon atoms moving on the surface of the nickel to form patches of graphite which eventually will cover the entire surface.

Attempts to use the proposed procedure with a carburized nickel sample or at temperatures higher than 490°C failed because it was not possible to obtain a carbon Auger spectrum showing fine structure in the low energy side of the 272 eV minimum.

REFERENCES

- [1] W.D. Klopp and V.D. Barth, Memorandum 50 (Defense Metals Information Center, Battelle Memorial Institute, Columbus, Ohio, 1960).
- [2] R.W. Powers and M.V. Doyle, Trans. AIME 209 (1957) 1285.
- [3] T-S. Ke, Phys. Rev. 74 (1948) 9.
- [4] C.A. Wert, J. Appl. Phys. 21 (1950) 1196.
- [5] T.A. Massaro and E.E. Petersen, J. Appl. Phys. 42 (1971) 5534.
- [6] H.E. Bishop and J.C. Riviere, Acta Met. 18 (1970) 813.
- [7] H.S. Wildman, J.K. Howard and P.S. Ho, J. Vacuum Sci. Technol. 12 (1975) 75.
- [8] E.N. Sickafus, Surface Sci. 19 (1970) 181.
- [9] L.C. Isett and J.M. Blakely, Report # 2250 (Materials Research Center, Cornell University, Ithaca, N.Y.).
- [10] L.C. Isett and J.M. Blakely, J. Vacuum Sci. Technol. 12 (1975) 237.
- [11] J.C. Shelton, H.R. Patil and J.M. Blakely, Surface Sci. 43 (1974) 493.
- [12] N. Laegreid and G.K. Wehner, J. Appl. Phys. 32 (1961) 365.
- [13] J.F. Mojica, to be published.
- [14] N.C. MacDonald, in: Physical Aspects of Electron Microscopy and Microbeam Analysis, Ed. B.J. Siegel and D.R. Beaman (John Wiley and Sons, Inc., 1975) p.431.
- [15] C.C. Chang, in: Characterization of Solid Surfaces, Ed. P.F. Kane and G.B. Larrabee (Plenum Press, New York-London, 1974) p.509.
- [16] E.J. Scott, L.H. Tung and H.G. Drickamer, J. Chem. Phys. 19 (1951) 1075.

- [17] R.B. Bird, W.E. Stewart and E.N. Lightfoot, in: Transport Phenomena (John Wiley and Sons, Inc., New York-London-Sidney,1960).
- [18] H.S. Carslaw and J.C. Jaeger, in: Conduction of Heat in Solids (Oxford University Press, London,1959).
- [19] P.G. Shewmon, in: Diffusion in Solids (McGraw-Hill Book Company, Inc., New York-San Francisco-Toronto-London,1963).
- [20] M. Wuttig and H.K. Birnbaum, Phys. Rev. 147 (1966) 495.
- [21] M.R. Spiegel, in: Laplace Transforms, Schaum Series (McGraw-Hill Book Company, New York-St. Louis-San Francisco-Toronto-Sidney,1965).

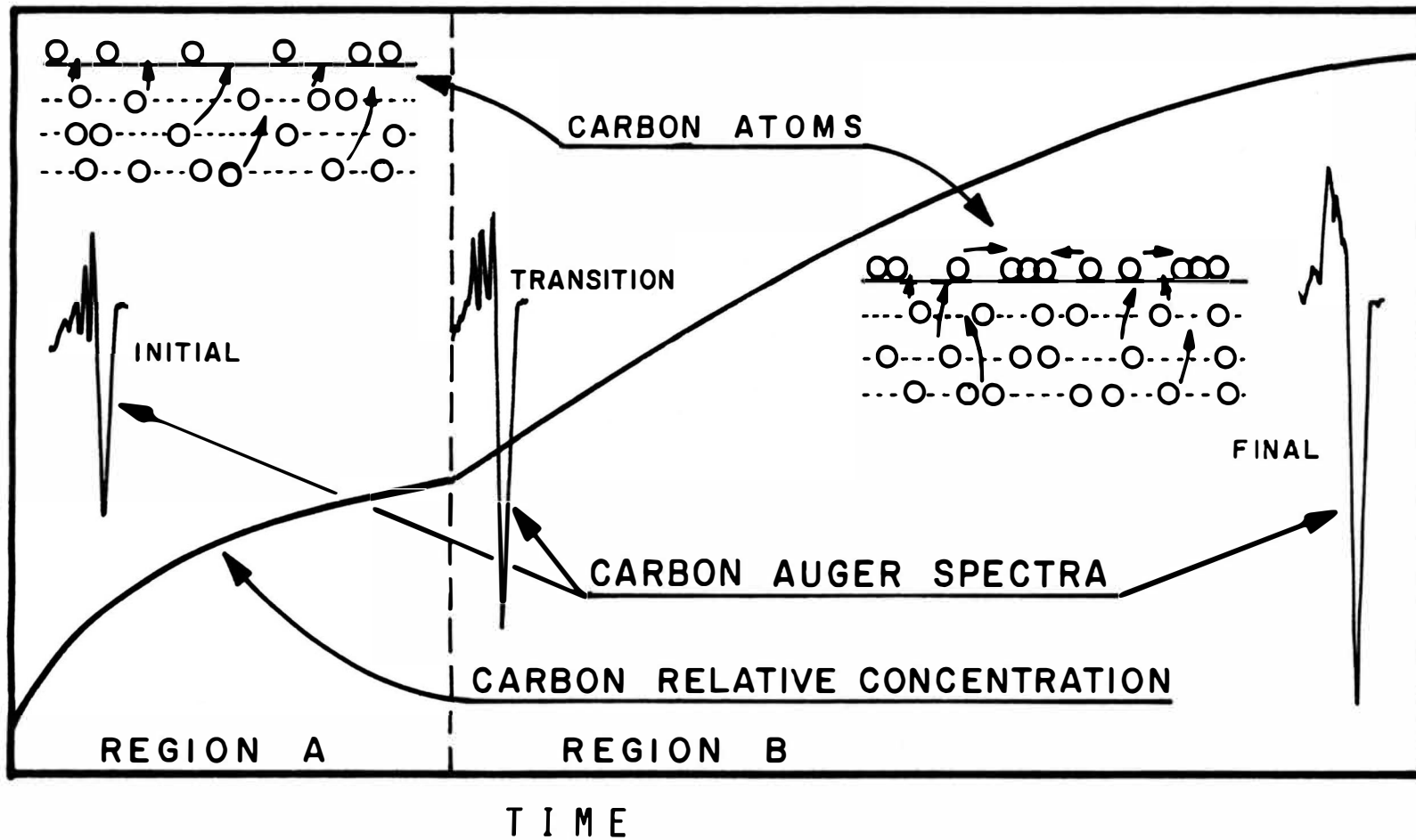


Figure 1. Schematic diagram of the experimental results and their interpretation.

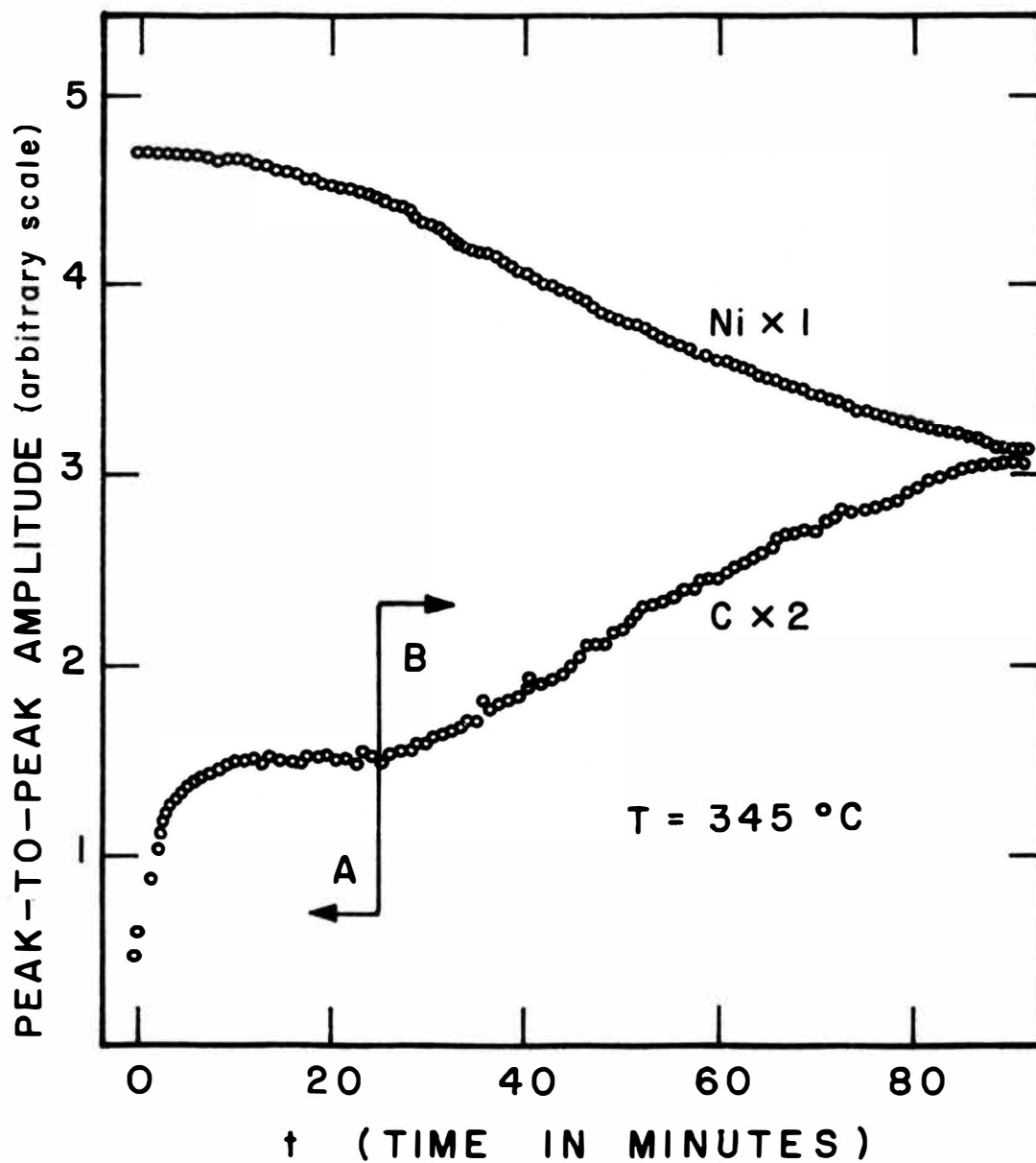


Figure 2. Time dependence of the peak-to-peak amplitude of the $dN(E)/dE$ Auger spectrum of carbon and nickel.

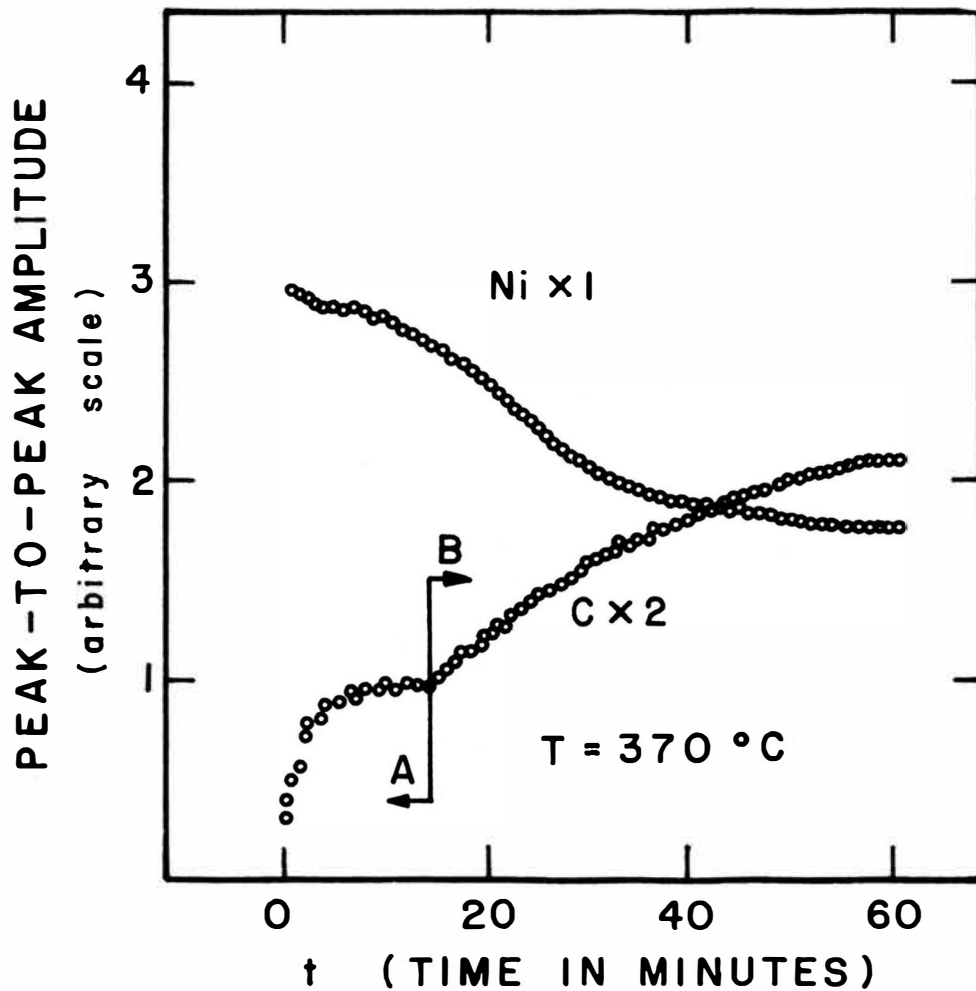


Figure 3. Time dependence of the peak-to-peak amplitude of the $dN(E)/dE$ Auger spectrum of carbon and nickel.

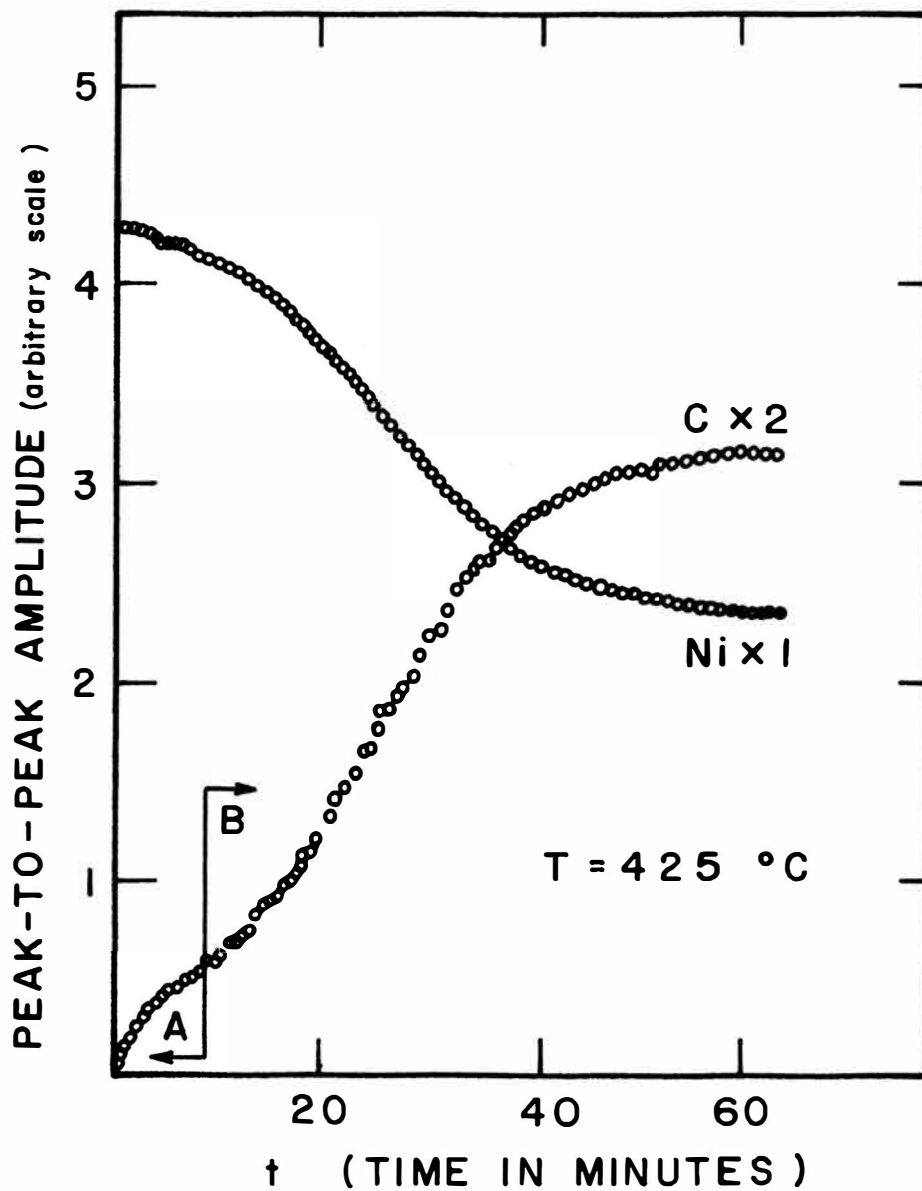


Figure 4. Time dependence of the peak-to-peak amplitude of the $dN(E)/dE$ Auger spectrum of nickel and carbon.

Figure 5. Evolution of the carbon Auger spectrum as the concentration of carbon increases at the surface. The time marks indicate when recordings were started after heating began.

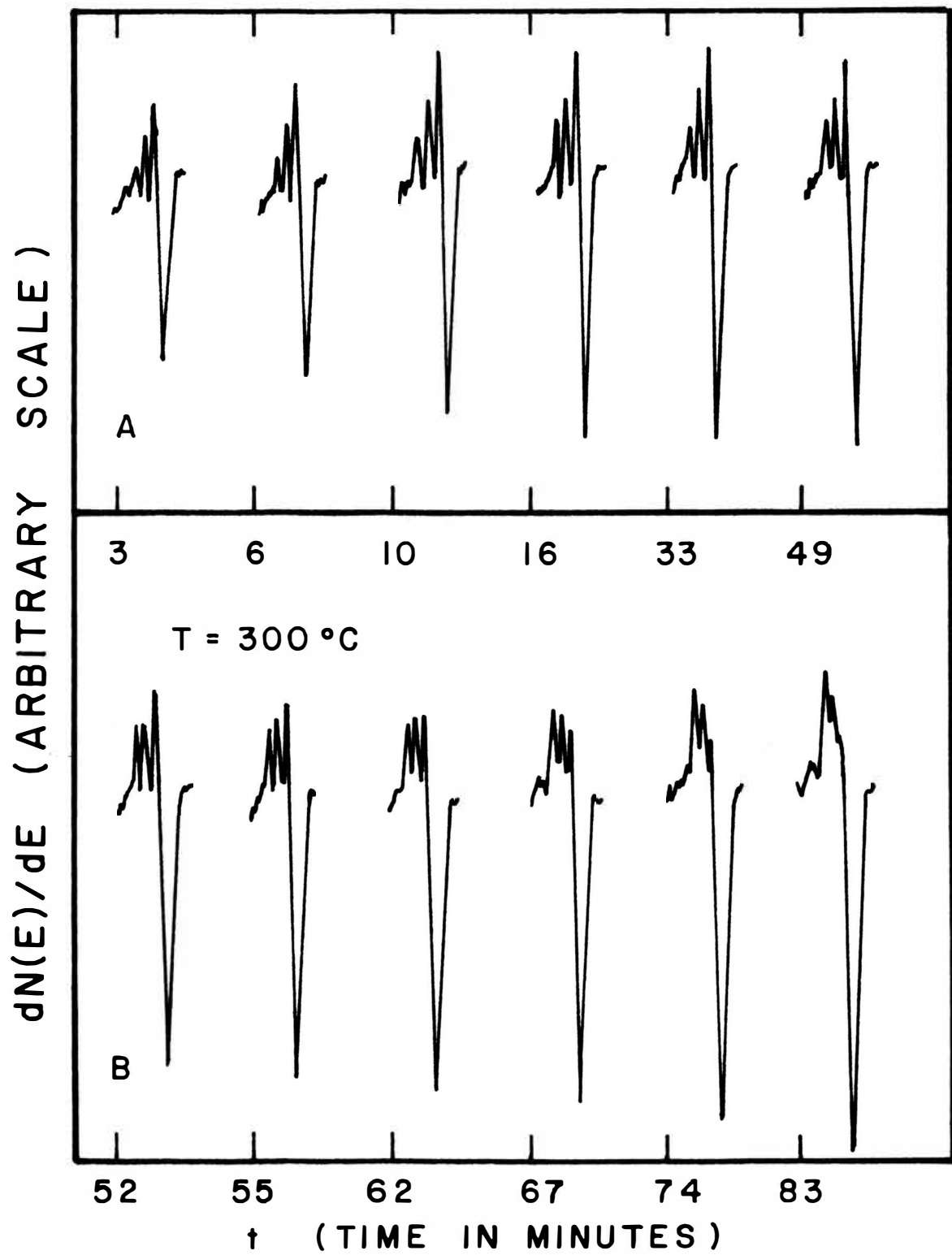
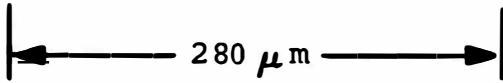
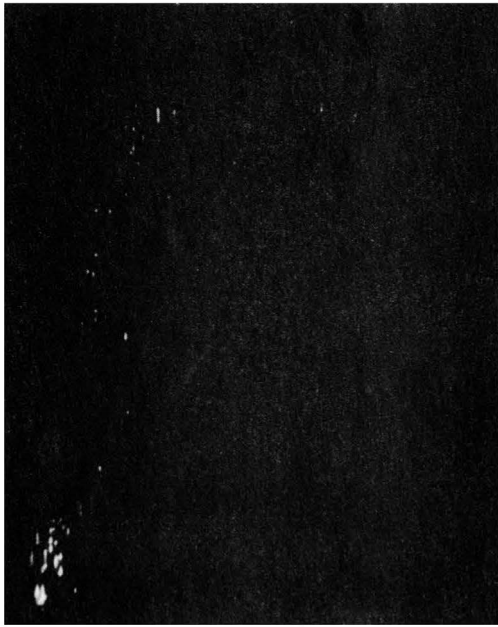
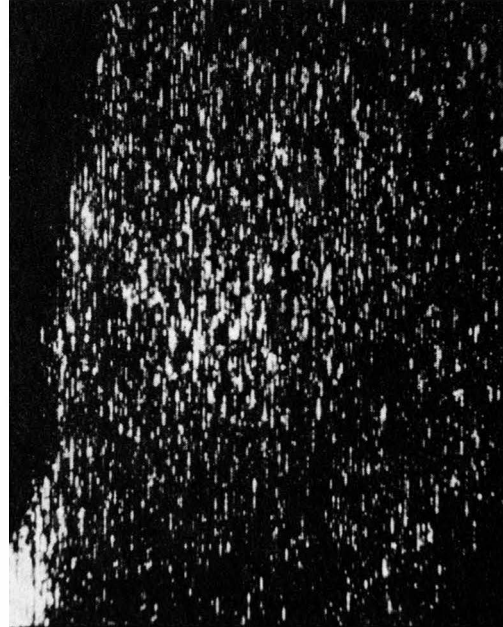


Figure 5

Figure 6. Micrographs of carbon on the surface of polycrystalline nickel. The arrow in micrograph D indicates the position of the electron beam when the Auger spectra were recorded. The diameter of the beam was 5 μm . This will correspond to a spot of 1.16 mm diameter in the micrograph.

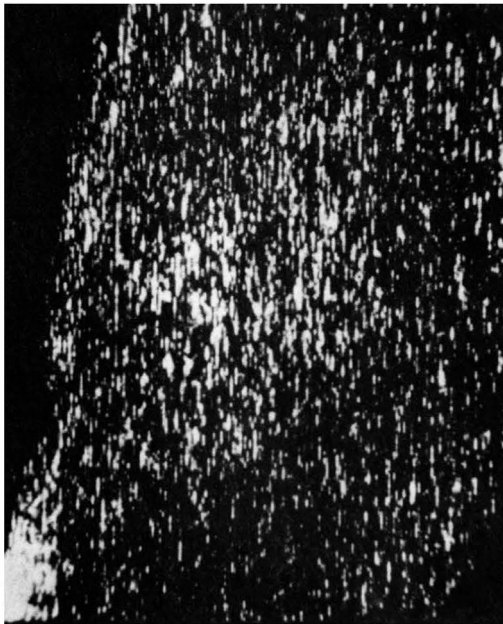


A: t = 2 minutes.



B: t = 50 minutes.

C: t = 53 minutes.



D: t = 84 minutes.

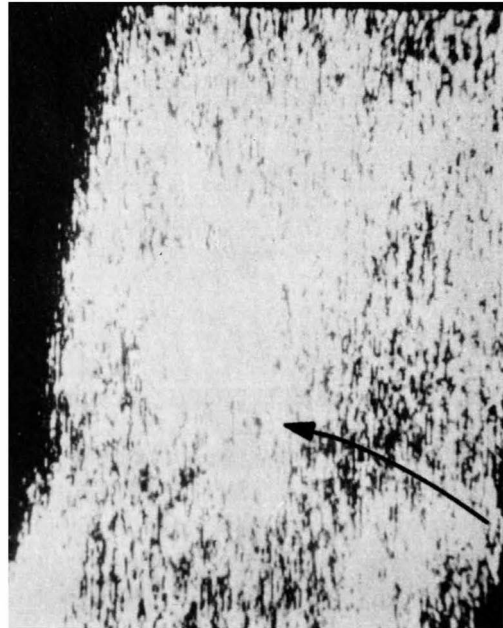


Figure 6

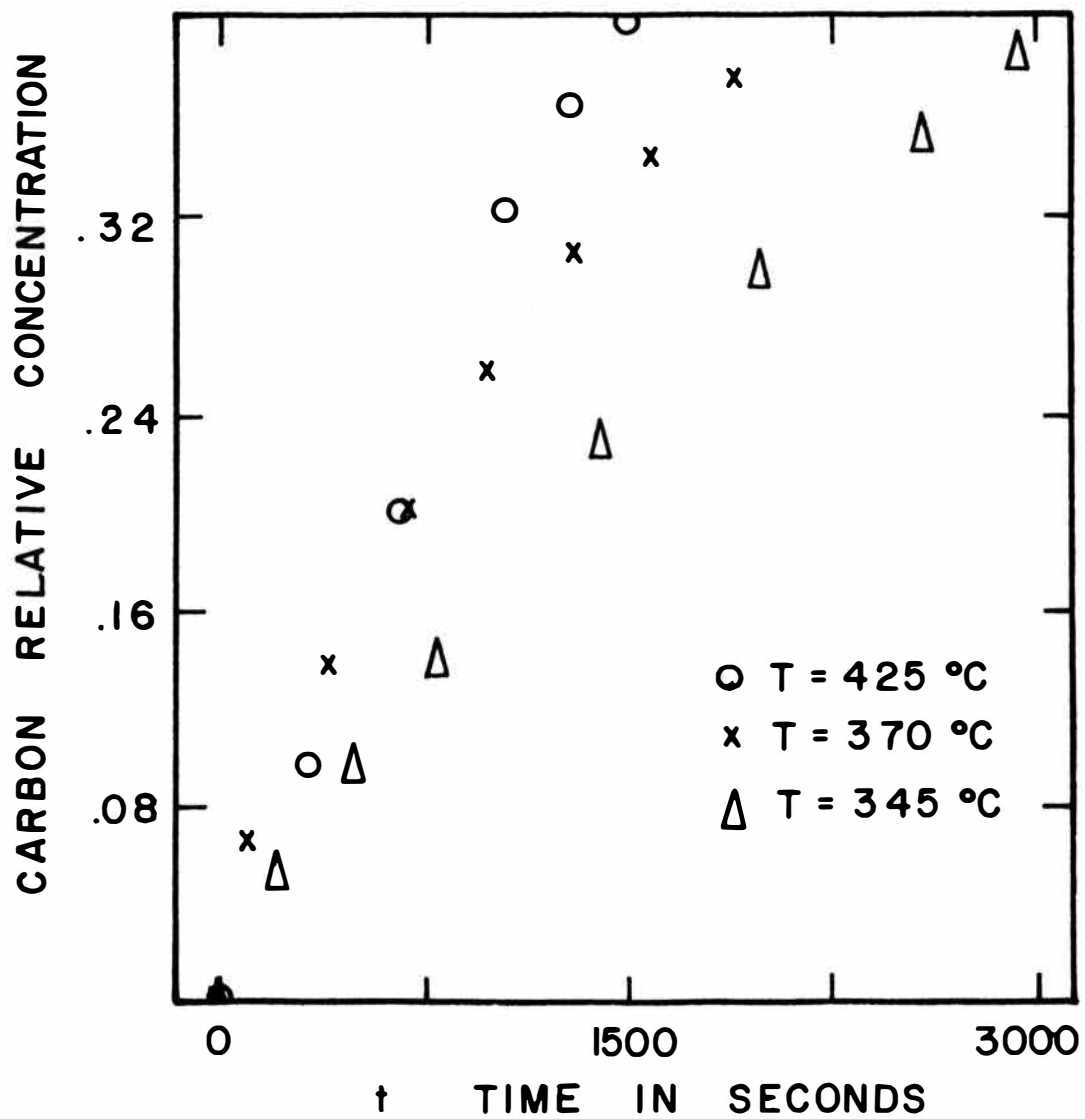


Figure 7. Time dependence of the carbon relative concentration at the surface of the polycrystalline nickel sample. Zero time is taken at the transition point between zones A and B.

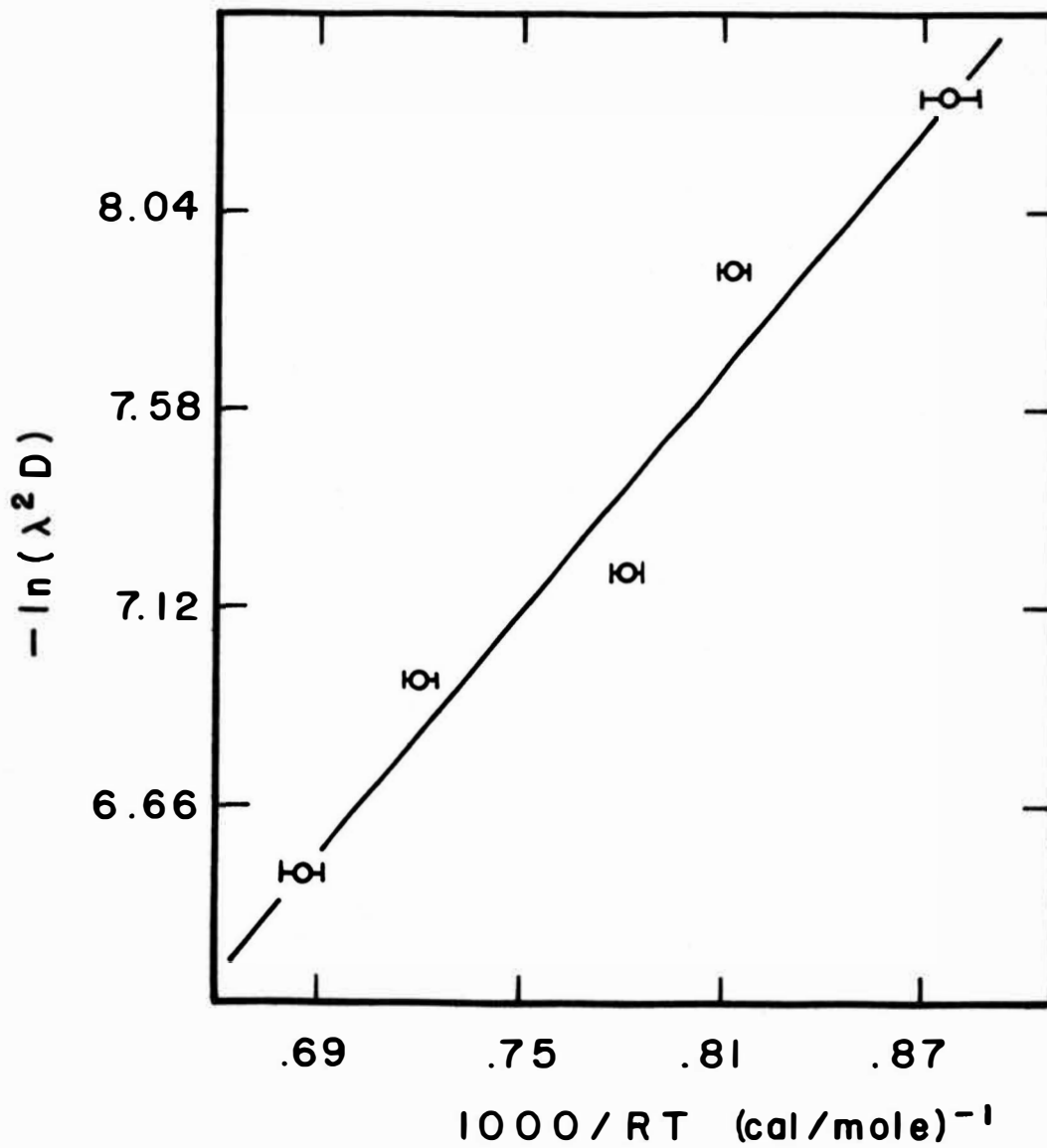


Figure 8. Bulk-to-surface diffusion coefficient D dependence of $1/T$.

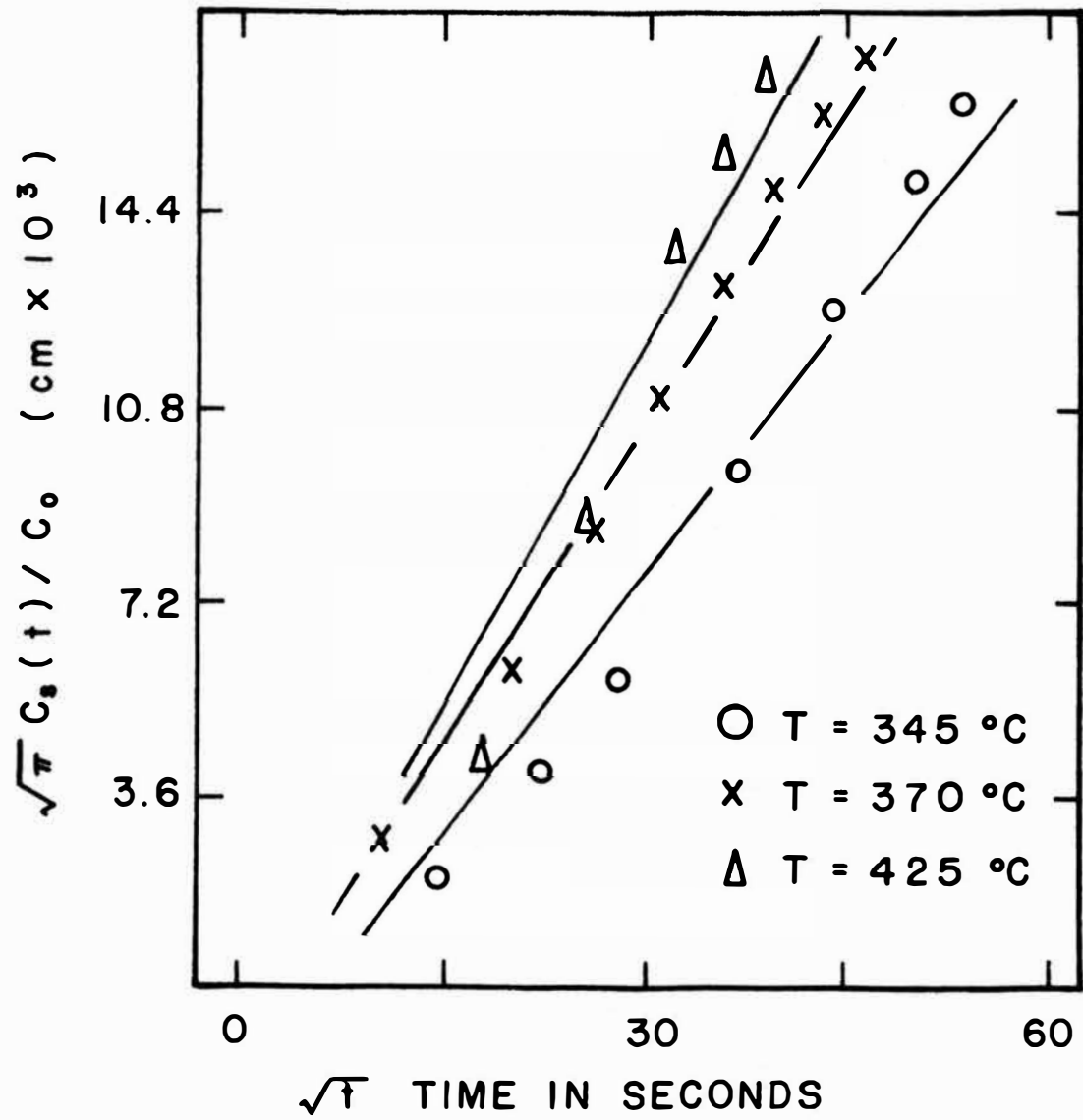


Figure 9. Plot of the normalized surface concentration of carbon versus \sqrt{t} . Zero time is taken at transition point between zones A and B.

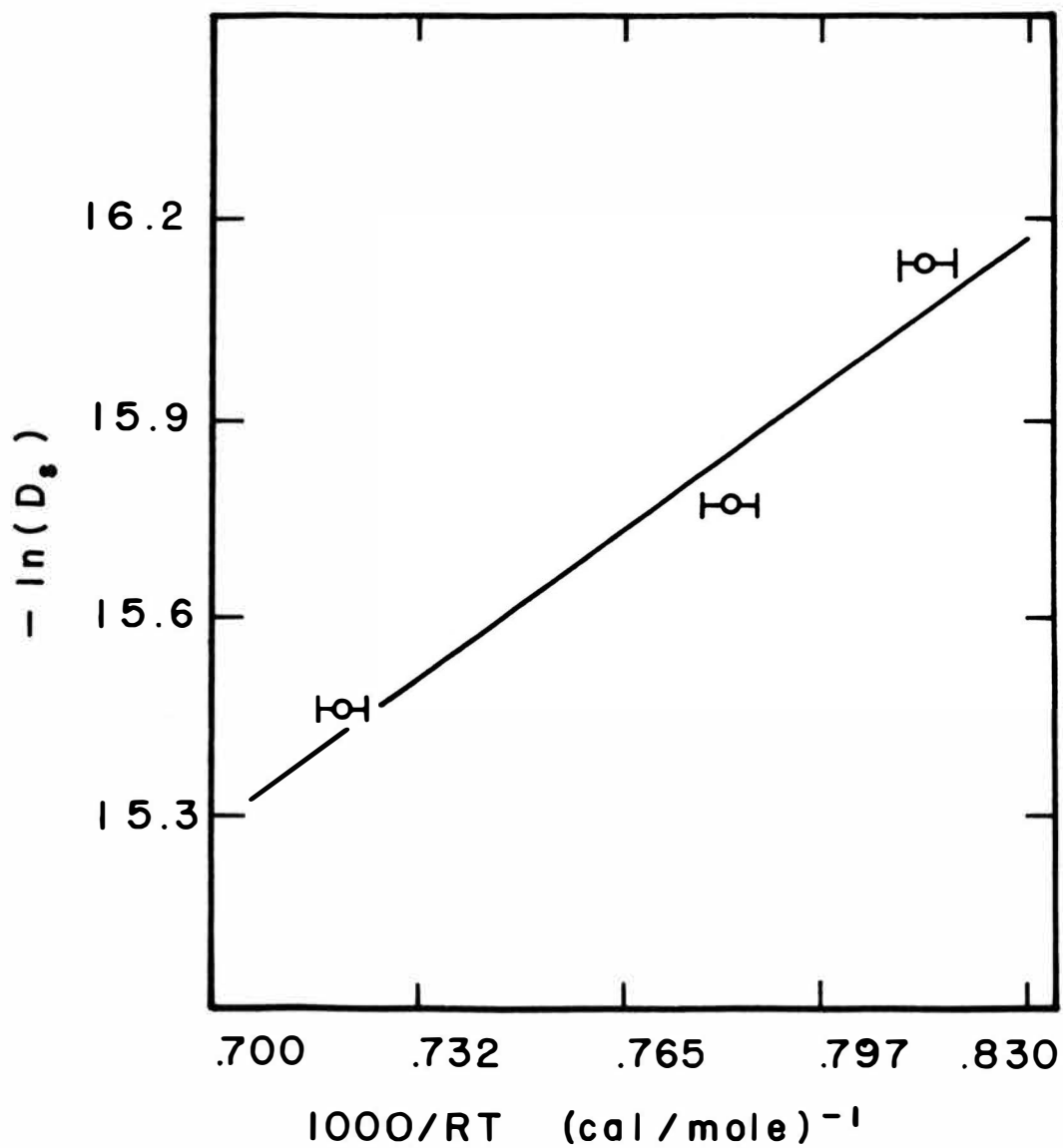
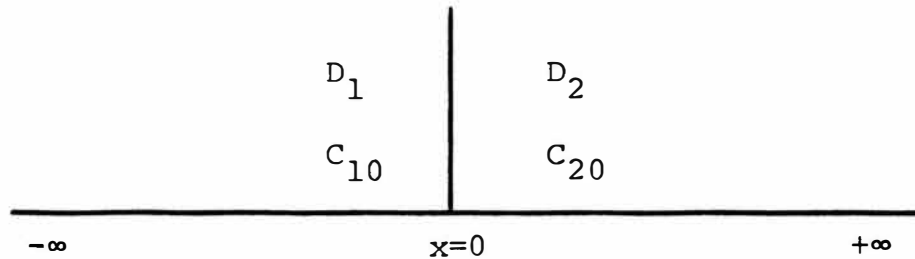


Figure 10. Surface diffusion coefficient D_s dependence of $1/T$.

APPENDIX I

DIFFUSION OF TWO SEMI-INFINITE MEDIA THROUGH AN INTERFACE.



The equations to be solved are:

$$\partial C_1 / \partial t = D_1 \partial^2 C_1 / \partial x^2 \quad (1)$$

$$\partial C_2 / \partial t = D_2 \partial^2 C_2 / \partial x^2 \quad (2)$$

with boundary conditions:

$$C_1(x, 0) = C_{10} \quad ; \quad C_2(x, 0) = C_{20} \quad (3)$$

$$-D_1 \partial C_1(0_-, t) / \partial x = -D_2 \partial C_2(0_+, t) / \partial x \quad (4)$$

$$C_1(0_-, t) = m C_2(0_+, t) \quad (5)$$

Call $L\{C(x, t)\} = c(x, s)$ where L is the Laplace transform operator, and use:

$$L\{\partial U / \partial t\} = su - U(x, 0) \quad (6)$$

$$L\{\partial^2 U/\partial x^2\} = d^2 u/dx^2 . \quad (7)$$

Then for $C_1(x,t)$:

$$D_1 d^2 c_1/dx^2 = sc_1 - C_{10} \quad (8)$$

with solution:

$$c_1(x,s) = A_1 e^{x\sqrt{s/D_1}} + A_2 e^{-x\sqrt{s/D_1}} + C_{10}/s. \quad (9)$$

Similarly for $C_2(x,t)$:

$$c_2(x,t) = B_1 e^{x\sqrt{s/D_2}} + B_2 e^{-x\sqrt{s/D_2}} + C_{20}/s. \quad (10)$$

Since we want the solution to be finite for every x , then: $A_2 = B_1 = 0$. Now the solutions are:

$$c_1(x,s) = A e^{x\sqrt{s/D_1}} + C_{10}/s \quad \text{and} \quad (11)$$

$$c_2(x,s) = B e^{-x\sqrt{s/D_2}} + C_{20}/s . \quad (12)$$

Apply now the boundary condition given by eq. (4):

$$-D_1 (s/D_1)^{1/2} A e^{x\sqrt{s/D_1}} = D_2 (s/D_2)^{1/2} B e^{-x\sqrt{s/D_2}} . \quad (13)$$

Then at $x = 0$,

$$A/B = -(D_2/D_1)^{1/2} . \quad (14)$$

Substitute now eq. (14) in eq. (5):

$$B + C_{20}/s = mA + mC_{10}/s \quad (15)$$

and solve for B to obtain:

$$B = (1/s) \frac{mC_{10} - C_{20}}{1 + m\sqrt{D_2/D_1}} . \quad (16)$$

Substitution of eq. (16) in eq. (12) gives:

$$c_2(x,s) = \frac{mC_{10} - C_{20}}{1 + m\sqrt{D_2/D_1}} \{ e^{-x\sqrt{s/D_2}} + C_{20} \} (1/s) \quad (17)$$

and since $C_2(x,t)$ is given by $L^{-1}\{c_2(x,s)\}$

$$C_2(x,t) = \frac{C_{10} - C_{20}/m}{1/m + \sqrt{D_2/D_1}} \operatorname{erfc}\{x/\sqrt{4D_2t}\} + C_{20} . \quad (18)$$

Solving eq. (15) for A:

$$A = (1/s) \frac{C_{20} - mC_{10}}{m + \sqrt{D_1/D_2}} . \quad (19)$$

Using this expression in eq. (11) we have:

$$c_1(x,s) = \frac{C_{20} - mC_{10}}{m + \sqrt{D_1/D_2}} [e^{x\sqrt{s/D_1}}]/s + C_{10}/s \quad (20)$$

and using the Laplace inverse transform:

$$C_1(x,t) = \frac{C_{20} - mC_{10}}{m + \sqrt{D_1/D_2}} \operatorname{erfc}\{-x/\sqrt{4D_1t}\} + C_{10} \quad \text{or} \quad (21)$$

$$C_1(x,t) = C_{10} + \frac{C_{20} - mC_{10}}{m + \sqrt{D_1/D_2}} [1 + \operatorname{erf}\{x/\sqrt{4D_1t}\}] \quad . \quad (22)$$

VITA

The author was born in San Luis Potosi, S.L.P., Mexico, September 15, 1941. He entered the Seminario Arquidiocesano de Monterrey in 1956 where he completed the course work in Humanities, Philosophy and Theology. He entered the Instituto Tecnológico de Monterrey in 1966 and received a B.S. in Physics in 1971. He entered the University of Missouri-Rolla in 1971 and received a M.S. degree in Physics in 1974. He also received a B.S. in Metallurgical Engineering in 1974. He has worked as an Assistant Professor of Humanities and Physics in the Universidad Labastida, Universidad de Monterrey and in the Instituto Tecnológico de Monterrey from 1966 to 1971. He has been engaged in graduate research since 1972. He is married and has two children.